Reprinted from SUMITOMO LIGHT METAL TECHNICAL REPORTS (Title No. P-385)

論　文

Grain Refinement of a High Strength Aluminium Alloy Sheet*

Hideo Yoshida**, Teruo Uno*** and Yoshio Baba***

住友軽金属工業株式会社技術研究所

論　文

Grain Refinement of a High Strength Aluminium Alloy Sheet*

Hideo Yoshida[**], **Teruo Uno**[***] **and Yoshio Baba**[***]

It has been known that a high strength aluminium alloy, Al−Zn−Mg−Cu−Cr, with a fine grain which size is below $20\mu m$ diameter, has superplasticity at high temperature. A fine-grained sheet is obtained in this study by a thermomechanical treatment including at least three steps, that is, precipitation, cold rolling and recrystallization. The mechanism of grain refinement is as follows. Large second-phase particles (AlCuMgZn, $Mg_3Zn_3Al_2$, $MgZn_2$, $\sim 1\mu m$ in diameter) which have no coherency with matrix precipitate during aging at high temperature or slow cooling in the first step. The matrix is homogeneously deformed by multiple slip in the presence of large particles. Therefore dislocation networks or cells are formed during deformation. The precipitation of supersaturated solute atoms formed by quenching make the sub-structure stable during heating. In high temperature, the precipitation of chromium inhibits the migration of grain boundaries. The grain size is determined by competition between the recovering rate of a deformed structure and the precipitating rate of solute atoms.

1. Introduction

A fine-grained high strength aluminium alloy has superplasticity at high temperature and is now going to apply to the superplastic forming in structural components of aircrafts. This fine-grained structure (grain size is below $20\mu m$) is obtained by a thermomechanical treatment (TMT).

Several kinds of TMT have been developed to improve the mechanical properties in high strength aluminium alloys[1,2]. In the conventional process to produce a plate, a cast structure is elongated in the rolling direction and dynamic recovery occurs within the elongated grains during high temperature deformation .The boundaries of elongated grains are corresponding to that of original cast grains where the seggregation of impurities occurs. This is why the fracture toughness and ductility of plates decrease. Especially, intermediate TMT (ITMT) which has a new concept in ingot processing improves these properties. The original cast grain boundaries are eliminated by a recrystalliza tion step prior to a conventional working process. This ingot processing involves homogenization of ingots followed by furnace cooling, then warm working (followed by rapid cooling), and finally, recrystallization by rapid heating. This processing produces fine grains by discontinuous recrystallization.The above mentioned method of grain refinement was designed to convert a conventionally processed plate into a fine-grained sheet, primarily for superplastic forming applications, by Wert et al[3,4].

The purposes of this investigation are to discuss the mechanism of grain refinement by TMT[5].

2. Experimental

A 6 mm thick plate commercially produced by conventional process was utilized for all of this experimental work. A high purity Al-Zn-Mg-Cu alloy (registrated as 7475 in Aluminum Association) was usually used. The chemical compositions of this alloy are presented in **Table 1**. The three dimensional microstructure of a 7475 plate solutionized at 753 K for 0.3 ks WQ is shown in **Fig. 1**.

The TEM in this study has a four-step sequence shown in **Fig. 2**, that is, solution treatment, precip-

Table 1 Chemical compositions (wt. %).

	Si	Fe	Cu	Mn	Mg	Cr	Zn	Ti
7475	0.04	0.04	1.57	<0.01	2.37	0.20	5.58	0.05

---

[*] Contribution to 4th Japan Inst of Metals Inter. Symp. (JIMIS−4) on Grain Boundary Structure and Related Phenomena held in Minakami Spa, Japan on 25～29 November 1985.

[**] Technical Research Laboratories, Metallurgical Technology Department

[***] Technical Research Laboratories, Dr. of Eng.

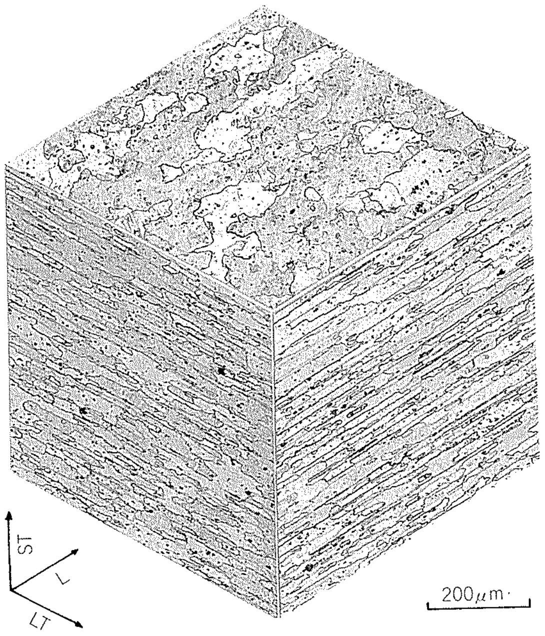

Fig. 1 Three dimentional microstructure of a hot-rolled plate followed by solution treatment at 753K for 0.3ks WQ.

itation, cold rolling and recrystallization. In the solution treatment at 753 K for 0.3 ks followed by quenching into water (WQ), the particles which precipitate during homogenizing or hot working are solutionized to produce a standard initial condition. In the next step, aging was carried out at high temperature from 633 to 753 K for 3.6~57.6 ks followed by WQ or furnace cooling (7×10^{-3} K/sec) to control the size and volume ratio of second-phase particles and the content of supersaturated solute atoms (Zn, Mg, Cu) in the matrix.

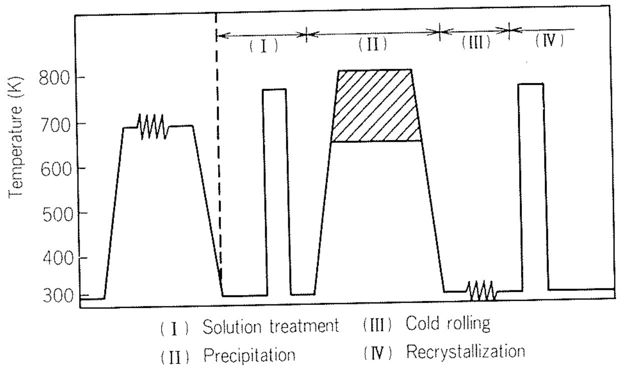

Fig. 2 Thermomechanical treatment in this investigation.

The above second-phase particles are solutionized above 733 K in this alloy. In the third step, the reduction of thickness are varied from 50~90%. In WQ, the period from quenching to cold rolling is within 1.8 ks because of natural age hardening. In the final step, the cold rolled sheets were recrystallized at 753 K for 0.3 ks in a salt bath and quenched into water.

The effect of heating rate in the recrystallization process on grain size was investigated by heating in an infrared furnace with a program controller. Grain size was measured in accordance with ASTM E−112.

3. Results and Discussion

3.1 Grain size

The effect of precipitation on grain size in recrystallized sheets (cold-rolling reduction of thickness, 90%), is indicated in **Table 2**. The same results were

Table 2 Effect of precipitation process on grain size (μm) in L−LT cross section of recrystallized sheets[1].

Solution treatment	Precipitation process										
	Aging temperature (K)	Aging time (×3.6ks)									
		1	2	4	8	16	1	2	4	8	16
		Water quenched					Furnace cooled				
753K×0.3ks WQ	633	–	–	11	9.5	9.5	–	–	19	19	16
	653	–	–	8	8	8	–	-3	16	16	13
	673	–	8	8	6.5	6.5	–	11	11	11	11
	693	–	9.5	9.5	8	6.5	–	11	11	11	11
	713	–	9.5	9.5	9.5	11	–	11	11	11	11
	733	–	11	11	–	–	–	11	11	–	–
	753	–	15	–	–	–	11	11	–	–	–
—	673	15	–	–	8	–	–	–	–	11	–
	753	–	15	–	–	–	–	11	–	–	–

(1) Reduction of thickeness in cold rolling : 90%

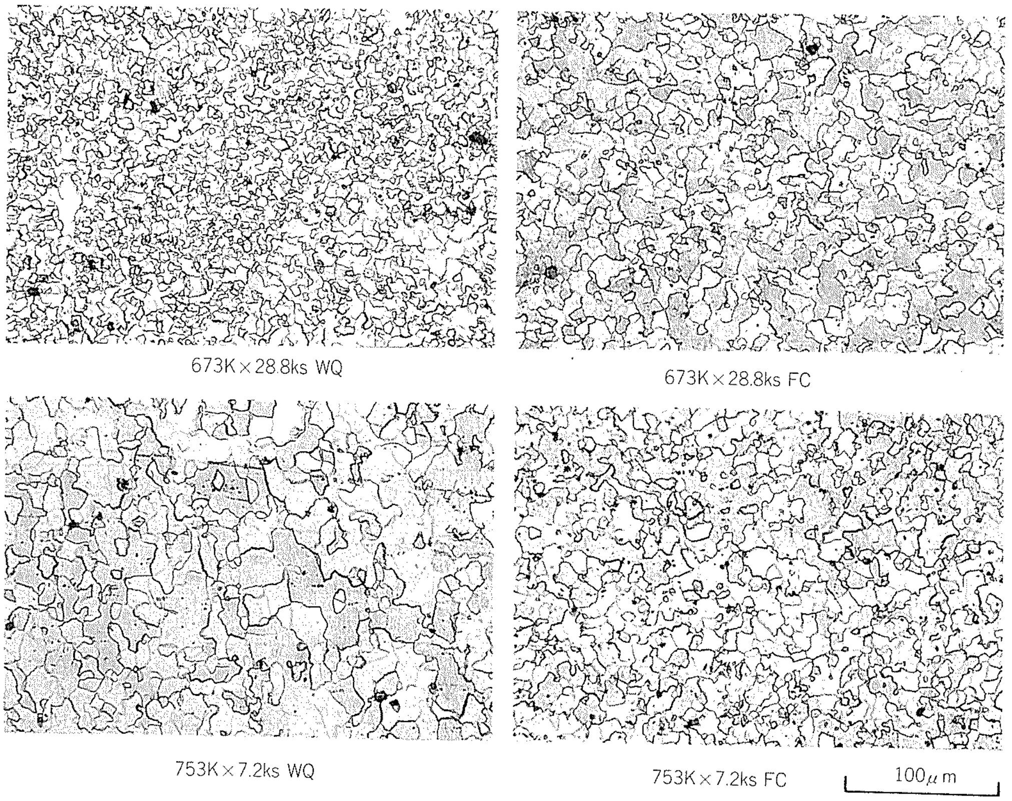

673K×28.8ks WQ

673K×28.8ks FC

753K×7.2ks WQ

753K×7.2ks FC

Fig. 3 Typical microstructures in a L-LT cross-section of recrystallized sheets (aged at 673K × 28.8ks and 753K × 7.2ks followed by cold-rolling at the reduction of 90%)

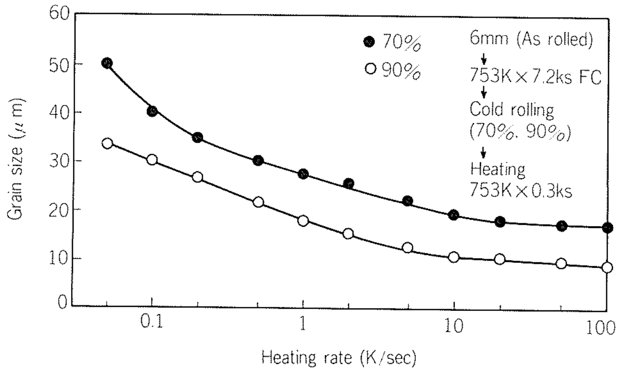

Fig. 4 Effect of heating rate on grain size in L-LT cross-section.

obtained in other reductions of thickness, 50%, 70% but the higher the reduction is, the finer the grain size becomes. **Table 2** shows that the process of solution treatment before precipitation has little influence on the final grain size. The finest grain occurs in aging at 673 K × 28.8~57.6 ks WQ. In WQ, the grain is the smallest in this aging temperature. This result agrees with the Wert's experiment. On the other hand, the almost same grain size are obtained in furnace cooling from 673 K or over. **Fig. 3** shows the typical microstructures in a L–LT cross-section.

The grain size is also influenced by heating rate in recrystallization process shown in **Fig. 4**. It is found that grain size becomes constant by heating at 10 K/sec or over.

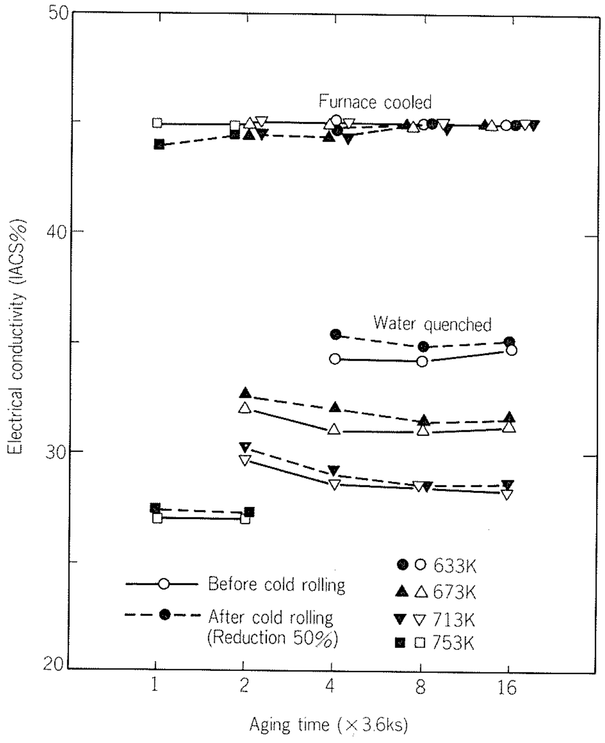

Fig. 5 Electrical conductivity measured before and after cold rolling at the reduction of 50%.

3.2 Electrical conductivity and microstructures

The electrical conductivity measured before and after the cold rolling (50% reduction) is shown in **Fig. 5**. This figure exhibits that the cold working increases the electrical conductivity in water-quenched materials and decreases it in furnace cooled ones. This suggests that supersaturated solute atoms formed by quenching into water precipitate on the dislocations or their networks introduced by cold working.

Figs. 6 and **7** show the effects of typical precipitation process on micro- and TEM structures before and after cold working (90% reduction). Large second-phase particles, which diameter is on the order of 1μm are observed except 753K×7.2ks WQ. These particles, identified as (AlCuMgZn), ($Mg_3Zn_3Al_2$) and ($MgZn_2$) phase by EDX and SAD, precipitate during aging at high temperature or furnace cooling and have no coherency with matrix. Another particles which size is 0.1~0.2μm in diameter are observed in every condition in **Fig. 6**. These

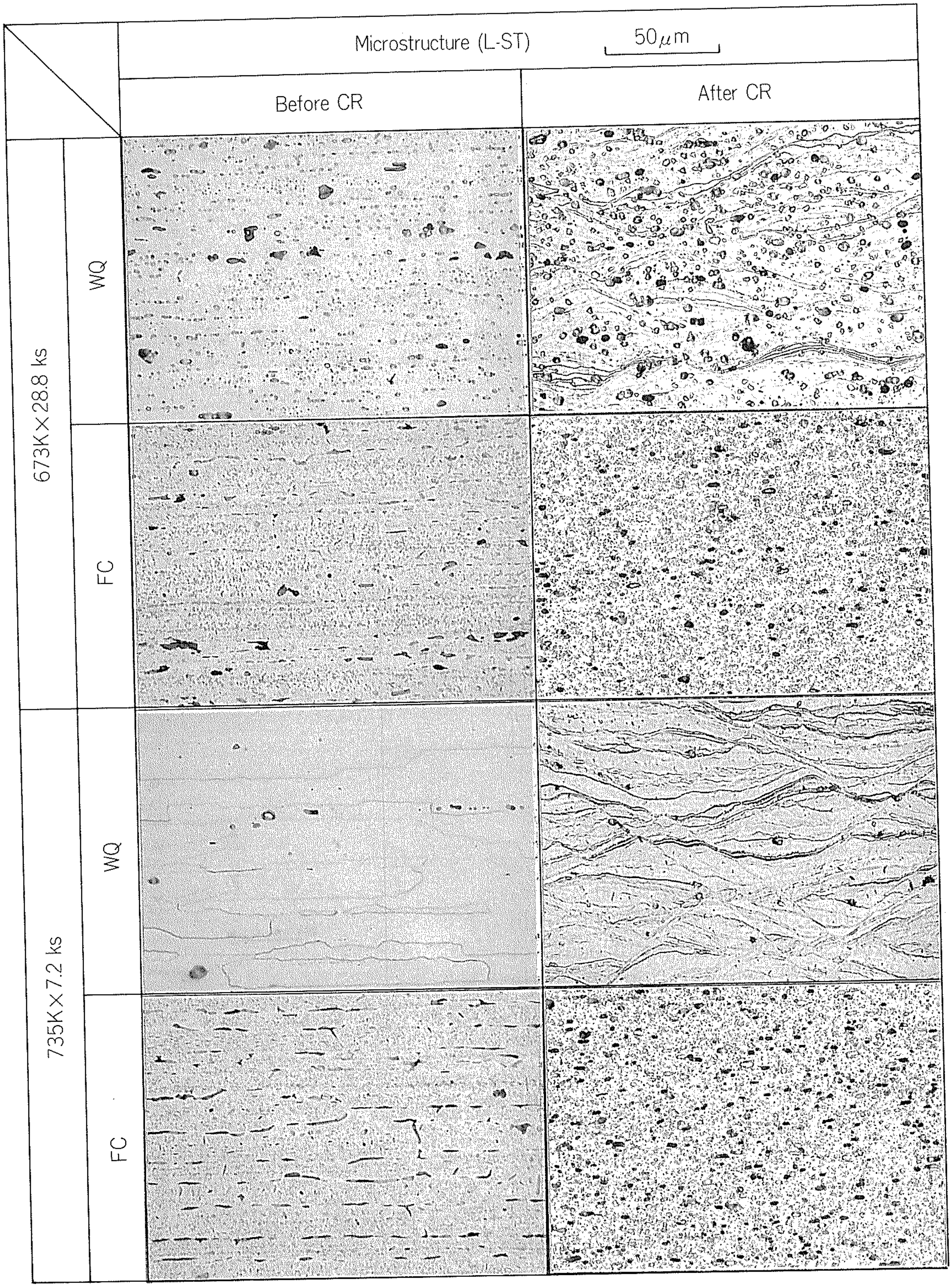

Fig. 6 Effect of typical precipitation process on microstructures before and after cold working.

particles are known as E-phase ($Al_{18}Mg_3Cr_2$) and precipitate during homogenizing and hot working of a ingot.

Heterogeneous deformation, particularly, shear bands are observed in the micro- and TEM structures only in cold working of the water-quenehed materials. Shear bands observed in L−LT cross section occur perpendicular to the rolling direction. The higher the quenching temperature is, the severer the shear bands becomes.

On the other hand, in furnace-cooled plates, the deformed structure becomes homogeneous. In TEM structures shown in **Fig.** 8, cell structures are observed in as cold-rolled sheets.

In heterogeneously deformed structure, dislocation density is altered. Consequently, the recovery of the deformed structure occurs heterogeneously. **Fig. 9** shows structural changes during heating

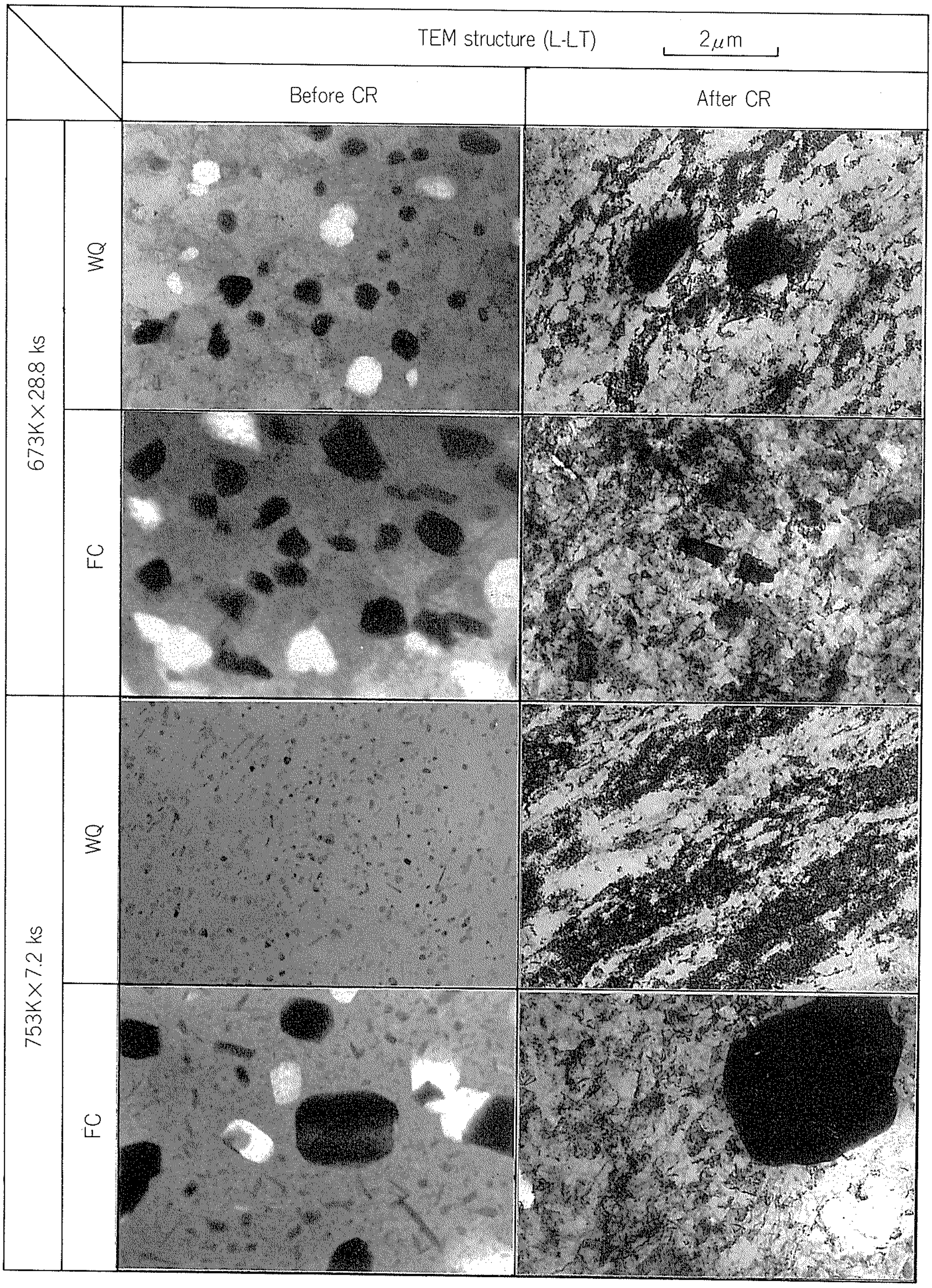

Fig. 7 Effect of typical precipitation process on TEM structures before and after cold working.

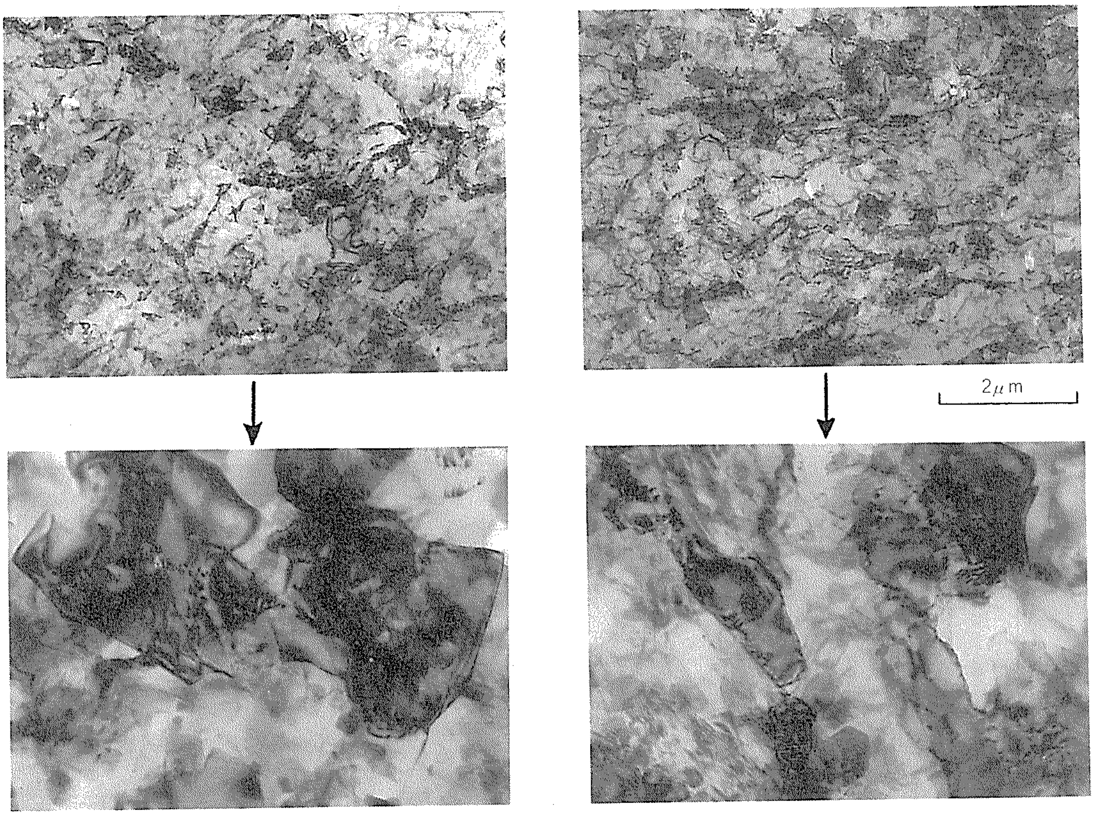

673K×28.8ks FC

753K×7.2ks FC

Fig. 8 TEM structures as cold-rolled. (Aged at 673K×28.8ks FC and 753K×7.2ks FC followed by cold rolling.)

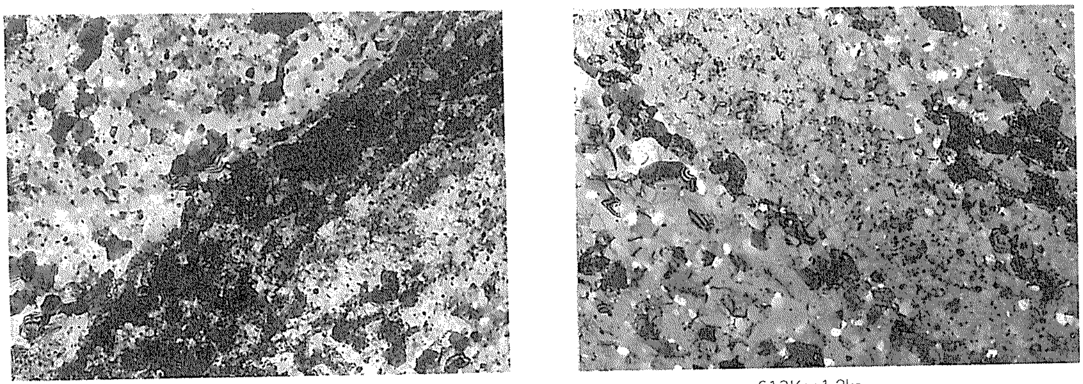

613K×0.3ks

613K×1.2ks

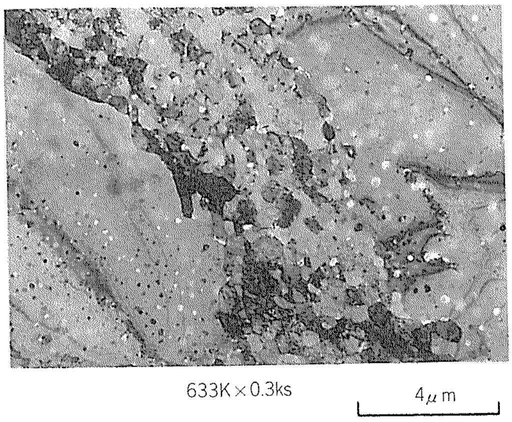

633K×0.3ks

Fig. 9 Structural changes during heating in a sheet aged at 753K×7.2ks WQ followed by cold rolling (90% reduction).

of a heterogeneous deformed structure. It is shown that the rate of recovery is different according to the dislocation density. The region with high dislocation density is slowly recovered because of the precipitation of supersaturated solute atoms.

The thermal stability of deformed structures is reflected into the exothermic curve of DTA or DSC. **Table 3** shows the temperature of the exothermic peak in DTA curves.

This peak, influenced by heating rate, shifts to higher temperature when the heating rate increases. In water-quenched materials followed by cold rolling, two peaks appear during heating. The first peak (lower temperature) corresponds to precipi-

Table 3 Temperature of exothermic peak in DTA curves.

Solution treatment	Precipitation Process	Temp. of exothermic peak (K)					
		50 K/min		200 K/min		400 K/min	
753K × 0.3ks WQ	673K × 28.8ks WQ	490	636	539	658	568	—
	673K × 28.8ks FC	—	633	—	671	—	686
	753K × 7.2ks WQ	492	671	546	691	568	703
	753K × 7.2ks FC	—	635	—	675	—	687

tation and the second one (higher temperature) does to recrystallization. The temperature of the second peak in 753K × 7.2ks WQ is higher by 20～40K than in other conditions. This result corresponds to the slow recovery of a heavily worked region shows in **Fig. 9**.

4. Mechanism of grain refinement

The mechanism of grain refinement in the typical precipitation process is discussed in the following.

The finest grain in this study is obtained in 673K × 28.8ks WQ. In this condition, the large second-

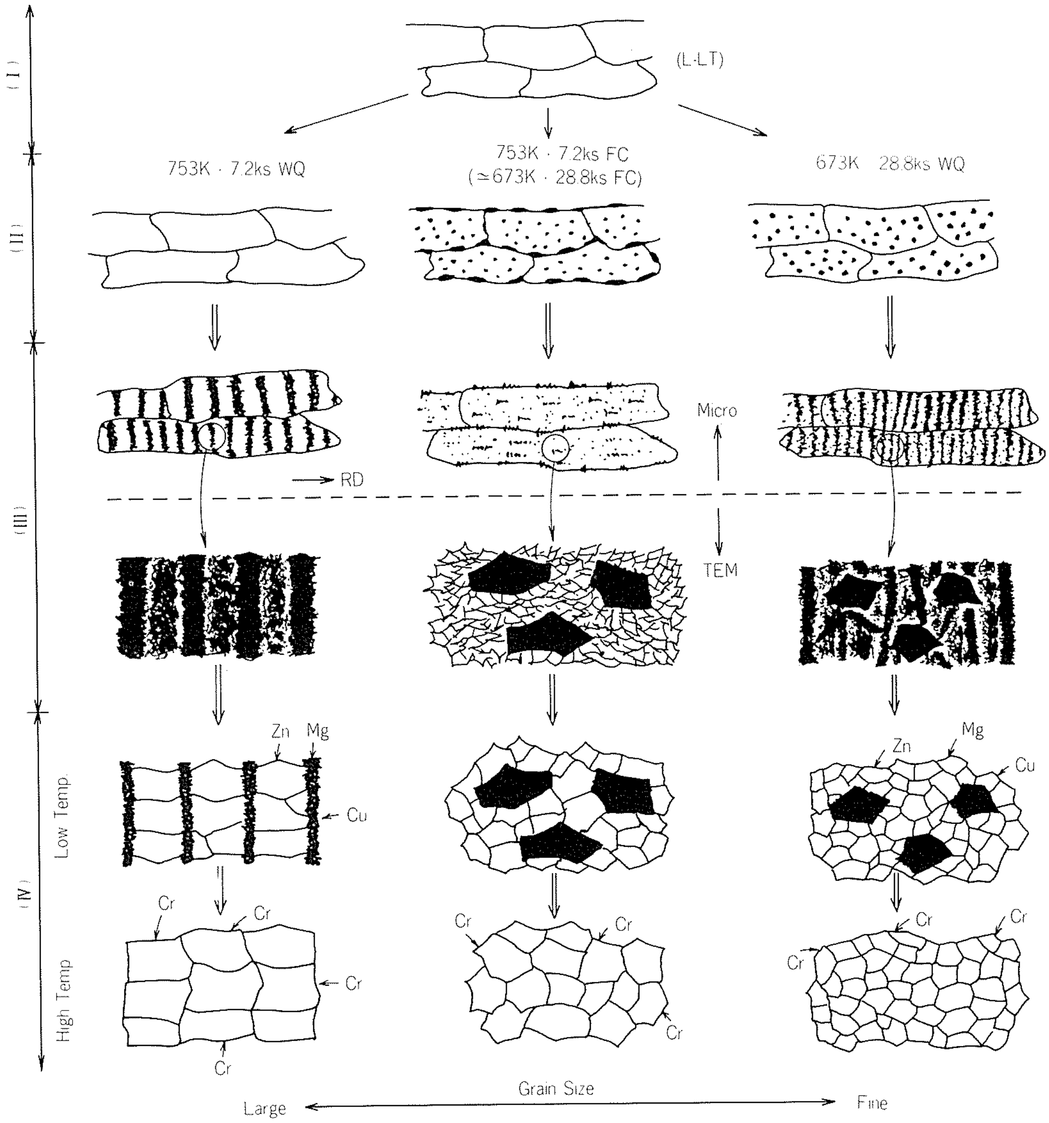
(I)
(II)
(III)
(IV)
Low Temp.
High Temp.
(L-LT)
753K · 7.2ks WQ
753K · 7.2ks FC
(≒673K · 28.8ks FC)
673K 28.8ks WQ
RD
Micro
TEM
Zn
Mg
Cu
Cr
Grain Size
Large
Fine

Fig. 10 Schematic diagram of grain refinement in an Al Zn-Mg-Cu-Cr alloy.
(I) Solution treatment (II) Precipitation
(III) Cold rolling (IV) Recrystallization

phase particles and supersaturated solute atoms coexist in the matrix prior to cold rolling. The large second-phase particles which have no coherency with matrix make the deformation homogeneous shown in **Figs. 6** and **7**. This means that multiple slip occurs during deformation. The multiple slip promotes the formation of sessile dislocations and dislocation networks. While the supersaturated atoms precipitate on the dislocations and their networks during cold rolling or heating. Further, in high temperature, the migration of boundaries of grain or subgrain is inhibited by precipitation of chromium. This is why the finest grain is formed. In slow heating, the migration and annhilation of dislocations becomes easier because of coagulation of precipitates which are pinning the grain boundaries at comparatively low temperature. This results in grain growth. When only supersaturated solute atoms exist and large particles are absent like 753K × 7.2ks WQ, the dislocation density becomes heterogeneous in the deformed structure. The grain size in this condition is controlled by the recovery of region with high dislocation density where supersaturated solute atoms precipitate, and therefore may be correlated with the spacing of shear bands. When supersaturated atoms do not exist like 753K × 7.2ks FC or 673K × 28.8ks FC, multiple slips caused by large particles produce cell structures during cold working. Then subgrains or fine grains are formed at comparatively low temperature and grain growth occurs gradually during heating. The grain size is determined by competition between the recovering rate of a deformed structure and the precipitating rate of solute atoms. Schematic diagrams of grain refinement described in the above is shown in **Fig. 10**.

5. Conclusion

A thermomechanical treatment was applied to grain refining of a high strength aluminium alloy sheet. This process has a four-step sequence, that is, solution treatment, precipitation, cold rolling and recrystallization. The conclusions obtained in this investigation are as follows:

(1) The solution treatment of a hot-rolled plate has little influence on grain size in recystallized sheets. The finest grain is obtained in aging at 673K × 28.8ks followed by quenching into water in the precipitation step. High reduction of thickness in cold rolling and rapid heating in recrystallization are effective to grain refinement.

(2) To obtain the finest grain, the coexistence of large second-phase particles which have no coherency with matrix and supersaturated solute atoms is required prior to cold rolling. The matrix with large particles is deformed homogeneously by multiple slip. Cell structures produced by multiple slip are stabilized by precipitation of supersaturated solute atoms at comparatively low temperature. At high temperature, the precipitation of chromium inhibits the migration of grain boundaries. The grain size is determined by competition between recovering rate and precipitating rate.

Reference

1) E. DiRusso, M. Conserva. M. Buratti and F. Gatto: Mat. Sci. Eng., **14** (1974), 23.
2) J. Waldman, H. Sulinski and H. Markus: Met. Trans., **5** (1974), 23.
3) J. A. Wert, N. E. Paton, C. H. Hamilton and M. W. Mahoney: Met. Trans., **12A** (1981), 1267.
4) C. C. Bampton, J. A. Wert and M. W. Mahoney: Met. Trans., **13A** (1982), 193.
5) Report of Advanced Aircrafts Technical Development Center, The Socicty of Japanese Aerospace Companies, Inc. No.802 (1984), No.901 (1985).

Reprinted from SUMITOMO LIGHT METAL TECHNICAL REPORTS (Title No. P-386)

論　　文

アルミ熱延における材料温度計算*

アルミ熱延の計算機制御のための検討，II

木　村　　　紘**

Temperature Calcuation in Hot Rolling of Aluminium

Computer Control of Hot Rolling of Aluminium, II

by Hiroshi Kimura

住友軽金属工業株式会社技術研究所

論　文

アルミ熱延における材料温度計算*

アルミ熱延の計算機制御のための検討，II

木村　紘**

Temperature Calcuation in Hot Rolling of Aluminium

Computer Control of Hot Rolling of Aluminium, II

by Hiroshi Kimura

Fundamental experiments on air cooling, spray cooling and hot rolling of aluminium were performed for determining the heat transfer coefficients in hot rolling process. And using these heat transfer coefficients, the temperature change of aluminium strip in hot strip mill line was calculated by the method of finite differences. The calculation results show that except in the roll gap, there is almost no temperature difference between the surface and the cross section center of the strip in case of aluminium, unlike in case of steel.

Therefore, for computer control, temperature model for calculating the mean strip temperature is necessary.

1. 緒　言

アルミニウム熱延における摩擦状態はすべり摩擦と固着摩擦が混在した，いわゆる，混合摩擦が支配的であり，適用する圧延理論としてはOrowan理論が適当である1)。また，圧延理論適用上の問題点の一つとして，圧延中の材料温度降下があり，場合によっては，それが100℃以上になることもあるのでその考慮が不可欠である1)。なぜならば，鉄鋼の場合，材料温度が100℃降下しても平均変形抵抗の増加は20%程度であるが2)，アルミニウムの場合は60%程度にもなるからである3)。

本報においては，圧延中の材料温度計算について報告する。従来の研究で明らかなように熱間圧延での材料温度変化は，(1) 圧延機の入側，出側における空中への輻射及び対流，(2) 圧延機入側におけるクーラントによる冷却，(3) 圧延中の塑性加工熱，ロールと材料表面との摩擦熱及びロールへの熱伝導によって決定される。それらを理論的に取扱った研究4) は多いが，アルミニウム熱延を対象とした例は少ない。また，熱間圧延全体を通して材料温度計算の理論値と実測値を比較した例はあるが，空冷，クーラント冷却，圧延の個々のプロセスを対象として理論値と実測値の比較を試みた例も少ない。

本報においては，まず，空冷実験，クーラント冷却実験，圧延実験を行い，理論と実験を対比させ，個々のプロセスにおける熱伝達率を決定する。次に，決定した熱伝達率を用い，差分法により実ラインにおける材料の板厚方向温度分布を計算し，計算機制御用の温度モデル作成上考慮すべき点を明らかにした。

2. 実 験 方 法

2.1 解析方法

熱間圧延での材料温度変化を検討する場合，熱延プロセスを空冷，クーラント冷却，圧延の3プロセスに分けて考えることができる。各プロセスにおける材料温度計算は差分法によるが，計算方法は基本的には従来の研究で明らかにされている4)。以下にその概略を箇条書きにする。

(1) 板厚をn等分し，式(1)に示す一次元非定常熱伝導方程式を差分化して板厚方向各点の温度推移を計算する。

$$C\rho\frac{\partial T}{\partial t}=\lambda\frac{\partial^2 T}{\partial x^2}+q \qquad \cdots\cdots(1)$$

ここで，Cは比熱(kcal/kg·℃)，ρは密度(kg/m^3)，λは熱伝導率(kcal/m·hr·℃)，Tは材料温度(℃)，tは時間(hr)，qは単位体積·単位時間当りの発熱量(kcal/m^3·hr)，xは材料厚さ方向座標(m)である。また，境界条件は板

---

* 軽金属，35 (1985)，381．に掲載

** 技術研究所プロセス研究部

表面において，式(2)で与えられる。

$$-\lambda\frac{\partial T}{\partial x}=Q \qquad \cdots\cdots(2)$$

ここで，Qは放熱の熱流束（kcal/m^2·hr）である。

(2) 空冷区間における輻射による放熱は式(3)で，対流による放熱は式(4)でそれぞれ表わされる。

$$Q_r=\sigma\varepsilon\left\{\left(\frac{T+273}{100}\right)^4-\left(\frac{T_A+273}{100}\right)^4\right\} \qquad \cdots\cdots(3)$$

$$Q_T=\alpha_T(T-T_A) \qquad \cdots\cdots(4)$$

ここで，Q_r, Q_Tは輻射，対流による熱流束(kcal/m^2·hr)，σはステファンボルツマン定数(=4.88kcal/m^2·hr·℃^{4})，εは輻射率(−)，T_Aは周囲温度(℃)，α_Tは対流熱伝達率(kcal/m^2·hr·℃)で自然対流の場合をα_N，強制対流の場合をα_Fとする。

(3) クーラント冷却区間における放熱は式(5)で表わされる。

$$Q_C=\alpha_C(T-T_C) \qquad \cdots\cdots(5)$$

ここで，Q_Cはクーラント冷却における熱流束(kcal/m^2·hr)，α_Cはクーラント熱伝達率(kcal/m^2·hr·℃)，T_Cはクーラント温度(℃)である。

(4) 圧延区間においては式(6)の塑性加工熱，式(7)の表面摩擦熱が発生し，式(8)に示す熱量がロールへの熱伝導で失われる。

$$Q_K=AK_{fm}\ln\left(\frac{h_1}{h_2}\right) \qquad \cdots\cdots(6)$$

$$Q_F=A\mu p_m v_{Rm} \qquad \cdots\cdots(7)$$

$$Q_R=\alpha_R(T-T_R) \qquad \cdots\cdots(8)$$

ここで，Q_Kは単位体積当りの材料に発生する塑性加工熱(kcal/m^3)，Aは仕事の熱当量(=1/427kcal/kg·m)，K_{fm}は平均変形抵抗(kgf/m^2)，h_1, h_2はそれぞれ入側厚(m)，出側厚（m）である。また，Q_Fは表面摩擦による熱流束(kcal/m^2·hr)，μは摩擦係数（−），p_mは平均圧延圧力(kgf/m^2)，v_{Rm}は材料とロールの相対速度の平均値（m/hr）である。また，Q_Rはロールへの熱伝導による熱流束(kcal/m^2·hr)，α_Rはロールと材料間の熱伝達率（kcal/m^2·hr·℃），T_Rはロール温度（℃）である。なお，v_{Rm}は式(9)で与えられる5)。

$$v_{Rm}=\frac{v_R(f^2+\varphi^2)}{2(f+\varphi)} \qquad \cdots\cdots(9)$$

Table 1 Conditions of air cooling tests.

Specimen	Initial temp. of specimen (℃)	Velocity of wind for air cooling (m/min)
Thickness×Width×Length (mm)		
2×350×350	420～430	0
5×350×350	〃	0, 100, 200, 300
10×350×350	〃	0

ここで，v_Rはロール周速（m/hr），fは先進率(−)，$\varphi=1-(1+f)(1-r)$，rは圧下率(−)である。

さて，上式において，塑性加工熱はn等分した材料要素のすべてに均等に発生するとする。すなわち，式(1)において$q=Q_K/t_R$，t_Rはロールと材料の接触時間(hr)である。表面摩擦熱の発生，ロールへの熱伝導損失は表面要素で行われるとし，かつ，表面摩擦熱については半分がロールへ伝導するとする。

さて，本報においては，まず空冷実験，クーラント冷却実験，圧延実験を行い，材料温度の計算値と実測値を比較することにより式(4)のα_T，式(5)のα_C，式(8)のα_Rを決定する。ついで，決定されたα_T, α_C, α_Rを用いて実ラインにおける材料の板厚方向温度分布のシミュレーション計算を行う。

2.2 空冷実験

供試材を炉中で所定温度に加熱し，約30min間保持後，台上に取り出し，供試材中に埋込んだ熱電対及び接触型表面温度計によって一定時間おきに測温した。熱電対は供試材の幅・長手方向の中央部，板厚方向中心部に埋込んだ。また，表面温度計での測温も熱電対埋込部を対象とした。空冷条件としては，自然対流の場合は空中にそのまま放置，強制対流の場合は供試材表面に平行に送風した。なお，供試材は台上で板幅両端を支えられており，測温点において上・下面に接触物はない。供試材は純アルミニウム1100である。実験条件をまとめて**Table 1**に示す。熱電対は保護管付きのCAで線径は1.6mmであり，応答性は記録計を含めて0～500℃で0.3secである。表面温度計は市販の接触型温度計で精度は±4℃，応答性は0～500℃で1secである。風速の測定は熱線風速計によった。供試材上での風速のばらつきは±15%であった。

2.3 クーラント冷却実験

供試材を炉中で所定温度に加熱し，約30min保持後台上に取り出し，クーラントで冷却しながら供試材中に埋込んだ熱電対によって測定した。使用したノズルは扇形スプレーノズルで，噴射形状が**Fig. 1**の斜線のような形状を呈するものである。実験は**Fig. 1**に示すように80mmピッチのノズルで，供試材に対して水平より30°の角度

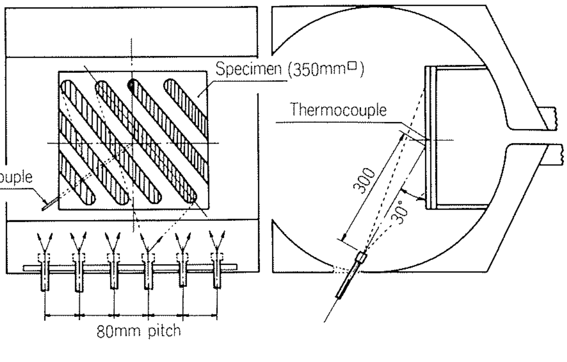

Fig. 1 Schematic diagram of experimental apparatus for spray cooling.

で300mm離した距離から冷却した。供試材は1100で，空冷実験で用いた試験片，熱電対及び記録計をそのまま用いた。実験条件をまとめて**Table 2**に示す。なお，ノズルと板の幾何学的関係，クーラント流量は実ラインを参考にして決定した。

2.4　圧延実験

実験用圧延機を用いてアルミニウム熱延実験を行った。供試材は1050，3003，5052の3合金で，寸法は2.0mm厚×80mm幅×500mm長である。圧延機はロール径が155mmの実験用圧延機，圧延条件は圧下率が20～50%，圧延速度が10m/min，平均圧延温度が200～400℃，潤滑は無潤滑及び市販圧延油約10%エマルジョンである。実験においては，ロール温度は予備圧延を行って予め上昇させ，実験中は50～60℃に保った。圧延油は材料に噴射せず，ロールに噴霧してロール入側での圧延油による材料温度降下を避けた。材料温度については，**Fig. 2**に示すように圧延前温度T_A(℃)，圧延後温度T_B(℃)を表面温度計にて測定し，同時に測温からロール入までの時間A(sec)，ロール出から測温までの時間B(sec)を測定する。以上のデータと材料の空冷曲線を用いてロールギャップ入側温度T_i(℃)，出側温度T_O(℃)を求め，圧延中の温度変化を推定した。

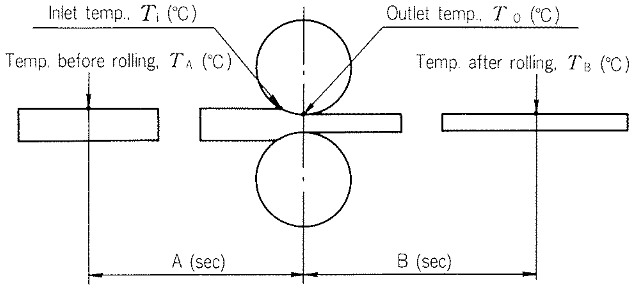
Inlet temp., T_i (℃)
Outlet temp., T_O (℃)
Temp. before rolling, T_A (℃)
Temp. after rolling, T_B (℃)
A (sec)
B (sec)

Fig. 2　Schematic diagram of measuring temperature (T_A and T_B) and time (A and B).

2.5　実ラインにおける材料温度シミュレーション

Fig. 3に示す3タンデムアルミニウム熱延ラインを対象として，前述の差分法で材料の板厚方向温度推移を計算した。図において，材料はNo.1スタンド前のA～B間で空冷，B～C間でクーラント冷却され，ついでC～D間で圧延される。以後，空冷・クーラント冷却・圧延を繰返して最終スタンドに至る。T_1，T_2は放射温度計である。圧延機はワークロール径が733mm，最大圧延速度が288m/min，主電動機出力が2,600kWの4重非可逆式圧延機である。対象とした材料は仕上厚が4～6mmの1100及び5052合金である。計算に当っては，**Table 3**に示す材料物性値[6]及び後述のように本研究で決定した熱伝達率を用いた。

3．結果及び考察

3.1　空冷，クーラント冷却及び圧延実験

空冷実験結果を**Fig. 4, 5**に示す。結果の整理に当っては初期温度が400℃となるように時間軸をずらせてある。図より板厚中心に埋込んだ熱電対による温度と表面温度計による温度とは，平均的にみて±5℃程度の差しかない。図中の実線は前述の差分法で計算した計算値である。ただし，板厚方向に10等分して温度分布を計算し

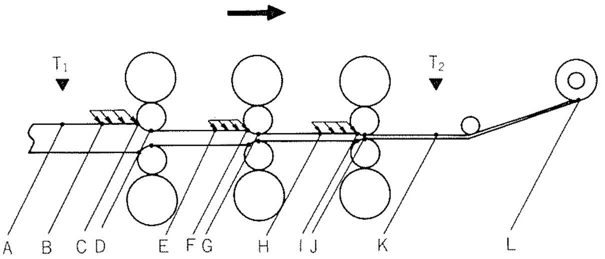

Fig. 3　Schematic layout of the hot strip mill line of aluminium.

Table 2　Conditions of spray cooling tests.

Specimen	Initial temp. of specimen (℃)	Coolant		
Thickness×Width×Length (mm)		10% emulsion	Temperature (℃)	Flow rate of spray (ℓ/min/nozzle)
10×350×350	420～430		54～72	15.8, 27.0, 35.0

Table 3　Physical properties of material[6] and heat transfer coefficients used in the calculation.

Material	Specific heat (kcal/kg/℃)	Density (kg/m³)	Thermal conductivity (kcal/m/hr/℃)	Emissivity (−)
Aluminium	0.22	2,700	175	0.06
Steel	0.11	7,830	46	0.79

Heat transfer coefficients (kcal/m/hr/℃)

Free convection	Forced convection	Spray cooling	Hot rolling of aluminium
Equ. (10)	Equ. (11)	Equ. (13)′	Equ. (14)

たところ，本条件下では板表面と板厚中央部の温度差は2℃以下であった。そこで，図では板厚方向10点の平均値を示してある。アルミニウムの熱伝導率が大きいこと，板厚が比較的薄いこと，空冷の熱伝達率が小さく表面が急冷されないことによって板厚方向の温度分布が殆んど生じないと考えられる。また，式(4)のα_Tは自然対流の場合をα_N，強制対流の場合をα_Fとし，**Fig. 4, 5**の温度実測値と計算値が一致するように式(10)及び式(11)を決定した。

$$\alpha_N = 1.99(T - T_A)^{0.25} \qquad \cdots\cdots(10)$$

$$\alpha_F = 2.97(1 + 0.0126V) \qquad \cdots\cdots(11)$$

ここで，Vは材料速度(m/min)である。対流熱伝達率の実験式は数多く発表されているが，適用条件が複雑で実用に供する場合には困難なことが多い。ここでは，自然対流についてはアルミニウムに対する適用を検討したKerthの式(10)′[7]，強制対流については乱流域に対する近似式である式(11)′[8]と本実験で得られた式(10)，(11)を比較する。**Fig. 6**に$T - T_A = 400$℃の場合について示す。本報の実験式が従来の実験式と大差ないことがわかる。

$$\alpha_N' = 1.64(T - T_A)^{0.25} \qquad \cdots\cdots(10)'$$

$$\alpha_F' = 5.11\frac{u^{0.8}}{l^{0.2}} \qquad \cdots\cdots(11)'$$

ここで，uは遠方の流速(m/sec)，lは板の長さ(m)である。

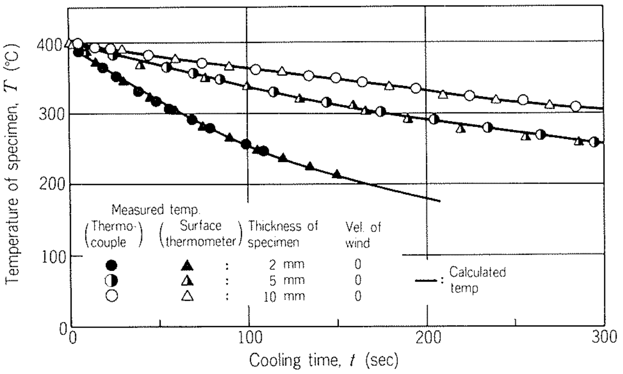

Fig. 4 Relation between temperature of specimen T and cooling time t in free convection.

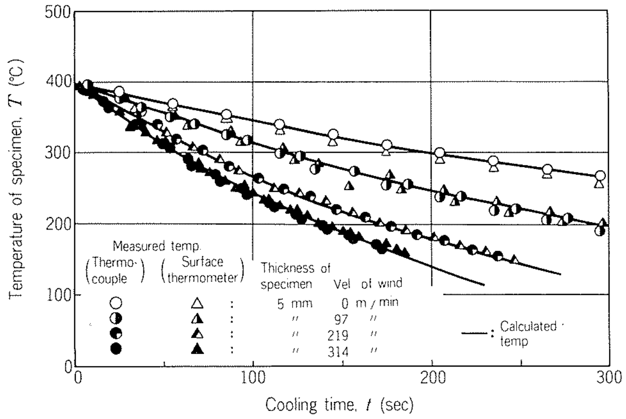

Fig. 5 Relation between temperature of specimen T and cooling time t in forced convection.

ある。

つぎに，クーラント冷却実験結果を**Fig. 7**に示す。図において時間軸の0はクーラントポンプ始動の瞬間であるが，別の実験で流量が所定値になるまで3～4 secかかることを確認しているので，**Fig. 7**の4 sec以降の測定値を整理の対象とする。差分法による計算値では板厚方向温度分布は4℃以下なので，近似的に温度分布がないとして式(12)でクーラント熱伝達率α_C(kcal/m²·hr·℃)を求めると，**Fig. 8**のようである。

$$\alpha_C = 3.6\times10^9\frac{C\rho h}{\Delta t}\ln\left(\frac{T_i - T_C}{T_f + T_C}\right) \qquad \cdots\cdots(12)$$

ここで，Cは比熱(kcal/kg·℃)，ρは密度(kg/mm³)，hは供試材厚さ(mm)，Δtは冷却時間(sec)，T_i，T_fは冷却前，後の板温度(℃)，T_Cはクーラント温度(℃)である。クーラント熱伝達率は板表面温度に影響されることが明らかにされているが[9]，**Fig. 8**では板温度が250～300℃に対して整理した熱伝達率である。**Fig. 8**よりα_Cの実験式として式(13)が得られる。

$$\alpha_C = 5{,}900\,v^{0.80} \qquad \cdots\cdots(13)$$

ここで，vは流量密度(m³/min·m²)であり，ノズル4.5個分の流量が材料に供給されるとして計算している(**Fig.**

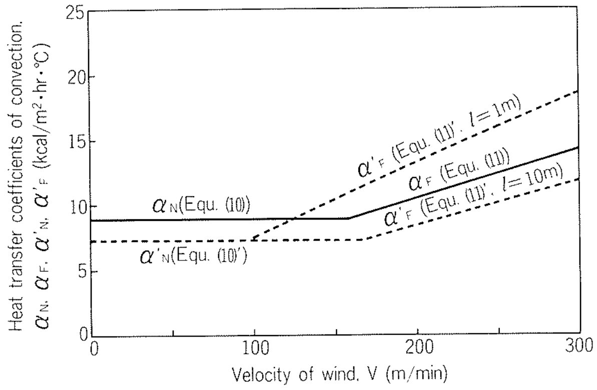

Fig. 6 Comparison of heat transfer coefficients of convection α_N, α_F (equ. (10), (11) and α_N', α_F' (equ. (10)′, (11)′).

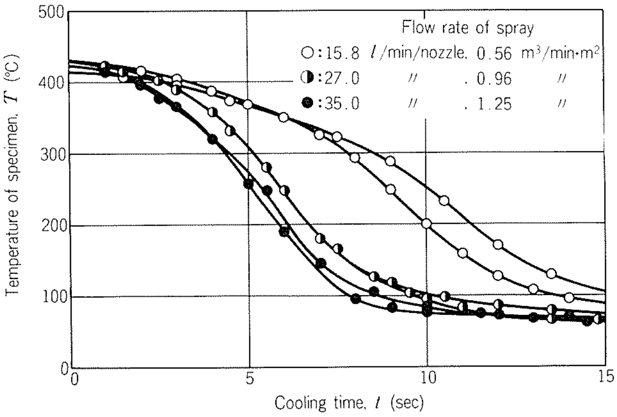

Fig. 7 Relation between temperature of specimen T and cooling time t in spray cooling.

1において，材料幅350mm/ノズルピッチ80mm=4.5である）。鋼板のスプレー冷却実験では，熱伝達率が流量密度の0.65～0.75乗に比例するという結果が報告されているが9)，式(13)もそれに近い結果を与えている。

つぎに，圧延実験結果について述べる。**Table 4** に温度及び時間の測定例を示す。表において，T_mは平均温度で1/2・(T_i+T_0)，T_dは降下温度でT_i-T_0で与えられる。表より，降下温度は1050>3003>5052であること，圧延油使用の場合が無潤滑の場合より大きいこと，平均温度が高いほど降下温度が高いことがわかる。**Table 5**に出側温度計算値T_0^C(℃)と実測値T_0^A(℃)の比較を示す。計算は前述の差分法によるが，摩擦係数μ及び平均変形抵抗K_{fm}は前報の値10)を，平均圧延圧力p_mは圧延荷重の実測値より求めた値を用いている。また，ロールと材料間の熱伝達率α_R(kcal/m^2·hr·℃)はロールギャップ出側温度の計算値と実測値が一致するように式(14)，(14)'を決定した。

$$\alpha_R=9,600t_R^{-0.5} \qquad \cdots\cdots(14)$$

$$\alpha_R=10,800t_R^{-0.5} \qquad \cdots\cdots(14)'$$

ここで，t_Rはロール接触時間（sec），式(14)は圧延油の場合，式(14)'は無潤滑の場合である。また，計算によると板厚方向の温度分布は10℃以内なので，**Table 5** の出側温度計算値としては板厚方向平均値を示してある。実測値と計算値の比較をすべてまとめて**Fig. 9**に示す。無潤滑の場合は誤差が大きいが，圧延油使用の場合は±10℃程度で温度予測が可能である。ところで，式(8)のα_Rについては従来より幾つかの式が提案されている。ロールと材料を完全接触の半無限体とし，一次元の熱移動問題として解くと式(15)となる4)。

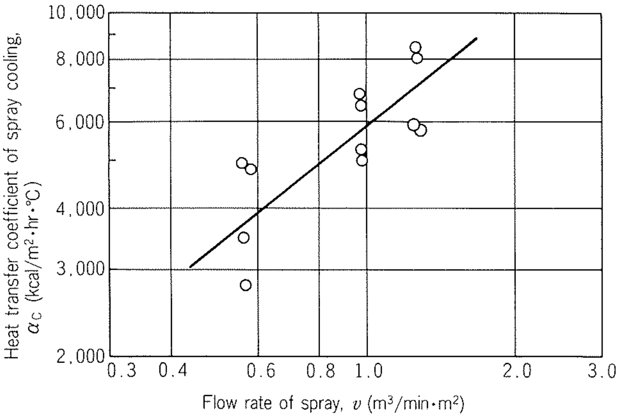

Fig. 8 Relation between heat transfer coefficient of spray cooling α_C and flow rate of spray v.

Table 4 Examples of measured temperature and time.

Material	Inlet thickness (mm)	Outlet thickness (mm)	Reduction (%)	T_A(1) (℃)	A(1) (sec)	T_i(1) (℃)	T_B(1) (℃)	B(1) (sec)	T_0(1) (℃)	Mean temp., T_m (℃)	Temp. drop, T_d (℃)	Lubricant
1050	2.023	1.344	34	390	6.2	378	179	3.9	183	281	195	10% emulsion
3003	1.987	1.375	31	291	7.3	276	149	3.7	152	214	124	
	1.988	1.340	33	380	7.0	360	184	2.9	187	274	173	
	1.991	1.343	33	545	6.0	527	248	3.0	252	390	275	
5052	1.536	1.173	24	352	6.0	339	181	2.8	186	263	153	
1050	2.023	1.444	29	350	6.2	338	186	3.7	191	265	147	None
3003	1.988	1.504	24	353	5.9	344	195	4.0	205	275	139	
5052	1.536	0.977	36	330	5.5	318	190	3.0	193	256	125	

(1) Refer to **Fig. 2.**

Table 5 Examples of calculated temperature at the exit of roll gap.

No.	Material	Inlet thickness (mm)	Outlet thickness (mm)	Rolling force (kgf)	Forward slip (%)	Friction coeff. (−)	Surface temp. of roll (℃)	Entry temp. measured (℃)	Exit temp.		Lubricant
									measured T_0^A(℃)	calculated T_0^C(℃)	
1	1050	2.023	1.344	7080	4.6	0.10	59	378	183	182	10% emulsion
2	3003	1.988	1.340	6300	0	0.04	63	360	187	184	
3	5052	1.536	1.173	12085	2.4	0.07	63	339	186	179	
4	1050	2.023	1.444	10816	7.7	0.64	53	338	191	175	None
5	3003	1.988	1.504	11413	6.6	0.64	49	344	205	185	
6	5052	1.536	0.977	37072	10.1	0.64	51	318	193	234	

$$\alpha_R = \frac{2\,\mathrm{b_a b_s}}{\sqrt{\pi}\,(\mathrm{b_a} + \mathrm{b_s})}\, t_R^{-0.5} \qquad \cdots\cdots(15)$$

ここで，$\mathrm{b_a} = \sqrt{\lambda_a C_a \rho_a}$（$\lambda_a$，$C_a$，$\rho_a$：アルミニウムの熱伝導率，比熱，密度），$\mathrm{b_s} = \sqrt{\lambda_s C_s \rho_s}$（$\lambda_s$，$C_s$，$\rho_s$：ロールの熱伝導率，比熱，密度）である。式(15)に **Table 3** の物性値を代入すると，$\alpha_R = 8{,}700 t_R^{-0.5}$となる。一方，Kerthはアルミニウムに対して式(16)に相当する式を与えている7)。両式を本報の式(14)，(14)′と比較すると，±25%の範囲で一致する。

$$\alpha_R = 11{,}800 t_R^{-0.5} \qquad \cdots\cdots(16)$$

3.2　実ラインにおける材料温度シミュレーション

差分法の計算にあたって，熱伝達率は原則として前述の実験で決定した **Table 3** に示す値を用いた。ただし，式(13)のクーラントの熱伝達率α_Cは第3スタンド出側の表面温度の実測値と計算値が一致するように式(13)′のように補正している。大幅な補正の理由は以下のようである。

(1)　式(13)はノズル直下での連続的な冷却に対する熱伝達率であるが，式(13)′は冷却長を1mと仮定した直下～1mの平均熱伝達率である。実験によると直下を1.0とすると，250mm離れた点での熱伝達率は0.56となる。熱伝達率は直下から離れるにつれて指数関数的に減少すると推定される。直下～1,000mmを指数関数で近似し，平均熱伝達率を求めると，直下の1.0に対して平均値は0.39となる。

(2)　式(13)に(1)の補正を加えると，係数は5,900×0.39＝2,300となる。さらに，式(13)′では表面温度の実測値と計算値が一致するように1,880と補正している。

$$\alpha_C = 1{,}880 v^{0.80} \qquad \cdots\cdots(13)' \ {}^{*1}$$

計算結果を **Fig. 10** に示す。図よりロール直下では表面と中心で温度差が最大60℃生じているが，ロール出側では板内部の熱伝導により瞬時にして温度差がなくなること，クーラント冷却では殆んど温度差が生じないことがわかる。参考のため，図中に材料が鉄鋼で入側温度が1,020℃，圧延条件はアルミニウムと同じ場合についての計算値を示す。鉄鋼の場合は相対的に熱伝導率が低く，かつ，周囲との温度差が大きいので表面が急冷され，ロール直下で最大100℃程度，クーラント冷却で最大20℃程度の温度差を生じている。

アルミニウムの場合，最終スタンド出側では表面と中心で温度差は殆んどない。このことから，最終スタンド出側の温度を所定値にする温度制御の立場からは，温度計算式として板厚方向の分布を考える必要がないことがわかる。また，圧延荷重，圧延トルクの計算の立場からも同様のことがいえるので，計算機制御のための温度計算式としては板厚方向の分布を考慮しない平均的温度が計算できればよい。従って，差分法による必要はなく，計算機制御のための簡略な計算式を決定することが可能である。これについては次の機会に述べる。

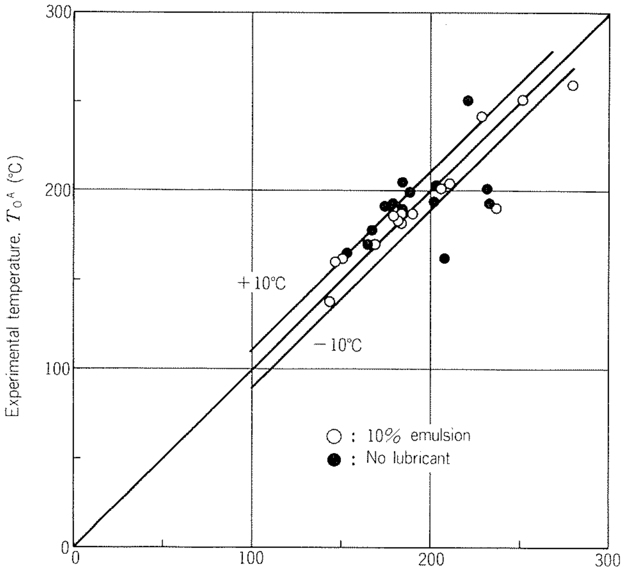

Fig. 9　Comparison of experimental temperature T_0^A and calculated temperature T_0^C at the exit of roll gap.

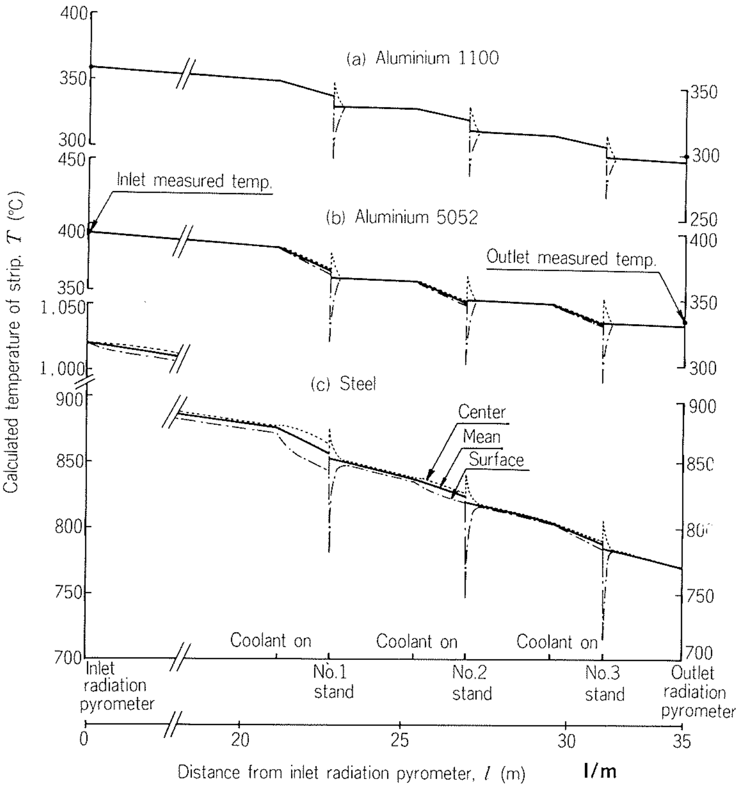

Fig. 10　Calculated temperature change of strip in the hot strip mill line.

---

*1　既発表の軽金属，**35**(1985)，381における式(13)′のvは，材料冷却用，ワークロール冷却用及びバックアップロール冷却用の3種類のクーラント流量の和である。一方，本論文のvは単に材料冷却用のクーラント流量のみである。

4. 結　　論

本報においては，アルミニウム熱延における材料温度計算について検討した。すなわち，まず空冷実験，クーラント冷却実験，圧延実験を行い，個々のプロセスにおける熱伝達率を決定した。ついで，実ラインにおいて差分法により材料の板厚方向温度分布推移の計算を行った。結果を要約すると以下のようである。

(1) 空冷実験によりアルミニウムを対象とした対流熱伝達率の式を決定した。それによれば，自然対流についてはKerthの式[7]で計算された値は本研究で導出された式よりも20％小さい。また，強制対流については材料移動速度の一次式で与えればよい。

(2) 流量密度が実機規模相当のクーラント冷却実験によりクーラント熱伝達率式を作成した。それによると，熱伝達率は流量密度の0.8乗に比例する。

(3) 圧延実験を行い，圧延前後の材料温度を測定することにより，ロールと材料間の熱伝達率を推定した。それによれば，得られた熱伝達率はロール・材料を完全接触の半無限体とした一次元熱解析で得られる値あるいはKerthの値と±25％の範囲で一致した。

(4) 以上の実験で決定した熱伝達率を用い，実ラインについて差分法により材料の板厚方向温度分布推移を計算した。その結果，通常の操業条件ではロール直下では板表面と中心で最大60℃程度の温度差が生ずるが，ロール出側では板内部の熱伝導により瞬時にして温度差がなくなること，クーラント冷却では表面と内部で殆んど温度差が生じないことが明らかになった。従って，計算機制御のための温度計算式としては，板厚方向分布を考慮しない平均的温度が計算できればよいことが明らかになった。

参　考　文　献

1) 木村紘：軽金属，**35** (1985)，222.
2) 美坂佳助，吉本友吉：塑性と加工，**8** (1967)，414.
3) 千田憲雄，木村紘，馬場義雄：住友軽金属技報，**19** (1978)，(1978)，3.
4) 例えば小門純一：塑性と加工，**11** (1970)，816.
5) 吉田博，他5名：塑性と加工，**23** (1982)，63.
6) 日本機械学会編：**伝熱工学資料**，改訂第3版，(1976)，148.
7) W. Kerth : Aluminium, **51** (1975)，570.
8) 日本機械学会編：**機械工学便覧**，改訂第4版，(1961)，11－25.
9) 三塚正志：鉄と鋼，**54** (1968)，1457.
10) 木村紘：住友軽金属技報，**26** (1985)，189.

Reprinted from SUMITOMO LIGHT METAL TECHNICAL REPORTS (Title No. P-387)

論　文

サークルアレイ超音波探触子についての二, 三の実験*

高 橋 伸 幸**

Experimental Study for Phase Steered Ultrasonic Circle Array

by Nobuyuki Takahashi

住友軽金属工業株式会社技術研究所

論　文

サークルアレイ超音波探触子についての二，三の実験*

高橋伸幸**

Experimental Study for Phase Steered Ultrasonic Circle Array

by Nobuyuki Takahashi

Recently, ultrasonic testing is one of the most effective and reliable nondestructive test method to meet the demand of quality for heat exchanger tubes. But there are some problems awaiting solution in ultrasonic testing.

This paper discusses the sound field characteristics of circle array in term of the design parameters of phase steered element numbers, element width and element spacing, and the artificial flaw detection sensitivity in trial circle array. The principle is based on phase steered ultrasonic linear array technology.

Experimental values by the circle array are equivalent to theoretical ones in the sound field characteristics and it is estimated that the circle array is the same to a line focus transducer in the artificial flaw detection sensitivity.

1. はじめに

熱交換器用薄肉管は高信頼性が要求され，その欠陥検査には渦流探傷あるいは超音波探傷検査が用いられているが，欠陥には多くの種類と形状があるので，品質保証の上から両者の併用が望ましい。しかし，超音波探傷検査においては，超音波探触子（以下，探触子と称する）を管円周方向に高速で回転させるもの[1]と，管円周方向に探傷子を多数個配置する方法とがあり，いずれも装置が高価格な上に，初期設定に時間を要する。これらに代る方式として，リニアアレイ探傷の理論[2,3,4]を用いたサークルアレイ探傷方式を検討し，その探触子を試作した。すなわち，振動子を環状に多数個配列し，本報では，その設計因子である駆動振動子数，振動子幅，振動子ピッチと超音波ビームの指向性等の関係を求めると共に，人工欠陥を外表面にもつ熱交換器用チタニウム溶接管についてその検出能を検討した。

2. サークルアレイ探傷検査

2.1 リニアアレイ探傷検査

リニアアレイ探傷検査は，電子走査形超音波探傷装置と超音波振動子（以下，振動子と称する）を直線状に多数個配列したアレイ形探触子を用い，超音波ビームを任意の方向に集束・偏向させて探傷を行うものである。

リニアアレイ探傷の原理を**Fig. 1**に示す。各振動子間の駆動タイミングを，一番端の振動子から順次遅延させて電子走査することにより，各振動子から放射された超音波の波面は，互いに干渉して超音波ビームが合成される。超音波ビームは遅延時間をリニアにすれば，振動子面に斜めに進行し，また，遅延時間を円弧にすると，超音波ビームはある一点に向って集束する。従って，超音波ビームは，各振動子間の遅延時間を変えることにより任意の進行方向をえらぶことができる。この超音波ビームが欠陥に当ると反射し，その反射波は球面状に広がって振動子へ戻ってくる。各振動子が受信した反射波に対して遅延時間を与えた後に加算すると，送信方向からの反射波のみ波面が強くなり，強い受波指向性が得られる。

2.2 サークルアレイ探傷検査

サークルアレイ探傷検査は，理論的にはリニアアレイ

---

* 日本非破壊検査協会　昭和60年度秋季大会（10月16～17日，於・仙台）にて一部発表,「管の超音波用サークル状リニアアレイ探触子の開発」を改題

** 技術研究所プロセス研究部

探傷検査と同じであり，後者の振動子配列が直線状であるのに対し，振動子を環状に配列したものである。従って，リニアアレイ探触子との形状の相違から生じる超音波ビーム路程差を遅延時間で補正しなければならない。

サークルアレイ探傷検査の概念を**Fig. 2**に示す。超音波ビームを管表面附近に集束・偏向させ，配列した環状振動子の中心位置を管が通過する際に探傷検査を行うわけであり，環状振動子と被探傷管の間には水を媒質として用いる。この方式は，電子走査により振動子の駆動を順に行って管の全周を高速で探傷するため，機械的な回転部分[1]がなく，また，装置が小型となり，かつ，初期設定が容易となる。

2.3　超音波ビームの指向性

幅wの線状振動子の指向性を $D_w(\theta)$ とすると，式(1)のように表わされる[5]。（**Fig. 3**参照）

$$D_w(\theta)=\sin\phi_w/\phi_w \qquad \cdots\cdots(1)$$

$$\text{ここに，}\ \phi_w=\frac{w\pi\sin\theta}{\lambda}$$

λ：媒質中の波長，（水の場合，$\lambda=0.298\mathrm{mm}$）

また，n 個の点音源を直線状にピッチ p で配列したときの指向性 $D_p(\theta)$ は，n が偶数と奇数の場合とでは異なり，式(2)，(3)で示される[6]。

$$n=\text{偶数}：\quad D_p(\theta)=\Big[\sum_{i=1}^{n/2}A_i\Big]^{-1}\sum_{i=1}^{n/2}A_i\cos(2i-1)\phi_p \qquad \cdots\cdots(2)$$

$$\text{ここに，}\ \phi_p=\frac{p\cdot\pi\cdot\sin\theta}{\lambda}$$

A_i：i 番目の点音源の振幅

$$n=\text{奇数}：\quad D_p(\theta)=\Big[\sum_{i=0}^{(n-1)/2}A_i\Big]^{-1}\sum_{i=0}^{(n-1)/2}A_i\cos 2i\phi_p \qquad \cdots\cdots(3)$$

偏向した超音波ビームの合成指向性 $D_t(\theta)$ は，振動子各々の指向性と，各振動子の中心に点音源を配列したときの指向性との積であり，式(4)で表わされる。

$$D_t(\theta)=D_w(\theta)\cdot D_p(\theta) \qquad \cdots\cdots(4)$$

$D_t(\theta)$，$D_w(\theta)$，$D_p(\theta)$は，実際にはθにおける音圧を$\theta=0$のときの音圧で除した値である。

(1)　駆動振動子数による影響

後述の試作したサークルアレイ探触子（$w=1.1\mathrm{mm}$，$p=1.4\mathrm{mm}$，周波数$f=5\,\mathrm{MHz}$）の$D_t(\theta)$を$n=1\sim8$の場合について式(4)から求めた結果を**Fig. 4**に示す。**Fig. 4**において，$D_t(\theta)$が$0\sim1.0\sim0$の範囲を主極(main beam)，それ以外の凹凸を副極（side lobe）という。主極の$D_t(\theta)$

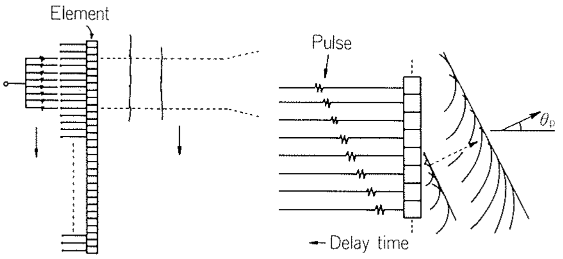
Element
Pulse
θp
Delay time

(a) Scanning　(b) Deflection

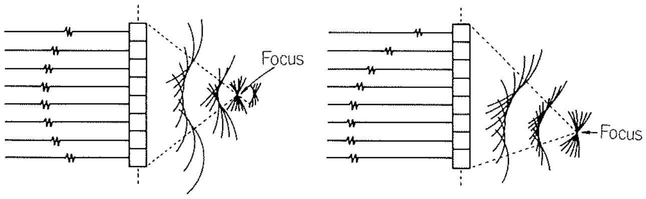
Focus
Focus

(c) Focusing　(d) Deflection+focusing

Fig. 1　Phase steered ultrasonic linear array technology.

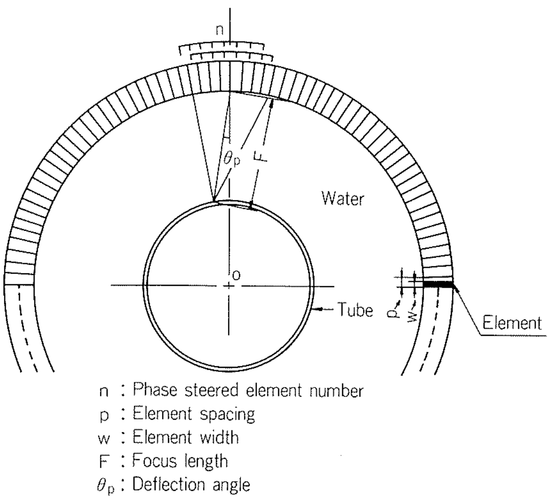
n
θp
F
Water
o
Tube
p
w
Element
n : Phase steered element number
p : Element spacing
w : Element width
F : Focus length
θp : Deflection angle

Fig. 2　Phase steered ultrasonic circle array.

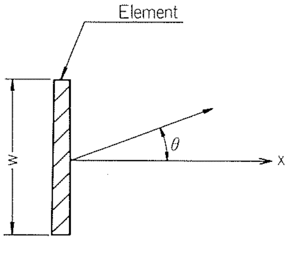
Element
w
θ
x

Fig. 3　Emission from a single array element.

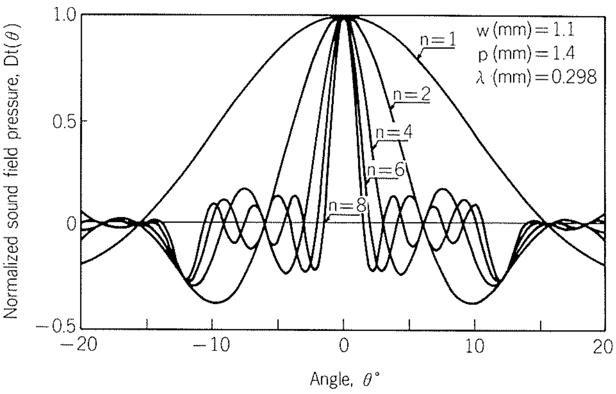

Fig. 4　Theoretical values of the sound field pressure distribution.

は，nが多くなると鋭くなり，画像表示した場合には虚像の原因となる副極の高さは小さい。副極の発生は，超音波ビームを集束する場合に有限の大きさの振動子に対して遅延時間を与えて行うので，遅延時間が連続とならず，位相加算された波面は完全な凹面とならないためである。また，振動子の形状は矩形板を用いるから，その形状比（振動子の厚さtと幅wの比，t/w）も副極発生の原因となる。

(2) 振動子ピッチによる影響

前項の探触子において，n＝8として0.2mm間隔でp＝1.2～2.0mmと変えた場合の$D_t(\theta)$を求めた結果を**Fig. 5**に示す。主極の$D_t(\theta)$はpが大きくなるにつれて鋭くなるが，副極の高さは変らないことがわかる。

(3) 振動子幅の影響

同様にn＝8として，0.2mm間隔でw＝0.4～1.2mmと変えた場合の$D_t(\theta)$を**Fig. 6**に示す。主極の$D_t(\theta)$は，この程度のwの範囲では差が殆んど認められず，副極の高さも変わらない。

2.4 グレーティングロブ発生角

探触子はn個の振動子より構成されている。従って，**Fig. 7**に示すように，主極方向以外に隣接振動子によって超音波の位相が整数波長ずれた方向にも合う波面を生じ，それをグレーティングロブ（grating lobe）という。1波長ずれたグレーティングロブの伝搬方向θ_gを式(5)に示す[5)]。

$$\theta_g = \sin^{-1}\{(\sin\theta_p) \pm \lambda/p\} \qquad \cdots\cdots(5)$$

ここに，θ_p：主極の偏向角

θ_gはn個の振動子の中心における法線からの傾きであり，法線に対してθ_pの反対側を負とする。媒質は水なのでλ＝0.298mmとなり，θ_gはθ_pとpの関数となる。θ_pを0～8°，0.2mm間隔でp＝1.2～2.0mmと変えた場合のθ_gを式(5)から求めて**Fig. 8**に示す。**Fig. 8**からわかるように，θ_pまたはpが大きくなるにつれてθ_gは小さくなる。

θ_gが小さくなると，グレーティングロブの裾野のビームが探傷する管の中心に向くため，管表面からの反射エコーが大きくなって，主極入射点近辺の探傷が難しくなるので望ましくない。

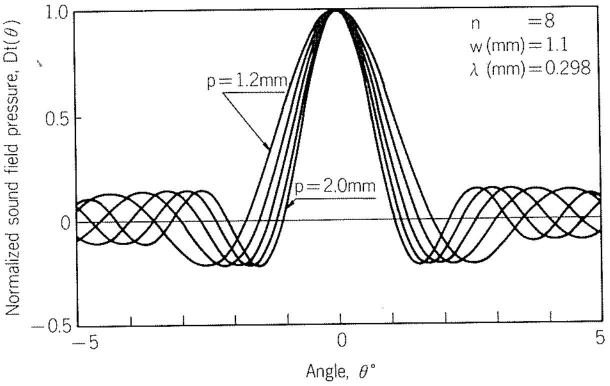

Fig. 5 Theoretical value of the sound field pressure distribution.

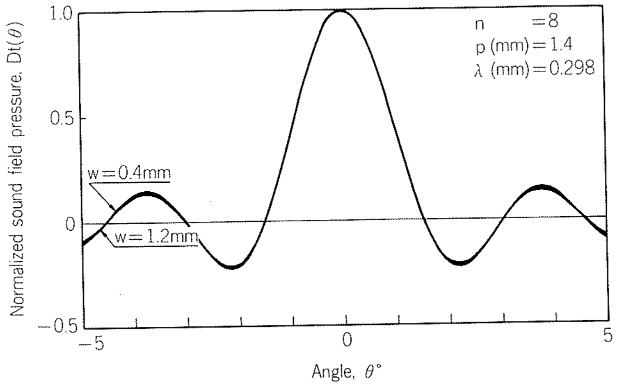

Fig. 6 Theoretical value of the sound field pressure distribution.

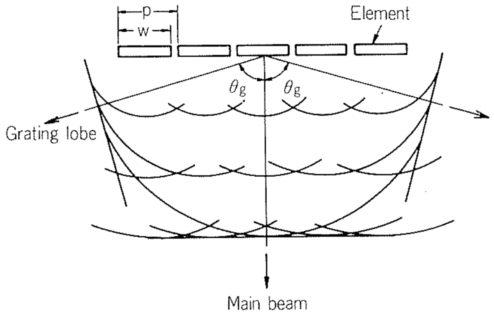

Fig. 7 Propagation of grating lobe.

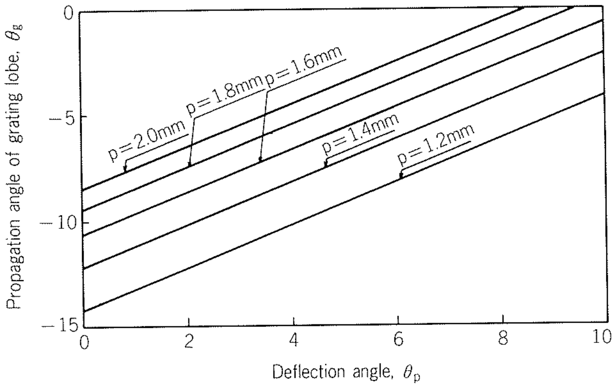

Fig. 8 Relation between deflection angle and propagation angle of grating lobe.

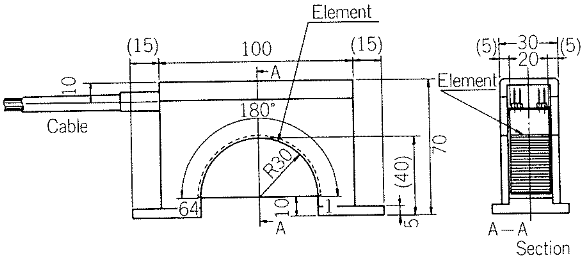

Fig. 9 Phase steered ultrasonic circle array.

3. サークルアレイ探傷実験

3.1 試作サークルアレイ探触子

試作したサークルアレイ探触子の形状は**Fig. 9**に，仕様を**Table 1**にそれぞれ示す。振動子の材質は，ジルコン酸チタン酸鉛である。n 個の振動子の音圧の測定には**Fig. 10**に示す音圧反射装置（反射体は直径0.8mm，長さ40mmの鋼針）を用い，媒質は水である。なお，使用した超音波探傷装置は，デジタル制御可能な(株)東芝製AU100型であり，パルサーチャンネル数は，64個である。

3.2 音圧分布測定結果

(1) 単一振動子の指向性

n＝1のときの$D_w(\theta)$の実測値を式(1)からの理論値と比較して**Fig. 11**に示す。両者はほぼ一致していることがわかる。

(2) 集束・偏向状況

n＝8，焦点距離F＝20mmとして，θ_pを変えた場合の焦点近傍での音圧分布測定結果を**Fig. 12**に示す。θ_pを大きくするにつれて主極の音圧が低下し，グレーティングロブの発生が顕著となる。主極の偏向は，設定と測定結果との間にずれがあるが，これは反射体の位置設定誤差が最大1 mm（$\theta_p=2.9°$に相当）あるためである。偏向による主極の音圧は**Fig. 13**からわかるように式(1)に，また，グレーティングロブの発生角は**Fig. 14**に示すように式(5)と，それぞれほぼ一致している。

(3) 主極の音圧と幅

振動子形状が円板の場合，中心軸上の音圧は測定位置Xが遠距離の場合には，式(6)で表わされる[7]。

$$P = P_0 \pi a^2 / \lambda X \qquad \cdots\cdots(6)$$

ここに，a：円板の半径
P_0：振動子直前の平均音圧

Table 1 Specification of phase steered ultrasonic circle array.

Frequency,	f(MHz)	5
Element width,	w(mm)	1.1
Element spacing,	p(mm)	1.4
Element number,	N	64
Element length,	L(mm)	20
Radius of half circle,	R(mm)	30

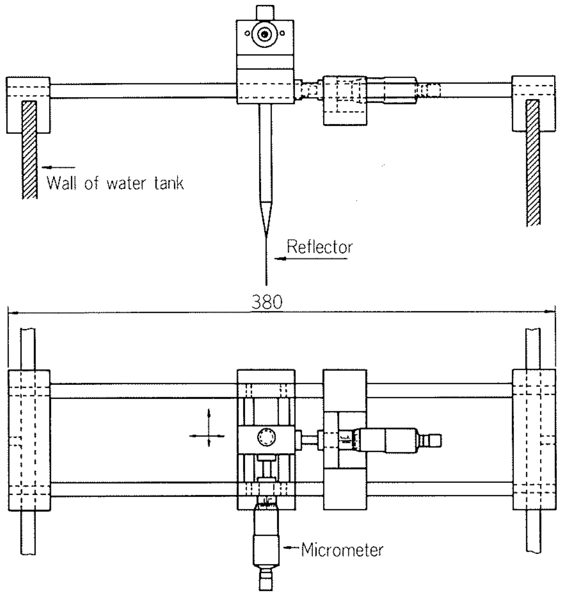

Fig. 10 Reflect calibrater.

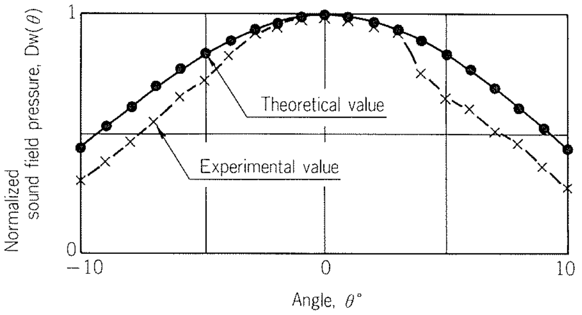

Fig. 11 The sound field pressure distribution of a single array element.

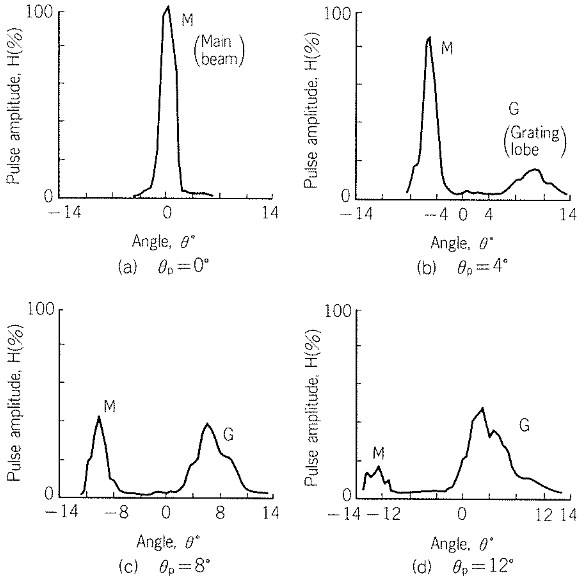

(a) $\theta_p=0°$　(b) $\theta_p=4°$
(c) $\theta_p=8°$　(d) $\theta_p=12°$

Fig. 12 Sound field pressure distribution by the circle array. (Focus length F : 20mm)

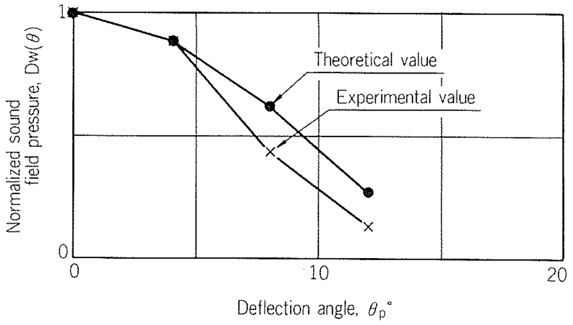

Fig. 13 Main beam intensity.

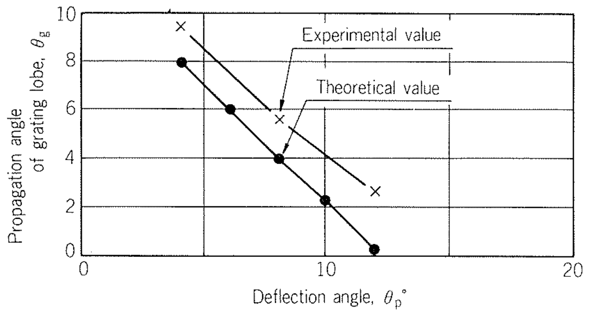

Fig. 14　Propagation angle of grating lobe.

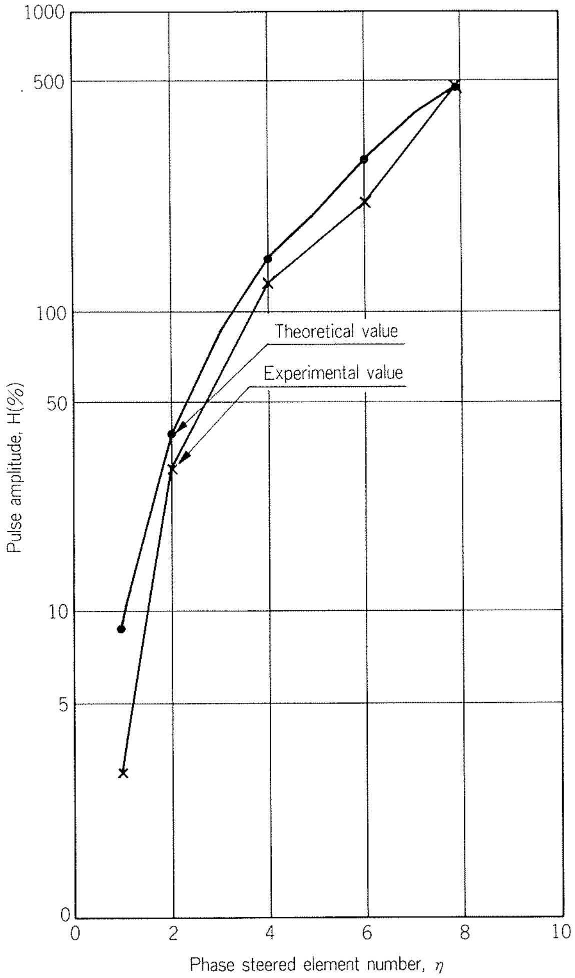

Fig. 15　Main beam intensity.

振動子形状が矩形板の場合も円板と同様，中心軸上の音圧は振動子の面積に比例すると考えられる。しかし，音圧をエコー高さで表示する場合には，音圧は振動子の電気音響変換損失により振動子の面積の２乗に比例する[8]。**Fig. 15**にｎと主極の音圧，**Fig. 16**にｎと主極の幅（ピーク感度より 6 dB downさせたときの幅）の関係をそれぞれ示す。いずれの場合も，実測値は測定値とよく一致していることがわかる。すなわち，n が多くなるに従って主極音圧は高くなり，主極の幅は小さくなって $D_t(\theta)$ が鋭くなる。

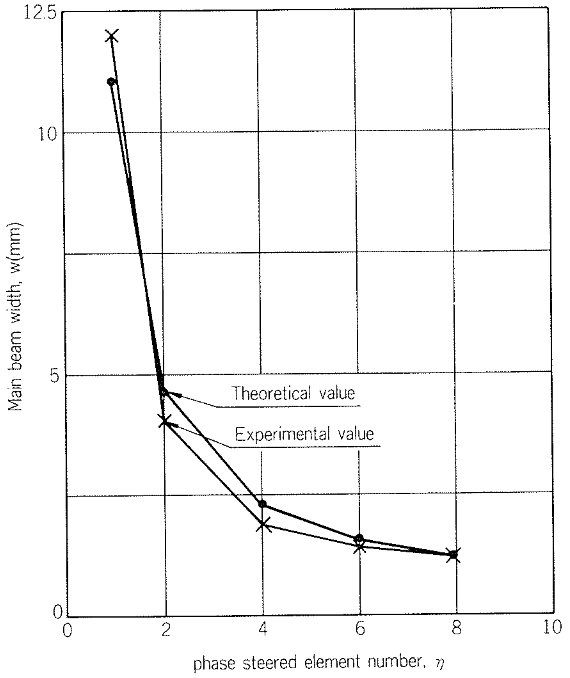

Fig. 16　Main beam width.

Table 2　Sensitibity by phase steered ultrasonic circle array and point focus transducer.

Tube (Diameter× Thickness, mm)	Artificial flaw dimension (Width×Length, mm)	S/N Ratio	
		Line focus transducer	Circle array
12.7 ×0.7	0.05×15	6.0	4.0
19.05×0.7	0.08×10	7.0	3.5

3.3　人工欠陥検出能

熱交換器用チタニウム溶接管の外表面に設けた人工欠陥に対するラインフォーカス形探触子と試作サークルアレイ探触子による検出能を，**Table 2** に示す。なお，供試管への超音波ビームの入射は，板波 A_0 モード発生入射角にて行った。試作サークルアレイ探触子の長さ L＝20mm，ラインフォーカス形探触子の焦点位置でのビーム長さ l＝ 6 mmを考慮すれば，サークルアレイ探触子とラインフォーカス形探触子の人工欠陥検出能は，同等と推定される。

4. ま　と　め

本報では，サークルアレイ探触子を設計するときに必要となる駆動振動子数，振動子幅，振動子ピッチと超音波ビームの指向性等の関係を理論式から求めた。また，サークルアレイ探触子を試作し，理論式との適合性並びに人工欠陥の検出能について検討した。得られた結果は以下のようである。

(1)　駆動振動子数が多くなるに従い，主極の指向性は鋭くなり，主極の強度も強くなる。

(2)　振動子ピッチが大きくなるにつれて，主極の指向性は鋭くなる。

(3)　振動子幅0.4～1.2mmの範囲では，主極の指向性は変わらない。

(4)　単一振動子の指向性により，主極の強度が決定される。

(5)　主極の強度は偏向を大きくするにつれて弱くなりグレーティングロブが顕著になる。

(6)　試作サークルアレイ探触子の人工欠陥検出能は，ラインフォーカス形探触子と同等である。

本方式による探傷検査は，従来方式と比べて装置の価格が安価となり，初期設定にそれほど時間を要しない利点をもつが，装置の実用化には探傷速度，振動子間の感度差等未解決の点があるので，更に今後の研究が必要である。

文　献

1)　鷲田理雄，金森照夫，野世渓精：本誌，**19**（1978)，168.
2)　長井敏，内田邦治：**NDI資料**，春期大会講演概要（1981)，114.
3)　岩崎全良：**NDI資料**，No.2915（1982)，1.
4)　土屋武雄，玉木清英，小菅英男：**NDI資料**，No.2979（1983)，31.
5)　D. K. Lemon and G. J. Posakony：Mat. Eva., **38**（1980)，34.
6)　小島正：**医用超音波機器ハンドブック**，コロナ社，(1980)，57.
7)　日本非破壊検査協会編：**超音波探傷試験B**，(1979)，15.
8)　前出7)，16.

Reprinted from SUMITOMO LIGHT METAL TECHNICAL REPORTS (Title No. P-387)

住友軽金属工業株式会社技術研究所

論　文

サークルアレイ超音波探触子についての二，三の実験*

高橋伸幸**

Experimental Study for Phase Steered Ultrasonic Circle Array

by Nobuyuki Takahashi

Recently, ultrasonic testing is one of the most effective and reliable nondestructive test method to meet the demand of quality for heat exchanger tubes. But there are some problems awaiting solution in ultrasonic testing.

This paper discusses the sound field characteristics of circle array in term of the design parameters of phase steered element numbers, element width and element spacing, and the artificial flaw detection sensitivity in trial circle array. The principle is based on phase steered ultrasonic linear array technology.

Experimental values by the circle array are equivalent to theoretical ones in the sound field characteristics and it is estimated that the circle array is the same to a line focus transducer in the artificial flaw detection sensitivity.

1．はじめに

熱交換器用薄肉管は高信頼性が要求され，その欠陥検査には渦流探傷あるいは超音波探傷検査が用いられているが，欠陥には多くの種類と形状があるので，品質保証の上から両者の併用が望ましい。しかし，超音波探傷検査においては，超音波探触子（以下，探触子と称する）を管円周方向に高速で回転させるもの[1]と，管円周方向に探傷子を多数個配置する方法とがあり，いずれも装置が高価格な上に，初期設定に時間を要する。これらに代る方式として，リニアアレイ探傷の理論[2,3,4]を用いたサークルアレイ探傷方式を検討し，その探触子を試作した。すなわち，振動子を環状に多数個配列し，本報では，その設計因子である駆動振動子数，振動子幅，振動子ピッチと超音波ビームの指向性等の関係を求めると共に，人工欠陥を外表面にもつ熱交換器用チタニウム溶接管についてその検出能を検討した。

2．サークルアレイ探傷検査

2.1　リニアアレイ探傷検査

リニアアレイ探傷検査は，電子走査形超音波探傷装置と超音波振動子（以下，振動子と称する）を直線状に多数個配列したアレイ形探触子を用い，超音波ビームを任意の方向に集束・偏向させて探傷を行うものである。

リニアアレイ探傷の原理を**Fig. 1**に示す。各振動子間の駆動タイミングを，一番端の振動子から順次遅延させて電子走査することにより，各振動子から放射された超音波の波面は，互いに干渉して超音波ビームが合成される。超音波ビームは遅延時間をリニアにすれば，振動子面に斜めに進行し，また，遅延時間を円弧にすると，超音波ビームはある一点に向って集束する。従って，超音波ビームは，各振動子間の遅延時間を変えることにより任意の進行方向をえらぶことができる。この超音波ビームが欠陥に当ると反射し，その反射波は球面状に広がって振動子へ戻ってくる。各振動子が受信した反射波に対して遅延時間を与えた後に加算すると，送信方向からの反射波のみ波面が強くなり，強い受波指向性が得られる。

2.2　サークルアレイ探傷検査

サークルアレイ探傷検査は，理論的にはリニアアレイ

---

* 日本非破壊検査協会　昭和60年度秋季大会（10月16～17日，於・仙台）にて一部発表，「管の超音波用サークル状リニアアレイ探触子の開発」を改題

** 技術研究所プロセス研究部

探傷検査と同じであり，後者の振動子配列が直線状であるのに対し，振動子を環状に配列したものである。従って，リニアアレイ探触子との形状の相違から生じる超音波ビーム路程差を遅延時間で補正しなければならない。

サークルアレイ探傷検査の概念を**Fig. 2**に示す。超音波ビームを管表面附近に集束・偏向させ，配列した環状振動子の中心位置を管が通過する際に探傷検査を行うわけであり，環状振動子と被探傷管の間には水を媒質として用いる。この方式は，電子走査により振動子の駆動を順に行って管の全周を高速で探傷するため，機械的な回転部分[1]がなく，また，装置が小型となり，かつ，初期設定が容易となる。

2.3　超音波ビームの指向性

幅wの線状振動子の指向性を $D_w(\theta)$ とすると，式(1)のように表わされる[5]。(**Fig. 3**参照)

$$D_w(\theta) = \sin\phi_w / \phi_w \qquad \cdots\cdots(1)$$

$$\text{ここに，} \phi_w = \frac{w\pi\sin\theta}{\lambda}$$

λ：媒質中の波長，(水の場合，$\lambda = 0.298\mathrm{mm}$)

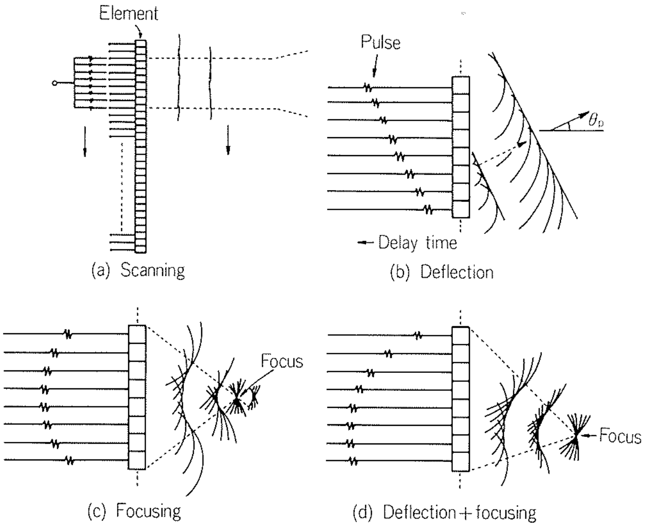
Element
Pulse
θ_D
Delay time
Focus
Focus

(a) Scanning　(b) Deflection　(c) Focusing　(d) Deflection＋focusing

Fig. 1　Phase steered ultrasonic linear array technology.

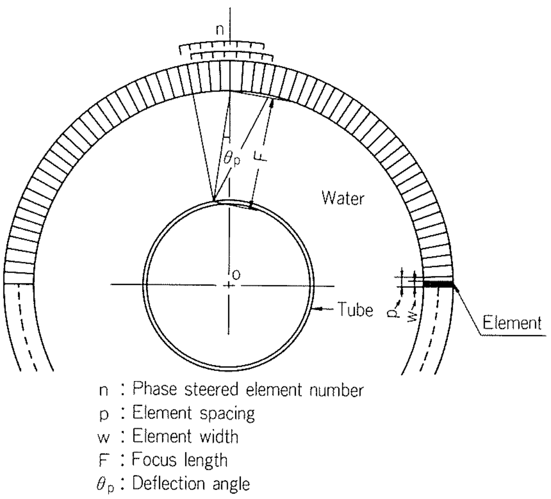
n
θ_p
F
Water
o
Tube
p
w
Element
n : Phase steered element number
p : Element spacing
w : Element width
F : Focus length
θ_p : Deflection angle

Fig. 2　Phase steered ultrasonic circle array.

また，n 個の点音源を直線状にピッチ p で配列したときの指向性 $D_p(\theta)$ は，n が偶数と奇数の場合とでは異なり，式(2)，(3)で示される[6]。

$$n = \text{偶数：}\quad D_p(\theta) = \Big[\sum_{i=1}^{n/2} A_i\Big]^{-1} \sum_{i=1}^{n/2} A_i \cos(2i-1)\phi_p \qquad \cdots\cdots(2)$$

$$\text{ここに，} \phi_p = \frac{p\cdot\pi\cdot\sin\theta}{\lambda}$$

A_i：i 番目の点音源の振幅

$$n = \text{奇数：}\quad D_p(\theta) = \Big[\sum_{i=0}^{(n-1)/2} A_i\Big]^{-1} \sum_{i=0}^{(n-1)/2} A_i \cos 2i\phi_p \qquad \cdots\cdots(3)$$

偏向した超音波ビームの合成指向性 $D_t(\theta)$ は，振動子各々の指向性と，各振動子の中心に点音源を配列したときの指向性との積であり，式(4)で表わされる。

$$D_t(\theta) = D_w(\theta)\cdot D_p(\theta) \qquad \cdots\cdots(4)$$

$D_t(\theta)$，$D_w(\theta)$，$D_p(\theta)$は，実際にはθにおける音圧を$\theta = 0$のときの音圧で除した値である。

(1)　駆動振動子数による影響

後述の試作したサークルアレイ探触子($w = 1.1\mathrm{mm}$，$p = 1.4\mathrm{mm}$，周波数$f = 5\,\mathrm{MHz}$)の$D_t(\theta)$を$n = 1 \sim 8$の場合について式(4)から求めた結果を**Fig. 4**に示す。**Fig. 4**において，$D_t(\theta)$が$0 \sim 1.0 \sim 0$の範囲を主極(main beam)，それ以外の凹凸を副極(side lobe)という。主極の$D_t(\theta)$

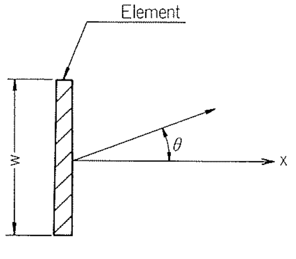
Element
w
θ
x

Fig. 3　Emission from a single array element.

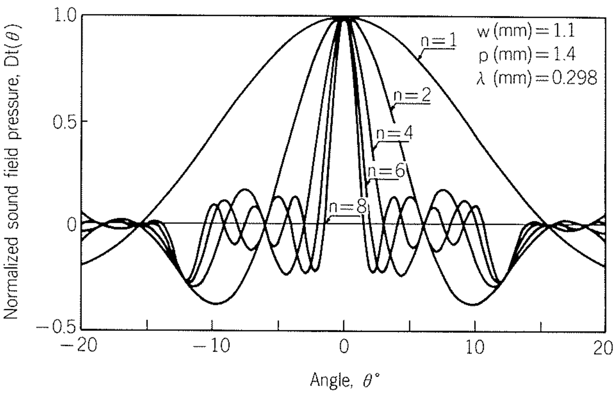

Fig. 4　Theoretical values of the sound field pressure distribution.

は，nが多くなると鋭くなり，画像表示した場合には虚像の原因となる副極の高さは小さい。副極の発生は，超音波ビームを集束する場合に有限の大きさの振動子に対して遅延時間を与えて行うので，遅延時間が連続とならず，位相加算された波面は完全な凹面とならないためである。また，振動子の形状は矩形板を用いるから，その形状比（振動子の厚さtと幅wの比，t/w）も副極発生の原因となる。

(2) 振動子ピッチによる影響

前項の探触子において，n＝8として0.2mm間隔でp＝1.2～2.0mmと変えた場合の$D_t(\theta)$を求めた結果を**Fig. 5**に示す。主極の$D_t(\theta)$はpが大きくなるにつれて鋭くなるが，副極の高さは変らないことがわかる。

(3) 振動子幅の影響

同様にn＝8として，0.2mm間隔でw＝0.4～1.2mmと変えた場合の$D_t(\theta)$を**Fig. 6**に示す。主極の$D_t(\theta)$は，この程度のwの範囲では差が殆んど認められず，副極の高さも変わらない。

2.4 グレーティングロブ発生角

探触子はn個の振動子より構成されている。従って，**Fig. 7**に示すように，主極方向以外に隣接振動子によって超音波の位相が整数波長ずれた方向にも合う波面を生じ，それをグレーティングロブ（grating lobe）という。

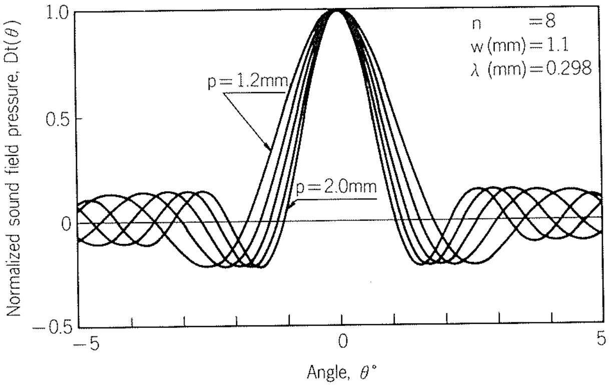

Fig. 5 Theoretical value of the sound field pressure distribution.

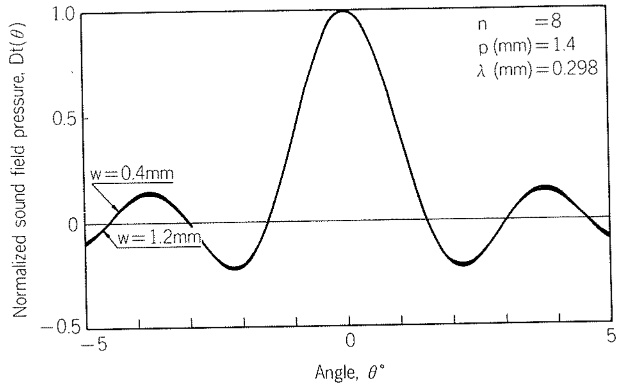

Fig. 6 Theoretical value of the sound field pressure distribution.

1波長ずれたグレーティングロブの伝搬方向θ_gを式(5)に示す[5)]。

$$\theta_g = \sin^{-1}\{(\sin\theta_p) \pm \lambda/p\} \quad \cdots\cdots(5)$$

ここに，θ_p：主極の偏向角

θ_gはn個の振動子の中心における法線からの傾きであり，法線に対してθ_pの反対側を負とする。媒質は水なのでλ＝0.298mmとなり，θ_gはθ_pとpの関数となる。θ_pを0～8°，0.2mm間隔でp＝1.2～2.0mmと変えた場合のθ_gを式(5)から求めて**Fig. 8**に示す。**Fig. 8**からわかるように，θ_pまたはpが大きくなるにつれてθ_gは小さくなる。

θ_gが小さくなると，グレーティングロブの裾野のビームが探傷する管の中心に向くため，管表面からの反射エコーが大きくなって，主極入射点近辺の探傷が難しくなるので望ましくない。

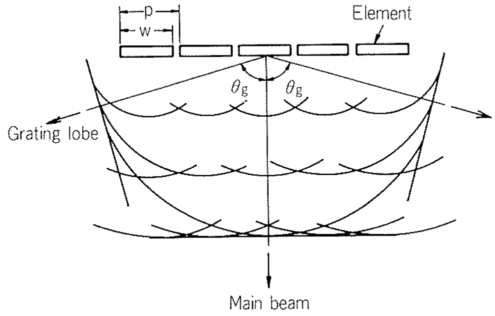

Fig. 7 Propagation of grating lobe.

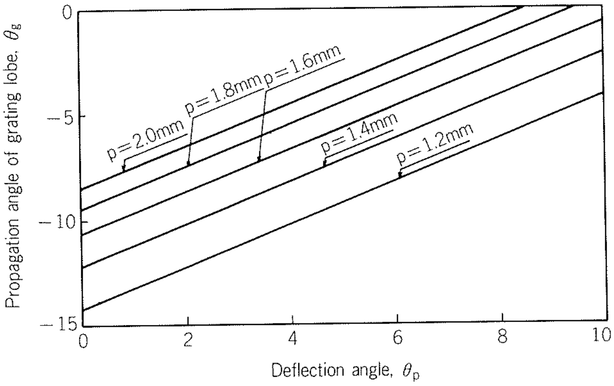

Fig. 8 Relation between deflection angle and propagation angle of grating lobe.

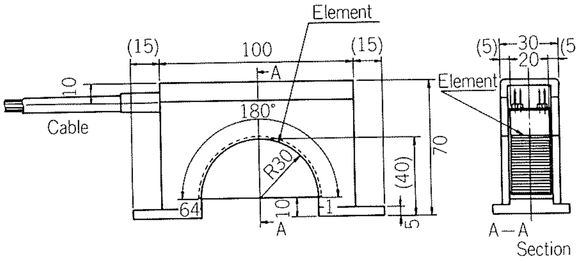

Fig. 9 Phase steered ultrasonic circle array.

3. サークルアレイ探傷実験

3.1 試作サークルアレイ探触子

試作したサークルアレイ探触子の形状は**Fig. 9**に，仕様を**Table 1**にそれぞれ示す。振動子の材質は，ジルコン酸チタン酸鉛である。n 個の振動子の音圧の測定には**Fig. 10**に示す音圧反射装置（反射体は直径0.8mm，長さ40mm の鋼針）を用い，媒質は水である。なお，使用した超音波探傷装置は，デジタル制御可能な(株)東芝製AU100型であり，パルサーチャンネル数は，64個である。

3.2 音圧分布測定結果

(1) 単一振動子の指向性

n＝1のときの$D_w(\theta)$の実測値を式(1)からの理論値と比較して**Fig. 11**に示す。両者はほぼ一致していることがわかる。

(2) 集束・偏向状況

n＝8，焦点距離F＝20mmとして，θ_pを変えた場合の焦点近傍での音圧分布測定結果を**Fig. 12**に示す。θ_pを大きくするにつれて主極の音圧が低下し，グレーティングロブの発生が顕著となる。主極の偏向は，設定と測定結果との間にずれがあるが，これは反射体の位置設定誤差が最大1 mm（$\theta_p=2.9°$に相当）あるためである。偏向による主極の音圧は **Fig. 13** からわかるように式(1)に，また，グレーティングロブの発生角は **Fig. 14** に示すように式(5)と，それぞれほぼ一致している。

Table 1　Specification of phase steered ultrasonic circle array.

Frequency,	f(MHz)	5
Element width,	w(mm)	1.1
Element spacing,	p(mm)	1.4
Element number,	N	64
Element length,	L(mm)	20
Radius of half circle,	R(mm)	30

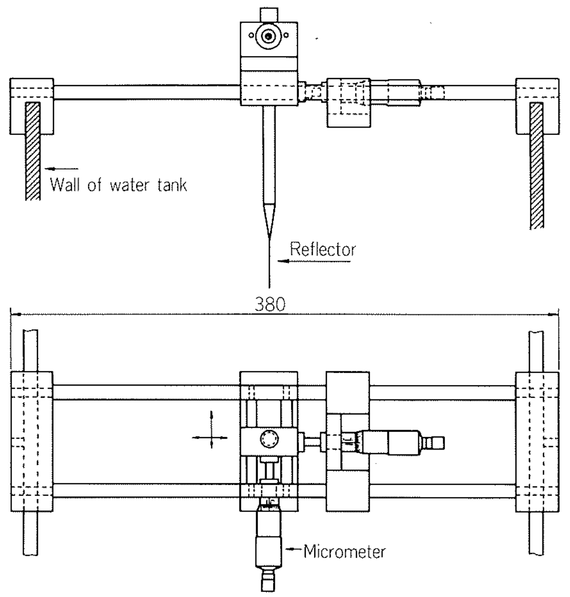

Fig. 10　Reflect calibrater.

(3) 主極の音圧と幅

振動子形状が円板の場合，中心軸上の音圧は測定位置Xが遠距離の場合には，式(6)で表わされる[7)]。

$$P=P_0\pi a^2/\lambda X \qquad \cdots\cdots(6)$$

ここに，a：円板の半径

P_0：振動子直前の平均音圧

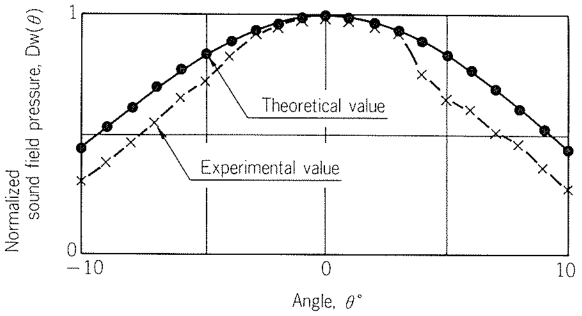

Fig. 11　The sound field pressure distribution of a single array element.

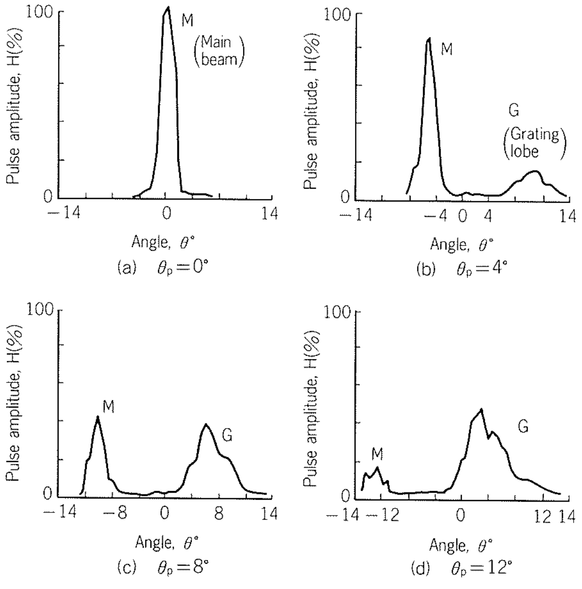

(a) $\theta_p=0°$　(b) $\theta_p=4°$　(c) $\theta_p=8°$　(d) $\theta_p=12°$

Fig. 12　Sound field pressure distribution by the circle array. (Focus length F : 20mm)

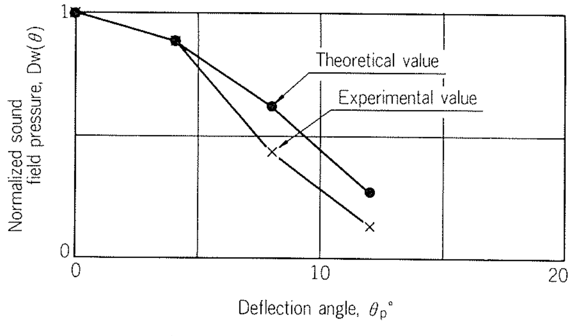

Fig. 13　Main beam intensity.

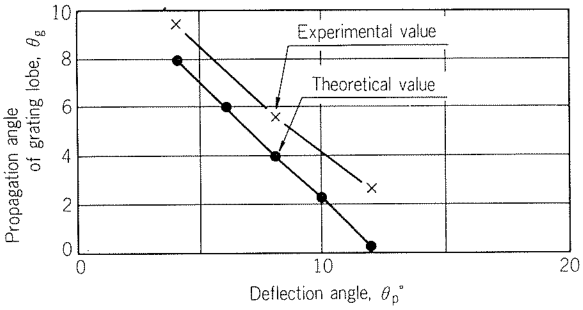

Fig. 14 Propagation angle of grating lobe.

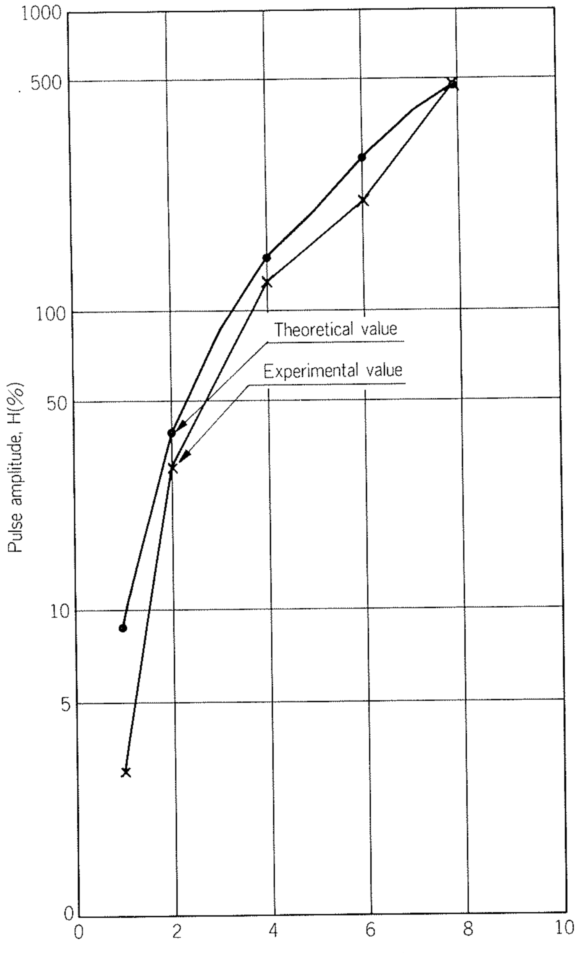

Fig. 15 Main beam intensity.

振動子形状が矩形板の場合も円板と同様，中心軸上の音圧は振動子の面積に比例すると考えられる。しかし，音圧をエコー高さで表示する場合には，音圧は振動子の電気音響変換損失により振動子の面積の２乗に比例する[8]。**Fig. 15**にnと主極の音圧，**Fig. 16**にnと主極の幅（ピーク感度より 6 dB downさせたときの幅）の関係をそれぞれ示す。いずれの場合も，実測値は測定値とよく一致していることがわかる。すなわち，n が多くなるに従って主極音圧は高くなり，主極の幅は小さくなって $D_t(\theta)$ が鋭くなる。

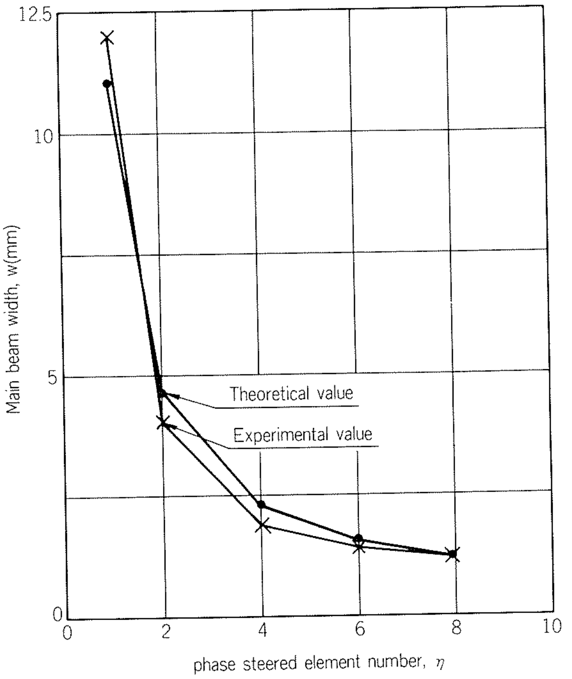

Fig. 16 Main beam width.

Table 2 Sensitibity by phase steered ultrasonic circle array and point focus transducer.

Tube (Diameter× Thickness, mm)	Artificial flaw dimension (Width×Length, mm)	S/N Ratio	
		Line focus transducer	Circle array
12.7 ×0.7	0.05×15	6.0	4.0
19.05×0.7	0.08×10	7.0	3.5

3.3 人工欠陥検出能

熱交換器用チタニウム溶接管の外表面に設けた人工欠陥に対するラインフォーカス形探触子と試作サークルアレイ探触子による検出能を，**Table 2** に示す。なお，供試管への超音波ビームの入射は，板波 A_0 モード発生入射角にて行った。試作サークルアレイ探触子の長さ L＝20mm，ラインフォーカス形探触子の焦点位置でのビーム長さ l= 6 mmを考慮すれば，サークルアレイ探触子とラインフォーカス形探触子の人工欠陥検出能は，同等と推定される。

4. まとめ

本報では，サークルアレイ探触子を設計するときに必要となる駆動振動子数，振動子幅，振動子ピッチと超音波ビームの指向性等の関係を理論式から求めた。また，サークルアレイ探触子を試作し，理論式との適合性並びに人工欠陥の検出能について検討した。得られた結果は以下のようである。

(1) 駆動振動子数が多くなるに従い，主極の指向性は鋭くなり，主極の強度も強くなる。

(2)　振動子ピッチが大きくなるにつれて，主極の指向性は鋭くなる。

(3)　振動子幅0.4～1.2mmの範囲では，主極の指向性は変わらない。

(4)　単一振動子の指向性により，主極の強度が決定される。

(5)　主極の強度は偏向を大きくするにつれて弱くなりグレーティングロブが顕著になる。

(6)　試作サークルアレイ探触子の人工欠陥検出能は，ラインフォーカス形探触子と同等である。

本方式による探傷検査は，従来方式と比べて装置の価格が安価となり，初期設定にそれほど時間を要しない利点をもつが，装置の実用化には探傷速度，振動子間の感度差等未解決の点があるので，更に今後の研究が必要である。

文　献

1)　鷲田理雄，金森照夫，野世渓精：本誌，**19**（1978），168.

2)　長井敏，内田邦治：**NDI資料**，春期大会講演概要（1981），114.

3)　岩崎全良：**NDI資料**，No.2915（1982），1.

4)　土屋武雄，玉木清英，小管英男：**NDI資料**，No.2979（1983），31.

5)　D. K. Lemon and G. J. Posakony：Mat. Eva., **38**（1980），34.

6)　小島正：**医用超音波機器ハンドブック**，コロナ社，（1980），57.

7)　日本非破壊検査協会編：**超音波探傷試験B**，（1979），15.

8)　前出7），16.

Reprinted from SUMITOMO LIGHT METAL TECHNICAL REPORTS (Title No. P-388)

論　文

HIP成形した Al-Si-Cu-Mg P/M合金の機械的性質*

渋江和久**　山内重徳**

Mechanical Properties of Hot Isostatic Pressed Al-Si-Cu-Mg P/M Alloys

by Kazuhisa Shibue and Shigenori Yamauchi

住友軽金属工業株式会社技術研究所

論　文

HIP成形した Al-Si-Cu-Mg P/M合金の機械的性質*

渋江和久**　山内重徳**

Mechanical Properties of Hot Isostatic Pressed Al-Si-Cu-Mg P/M Alloys

by Kazuhisa Shibue and Shigenori Yamauchi

It has been widely accepted that hot isostatic pressing (HIP) cannot provide excellent mechanical properties for the consolidated aluminium powder alloy because it is not effective in breaking up the surface oxide film on the aluminium powder particles.

In this study, the effects of following factors on the mechanical properties of Al-20%Si-2%Cu-1%Mg powder alloy by HIP was investigated: (1) atomization gas, (2) degassing condition before HIP, (3) temperature and (4) period of HIP. And mechanical properties of HIPed powder alloy were compared with those of extruded powder alloy.

Results obtained were as follows:

(1) Mechanical properties of HIPed powder alloys were comparable to those of extruded one.
(2) Optimal temperature of HIP was from 450 to 525 °C. At 550 °C, Si particles were coarsened, and at 400 °C, the mechanical properties were inferior to that of extruded alloy.
(3) Period of HIP had no effect on the mechanical properties of HIPed alloy. 10 min at 500 °C was enough to get excellent properties.
(4) Neither atomization gas nor degassing condition had effect on the mechanical properties of HIPed alloy. Air atomized powder was available for HIP as well as argon gas atomized one. As degassing condition, 10^{-3} Torr at 495 °C was useful.

In conclusion, HIP is considered to be available to consolidate Al-20%Si-2%Cu-1%Mg powder alloy.

1. 緒　　言

急冷凝固粉末を成形して得た過共晶 Al－Si 系合金はI/M法によるものと比較して機械的性質に優れていることが報告されている[1~3]。これらは，いずれも急冷凝固粉末を熱間押出により成形したものである。

一方，熱間静水圧圧縮(Hot Isostatic Pressing, 以下, HIP と略す）は，Near Net Shape ができる成形法として注目され，セラミックスや超合金の成形法として利用されている。しかし，アルミニウム合金粉末の場合，HIP成形では粉末表面の酸化膜を破壊することができないため，十分な機械的性質を得ることができず，HIP処理後に，押出，鍛造，または圧延などの熱間加工を施す必要があるとされている[4,5]。しかしながら，このことをAl－Si 系合金粉末について調べた報文はあまり見受けられない。

本報では，耐摩耗性に優れた Al-Si-Cu-Mg 系合金粉末の HIP による Near Net Shape の可能性を調査するため，Al-20%Si-2%Cu-1%Mg 合金のガスアトマイズ粉末を HIP 成形し，その機械的性質を測定した。すなわち，HIP 処理の温度及び時間，粉末表面の酸化膜，脱気の影響を検討し，HIP成形材と押出成形材の機械的性質を比較した。

2. 実　験　方　法

Table 1 に供試粉末合金の化学成分を示す。本合金粉

---

* 軽金属学会第68回春期大会（昭和60年5月，於：富山）で一部（熱間静水圧圧縮した Al-Si 系粉末合金の機械的性質）を発表

** 技術研究所金属材料研究部

Table 1　Chemical composition of experimental alloys.

Alloy	Atomization gas	Chemical composition (wt. %)			
		Si	Cu	Mg	Al
A	Air	21.2	1.9	0.97	Bal.
B	Argon	20.3	1.8	0.95	Bal.

末は母合金を溶解後，エアー並びにアルゴンガスアトマイズ法により作成した。

粉末圧縮体は，これらの粉末を粒径 297μm 以下に振動式ふるい器で分級し，冷間で一軸圧縮（外径62.7mm，高さ127mm）して得たものであり，圧縮体の密度は理論密度の80%となった。次に，脱気を行うために，圧縮体を外径68mm × 内径64mm のアルミニウム合金（6063）管に装入してその両端を封じ，一端に真空排気用アルミニウム管（1050）を接続した。脱気は昇温とともに開始して 495°C に到達後 1hr 保持し，ただちにアルミニウム管を圧縮してアルミニウム合金管内の真空度を保持した。このようにして得たビレットを HIP 処理または押出に供した。

HIP 処理は㈱神戸製鋼所製の小型 HIP 装置により行った。まず，HIP 処理温度の検討をエアーアトマイズ粉末により実施した。HIP 処理温度は，400，450，500，525 及び 550°C とし，処理時間は 1hr で，処理圧力は，1,000kgf/cm^2 とした。同様に，HIP 処理時間の検討は温度を 500°C にえらび，10，20，60 及び 120min と変えて行った。

さらに，粉末表面の酸化膜の影響を調べるため，エアー及びアルゴンガスアトマイズ粉末を用い，脱気の真空度を 10^{-3} または 10^{-5} Torr としたものについて HIP 処理を行った。

最後に，HIP 成形材と押出成形材の機械的性質の比較をエアーアトマイズ粉末を用いて行った。このとき，HIP 処理条件として，温度は 500°C，圧力は 1,000kgf/cm^2，処理時間は 1 hr とした。また，押出は 400°C において行い，押出比を15（押出寸法 ϕ18mm）とした。

熱処理はT6 処理(495°C× 1 hr水冷後175°C× 6 hr　空冷）とした。

以上のようにして作成した成形材について，密度，金属組織，ビッカース硬さ，引張性質，シャルピー衝撃値及び疲労強度を調査した。なお，引張試験は常温のほかに 250°C（100hr 保持）及び 450°C（ 1 hr 保持，押出成形材のみ）において行った。

3．実　験　結　果

3.1　HIP 処理温度の影響

3.1.1　密度

Fig. 1 に HIP 処理温度と成形体の密度の関係を示す。

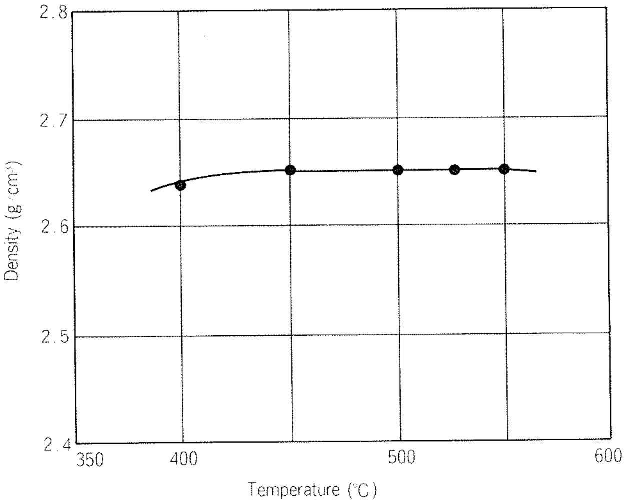

Fig. 1　Density vs. temperature of HIP of A alloy (F).

400°C の場合，密度は 2.64g/cm^3 であり，それ以上の温度の場合よりもやや低いが，450°C以上では，密度は2.65 g/cm^3 とほぼ一定の値をもつ。

3.1.2　金属組織

Fig. 2 に HIP 処理温度と金属組織の関係を示す。いずれの場合も，Si 粒子の分布はほぼ均一であった。500 °C 以下では，Si粒子の大きさはほぼ一定であり，それ以上の温度では，Si 粒子は粗大化する傾向を示した。

3.1.3　硬さ

Fig. 3 に HIP 処理温度とビッカース硬さの関係を示す。F 材（HIP 処理のまま）は 450°C 以上の処理温度では一定のビッカース硬さをもつが，400°C では幾分高い。T 6 材では，処理温度の上昇につれて硬さが向上するが，450 °C を越えるとほぼ一定値となった。

3.1.4　引張性質

Fig. 4 に HIP 処理温度と引張強さの関係を示す。F材では，400°C のものの引張強さが 450°C 以上のものよりもやや低く，この傾向は，T 6 材においては顕著であった。

また，伸びは，処理温度 450°C 以上ではF材が 3 ～ 7 %，T 6 材では 1 ～ 3 %であり，400°C の場合は F 材，T 6 材のいずれも 0 %であった。

Fig. 5 に引張試験片破断面の SFM 写真を示す。処理温度 400 °C のものでは主に PPB（Powder Particle Boundary）で破断しているが，500°Cの場合にはPPB での破断は観察されず，破面はディンプル状であった。このことから，400°C の HIP 処理の場合，粉末間の接合が不十分なために引張強さ及び伸びが低かったものと推測される。

3.2　HIP 処理時間の影響

3.2.1　金属組織

10～120min の範囲において，処理時間による金属組織の差は見られなかった。

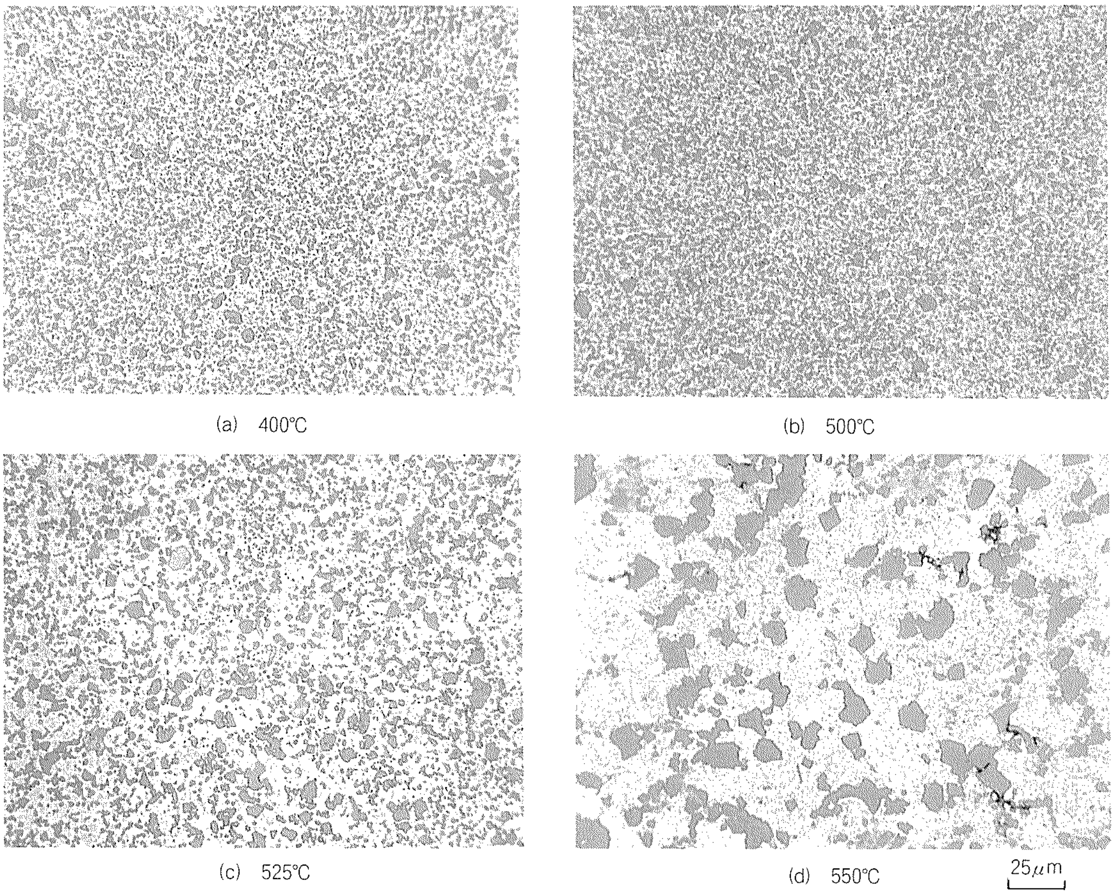

(a) 400℃ (b) 500℃

(c) 525℃ (d) 550℃

Fig. 2 Microstructures of A alloy consolidated by HIP at 400～550℃ (T6).

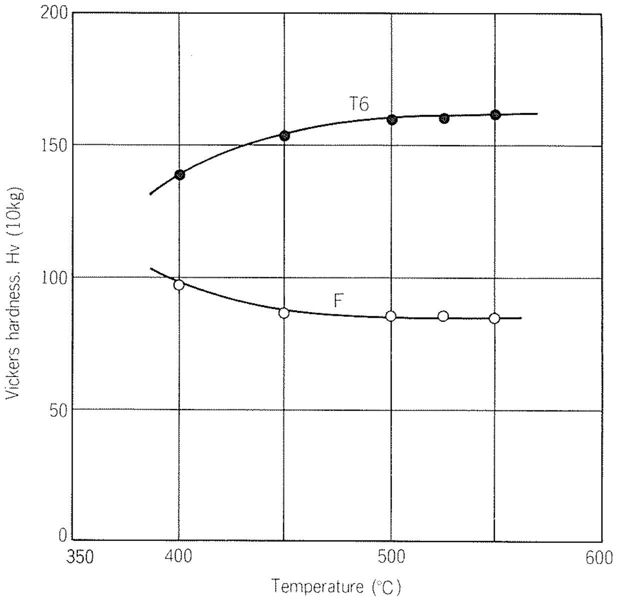

Fig. 3 Vickers hardness vs. temperature of HIP of A alloy.

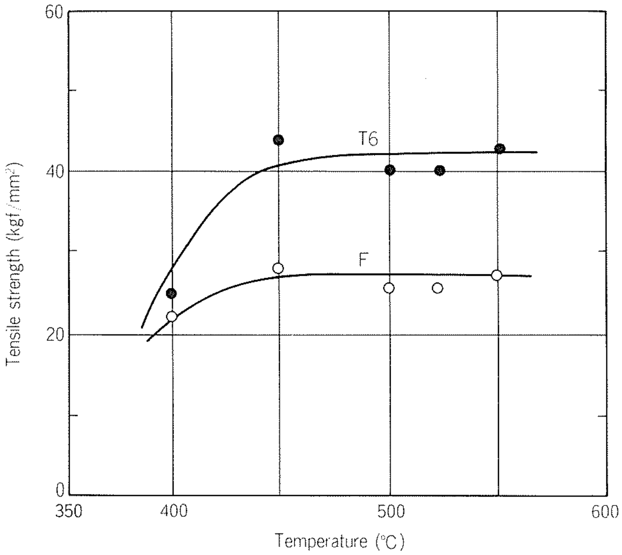

Fig. 4 Tensile strength vs. temperature of HIP of A alloy.

3.2.2 引張性質

Fig. 6 はF材及びT6材についてHIP処理時間と引張強さの関係を示す。10～120min の範囲において，処理時間は引張強さに影響を及ぼさなかった。なお，伸びについても同様であった。

3.3 アトマイズガス及び脱気条件の影響

3.3.1 金属組織

F材およびT6材ともに，アトマイズガスの種類及び脱気条件による金属組織の差は見られなかった。

3.3.2 機械的性質

Table 2 にF材及びT6材の機械的性質を示す。引張

Table 2 Effect of atomization gas and degassing condition on the mechanical properties of Al－Si－Cu－Mg powder alloys consolidated by HIP.

No.		Atomization gas	Degassing condition	Heat treatment	Tensile strength (kgf/mm^2)		Vickers hardness (10kg)
					Room temp.	250℃$^{(1)}$	
1	A alloy	air	495℃, 10^{-3}Torr	F	25.1	10.8	90
2				T6	40.5	11.8	156
3	B alloy	argon		F	24.5	9.9	87
4				T6	39.9	11.1	150
5	A alloy	air	495℃, 10^{-5}Torr	F	24.2	9.9	88
6				T6	39.9	11.4	153
7	B alloy	argon		F	24.3	10.0	86
8				T6	40.2	11.3	151

(1) Keeped for 100hr

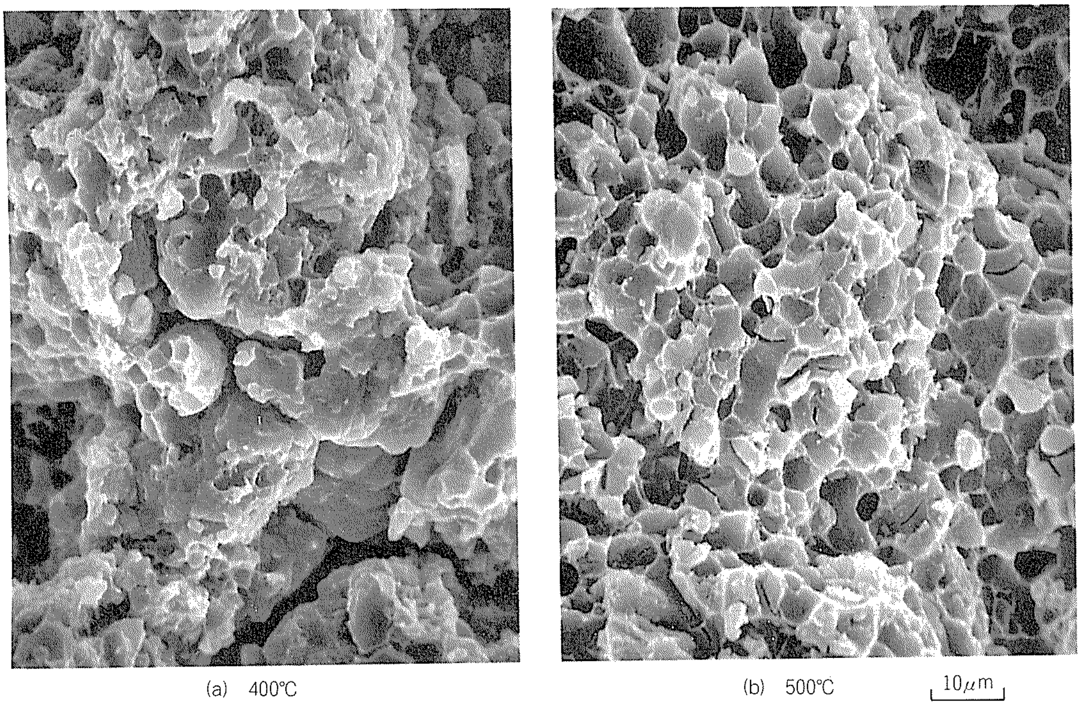
(a) 400℃　　(b) 500℃

Fig. 5 SEM fractographs showing fracture surface of tensile test specimens of A alloy consolidated by HIP at 400℃ and 500℃ (F).

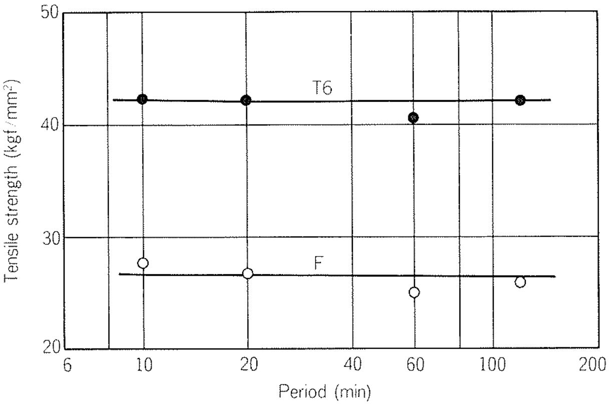

Fig. 6 Tensile strength vs. peviod of HIP at 500℃ of A alloy.

強さ及びビッカース硬さはF材，T6材ともそれぞれアトマイズガスの種類（エアーとアルゴン）及び脱気の真空度（10^{-3}と10^{-5} Torr）に関係なくほぼ同等であった。

3.4 HIP成形材と押出成形材の比較

3.4.1 金属組織

Fig. 7にHIP成形材と押出成形材の金属組織を示す。Si粒子の大きさは両者とも1～10μm程度であった。押出成形材の場合，いずれの場合も，金属組織中に空洞は観察されなかった。

Fig. 8に引張試験片破断部の断面金属組織を示す。いずれにおいても，PPBではく離したこん跡は見られず，粒子間の接合が十分であったものと推測される。

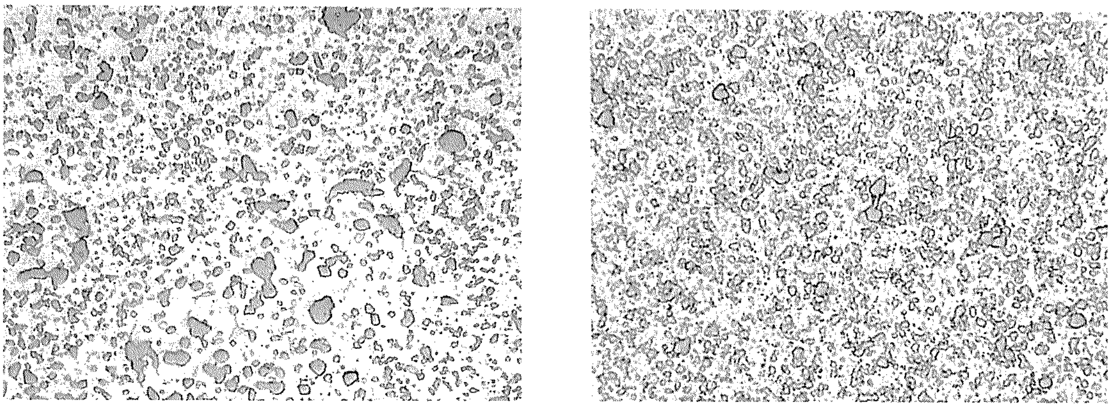

(a) HIP ed at 500°C (A alloy) (b) Extruded at 400°C (A alloy)

Fig. 7 Microstructures of alloys (T6).

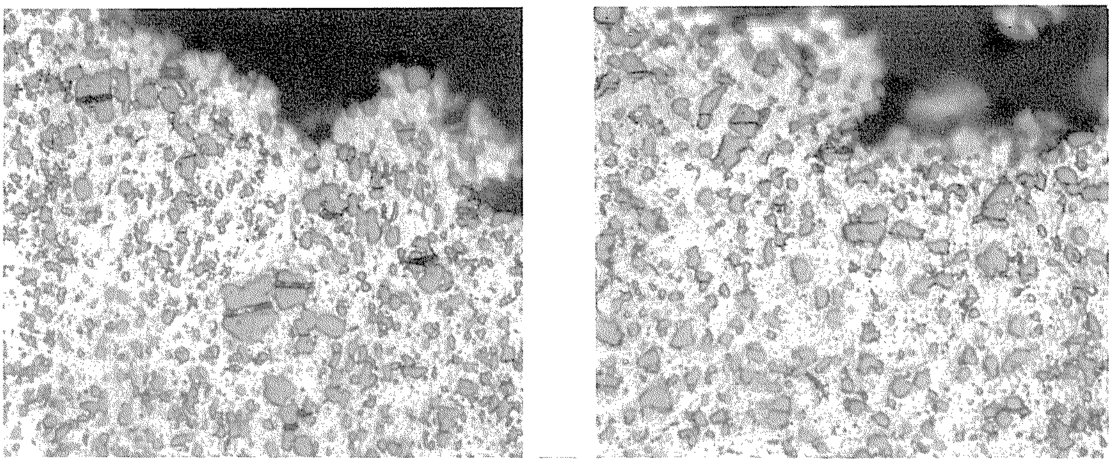

(a) HIP ed at 500°C (A alloy) (d) Extruded at 400°C (A alloy)

Fig. 8 Cross sectional microstructures of fractured surface of tensile test specimens (T6).

Table 3 Mechanical properties of powder alloys consolidated by HIP or extrusion process. (A alloy)

No.	Consolidation	Heat treatment	Tensile strength (kgf/mm^2)		Vickers hardness (10kg)	Charpy impact test (kgf/cm^2)		Fatigue strength$^{(2)}$ 10^7 (kgf/mm^2)
			Room temp.	250℃$^{(1)}$		U-notch	V-notch	
1	HIP	F	25.1	10.8	90	0.6	0.5	—
2	Extrusion	F	25.9	12.0	90	0.6	0.5	—
3	HIP	T6	40.5	11.8	156	0.3	0.2	20.0
4	Extrusion	T6	40.9	11.5	158	0.3	0.2	20.5

(1) Keeped for 100hr (2) Rotating-beam fatigue test, 1,750 rpm.

3.4.2 機械的性質

Table 3 に HIP 成形材と押出成形材の機械的性質を示す。F 材及び T 6 材いずれの場合も，HIP 成形材の引張強さ，ビッカース硬さ，シャルピー衝撃値および疲労強度は，押出成形材のものと同程度であった。

なお，押出成形材の 450°C における高温引張強さ及び耐力はそれぞれ 1.3kgf/mm^2，0.6kgf/mm^2 であった。

4. 考　　察

一般に，アルミニウム合金粉末の表面には酸化膜が存在するために，HIP 成形では十分な機械的性質が得られないとされている[4,5]。さらに，HIP 成形のみでなく，押出比や鍛造比が小さい場合には酸化膜が十分破壊されないために機械的性質が劣るとの報告が7091 (Al-Zn-Mg-Cu-Co合金)，Al-8%Fe-4%Ce 及び Al-6%Fe-6%Ni合

金についてなされている[6]。しかし，本実験においてはHIP成形によっても押出成形と同等の機械的性質が得られた。本実験ではAl-Si-Cu-Mg合金を用いており，この違いについては以下のように推測することができる。

一般に，HIP成形における緻密化は，塑性変形，クリープあるいは拡散のいずれかによってなされる[7]。このうち，塑性変形による緻密化が生じ，密度が理論密度のどの程度になるかは(1)式より推定される[7]。

$$D_{yield}=[(1-D_0)P/1.3\sigma_y+D_0^3]^{1/3} \quad \cdots\cdots\cdots\cdots(1)$$

ここで　D_{yield}：塑性変形による緻密化が生じたときの圧縮体の密度
D_0：圧縮体の初期密度
P：外部圧力（HIP圧力）
σ_y：HIP温度での粉末合金の降伏応力

本実験においては，$D_0=0.8$，$P=10\mathrm{kgf/mm^2}$であり，また，450°Cにおける本合金の耐力は$0.6\mathrm{kgf/mm^2}$なので，この値をσ_yとして，(1)式からD_{yield}を求めると，$D_{yield}>1$となる。これは，HIP処理温度及び圧力に到達する前に緻密化が塑性変形により進行し，理論密度にほぼ達すると考えられる。従ってこの塑性変形により，粉末表面の酸化膜がある程度破壊され，その後の接合に寄与するものと推測される。

次に，本実験における最適なHIP処理温度は450～525°Cであり，Al-Si系粉末合金の通常の熱間加工温度(400°C前後[1,3])よりかなり高い。このため，粉末間の拡散が活発に生じ，粉末同士の接合が促進されているものと考えられる。400°CにおけるHIP処理では緻密化は生じたものの，接合は不十分であったことからも，高温におけるHIP処理が粉末の接合に大きく寄与したことが推測される。

さらに，本実験で用いた合金の添加元素は，いずれもAl中での拡散係数がAlの自己拡散係数よりも大きい[8]。このように拡散係数の大きい元素が多量に含まれていれば，HIP処理中において，緻密化が完了した後，粉末同士の拡散が活発に生じ，その結果，接合を促進したことが考えられる。

以上の三点が粉末同士の接合を促進し，本合金系においてはHIP成形によっても押出成形と同等の機械的性質が得られる原因をなしたものと考えられる。

粉末の種類（エアーアトマイズとアルゴンガスアトマイズ）及び脱気時の真空度（10^{-3}Torrと10^{-5}Torr）は，HIP成形材の機械的性質に影響を及ぼさなかった。エアーアトマイズ粉末の酸化膜は不活性ガスアトマイズ粉末のものよりもかなり厚い[9]にも拘らず，この影響が現われなかったのは，上述の考察をある程度裏付けるものであろう。ただし，詳細については，さらに検討を加えることが必要である。

本実験の結果から，本合金のHIP処理の最適温度は450～525°Cであるとみなされる。400°Cでは接合不十分となるので避ける必要がある。また，550°CにおいてはSi粒子が著しく粗大化し，急冷凝固粉末の特性を失うことになるので避けるべきである。HIP処理時間は500°Cにおいては10～120minのいずれでもよい。

5. 結　　語

Al-Si-Cu-Mg合金粉末のHIP成形を行い，次の結果を得た。

(1)　最適なHIP処理温度は450～525°Cであった。550°C以上ではSi粒子が著しく粗大化し，また400°Cでは，粉末同士の接合が不十分であった。

(2)　500°CにおいてHIP処理時間（10～120min）は成形材の機械的性質に影響を及ぼさなかった。

(3)　エアーアトマイズ粉末とアルゴンガスアトマイズ粉末のいずれの場合も，HIP成形材の機械的性質はほぼ同等であった。また，脱気時の真空度の相互の影響はなかった。

(4)　HIP成形材の機械的性質は押出成形材と同等であった。

なお，HIP成形に関して，ご指導を賜わった通商産業省工業技術院名古屋工業試験所機械部超高圧応用課　町田充秀氏に深甚な謝意を表する。

参 考 文 献

1）佐野秀男，渋江和久，山内重德，犬丸　晋：本誌，**26** (1985)，215.
2）C. F. Dixton and H. M. Skelly：Int. J. Powder. Met.，**1** (1965)，23.
3）山内　勇，大中逸雄，川元　暁，福迫達一：日本金属学会誌，**49** (1985)，231.
4）F. H. Froes and J. R. Pickens：J. Metals, **36** (1984)，14.
5）T. E. Tietz and I. G. Palmer：*Advances in Powder Technology* (Edited by G. Y. Chin), ASM (1981)，189.
6）Y. W. Kim, W. M. Griffith, and F. H. Froes：J. Metals, **37** (1985)，27.
7）A. S. Helle, K. E. Easterling, and M. F. Ash by：Acta metall., **33** (1985)，2163.
8）平野賢一：軽金属，**31** (1981)，206.
9）G. Staniek：Aluminium, **60** (1984)，768.

Reprinted from SUMITOMO LIGHT METAL TECHNICAL REPORTS (Title No. P-389)

論　　文

Joining of Bi-metal Tube of Aluminium Alloy and Titanium to Titanium Tube Plate by Welding Process.

by Keizo Nanba* and Yoshihiko Sugiyama**

住友軽金属工業株式会社技術研究所

Joining of Bi-metal Tube of Aluminium Alloy and Titanium to Titanium Tube Plate by Welding Process.

by Keizo Nanba* and Yoshihiko Sugiyama**

The bi-metal (duplex) tube composed of aluminium alloy and titanium will be applied to heat-exchangers such as condenser of power plants and apparatus for OTEC (Ocean Thermal Energy Conversion) system in order to make a good use of each characteristic of the dissimilar materials. However, the joining process of such a bi-metal tube to titanium tube plate has still been left insufficient in points of corrosion-resistance, leak-tightness and strength of the joint.

The objective of the present study is to produce the high quality of joint by using tubular transition joint (TJ) of aluminium alloy and titanium made with friction welding process.

Firstly, the study was carried out on producing the TJ by friction welding process and secondly, on joining the TJ to aluminium alloy tube and titanium tube plate by inert gas arc welding.

The results obtained are as follows.

(1) Sound welds between 6063 aluminium alloy and titanium tubes with 26.9mm diameter and 2.7mm thickness were obtained by friction welding process. The welds had satisfactory mechanical properties and the formation of diffusion or alloying layer was not observed at the interface.

(2) Reliable joints were made with TIG welding process between 6063 aluminium alloy tube and titanium tube plate through the TJ produced from the friction weld mentioned above. The strength of the joint had a similar value to that of 6063−0 aluminium alloy and the interface at friction weld of the joint seemed not to be affected by the arc weld thermal cycle used in this study.

Therefore, it is expected that the tubular TJ of aluminium alloy and titanium made with friction welding is put to practical use.

1. Introduction

In order to apply each characteristic of dissimilar materials effectively, many attempts to join different ones have been studied and carried out. The typical example is found in the application of bi-metal (duplex) tube composed of aluminium alloy and titanium to obtain high thermal conductivity and corrosion-resistance, respectively, to heat exchangers such as condenser of power plant and apparatus for OTEC (Ocean Thermal Energy Conversion) system.

Both flaring of tube and inert gas arc welding processes are considered to join such a bi-metal tube to titanium tube plate in constructing the condensers, but these processes do not always guarantee corrosion-resistance, leak-tightness and strength of the joint.

The objective of the present study is to produce the high quality of joint by using tubular transition joint (TJ) of aluminium alloy and titanium made with a friction welding process.

Firstly, the study was carried out on producing the TJ of aluminium alloy and titanium tubes by a friction welding, and, secondly, on joining the TJ to aluminium alloy tube and titanium tube plate by inert gas arc welding.

2. Friction welding of aluminium alloy and titanium tubes

2.1 Experimental procedures

There are few reports on the friction welding of aluminium and titanium, especially, aluminium alloy and titanium tubes. Therefore, as a preliminary test the study was carried out to get the proper conditions for friction welding of pure aluminium and titanium bars, and then those of aluminium alloy and titanium bars. By referring to these results, suitable conditions for aluminium alloy and titanium tubes were investigated.

---

* Technical Research Laboratories, Applied Technogy Dept.

** Technical Research Laboratories, Planning & Managing Dept.

The materials used in these experiments are shown in **Table 1**, where wall thickness of the tubes was selected above one-tenth of the diameter because of friction weldability of tube to tube combination.

The faying surface was finished smoothly and then degreased by acetone.

The friction welder used for this study are shown in **Table 2**.

The welding sequence are schematically represented in **Fig. 1**. The friction welds were made by holding a non-rotating workpiece of aluminium in contact with a rotating workpiece of titanium.

Friction welding process parameters investigated are as follows : total upset length of workpieces U(mm), friction pressure P_1(kgf/cm^2) and time during friction phase T_1(sec), upsetting pressure P_2(kgf/cm^2) and time during upsetting phase T_2(sec), and time to stop rotation of a workpiece NL(sec). These parameters are, also, shown in **Fig. 1**.

Specimens were welded, and then the welds were examined by bending, tensile and flattening tests, metallography and EPMA analysis.

Table 1 Test materials and their tensile properties.

Meterials		Tensile properties		
		Yield strength (kgf/mm^2)	Tensile strength (kgf/mm^2)	Elongation (%)
Bar[1]	1050−H112	6.5	11	33
	6061−H112	7.5	16.4∼16.5	29
	TB49−O	44	56	30
Tube[2]	6063−T83	22.3∼22.7	24.8∼25.2	18∼21
	TTP49−O	45.7	61.4	36

[1] Diameter : 28mm [2] Diameter : 26.9mm Thickness : 2.7mm

Table 2 Friction welder.

Type		FW30U
Maximum load (kgf)	at friction phase	4,000
	at upsetting phase	10,000
Capacity(for steel bar) (mm)		10∼30
Rotational speed (rpm)		2,400

2.2 Experimental results and discussion

(1) Friction welding of bars

Friction welding conditions for pure aluminium and titanium bars investigated are shown in **Table 3**. Welds obtained under No.1 condition showed good quality, though amounts of weld upset formed remarkably on the aluminium side. Therefore, in order to decrease the amount (which are shown in **Table 3** as U) mainly, experiments were carried out under Nos.2 to 4 conditions. Typical appearances, bending tested specimens and results of tensile test of the welds are shown in **Figs. 2** to **3** and **Table 4**, respectively. Good quality of welds were obtained similarly under Nos.2 to 4 conditions.

Friction welding conditions for 6061 aluminium alloy and titanium bars were investigated under No.61 condition in the range obtained in **Table 3**,

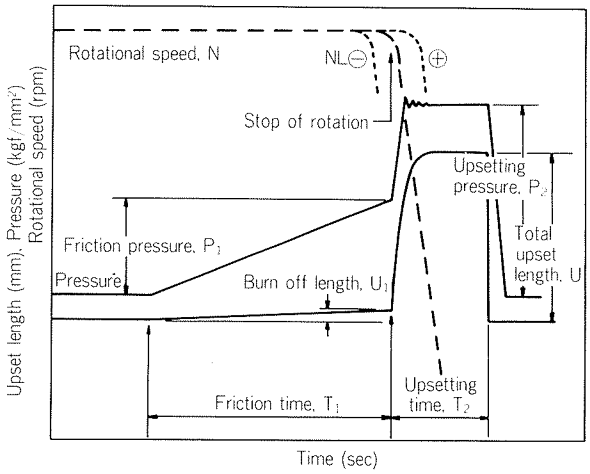

Fig. 1 Schematic representation of variation of the process parameters during friction welding.

Table 3 Friction welding conditions and quality of welds.

Materials (Bar)	No.	Welding conditions							Quality of welds
		U (mm)	Friction phase			Upsetting phase		NL (sec)	
			P_1 (kgf/cm^2)	T_1 (sec)	U_1 (mm)	P_2 (kgf/cm^2)	T_2 (sec)		
1050+Ti	1	17.8	28	10	2	60.5	4	0.3	No crack
	2	15.2	20	10	2	40	4	0.3	No crack
	3	14.8	20	10	1	40	4	0.3	No crack
	4	11.0	20	10	1	40	4	0	No crack
	Ranges for bar	10∼15	20	10	1∼2	40	4	0∼0.3	−

and under No.62 condition, where NL was changed into -0.3 sec in order to decrease U, as shown in **Table 5**. No crack occurred at welds under No.61 condition in any tests, but micro-cracks were observed at the interface of welds under No.62 condition in tensile test though the strength was not lower than that under No.61 condition, as shown in **Table 6**. Therefore, the suitable condition for those materials is No.61 as shown in **Table 5**.

(2) Friction welding of tubes

Friction welding conditions for 6063 aluminium alloy and titanium tubes were investigated by referring to results mentioned above. The results are shown in **Table 7**. Under No.11 condition P_2 was so high that 6063 aluminium alloy tube buckled. Therefore, P_2 was decreased to 33 or 20kgf/cm^2 so that the buckling might not occur. The results are shown in **Table 7** as Nos.12 and 13.

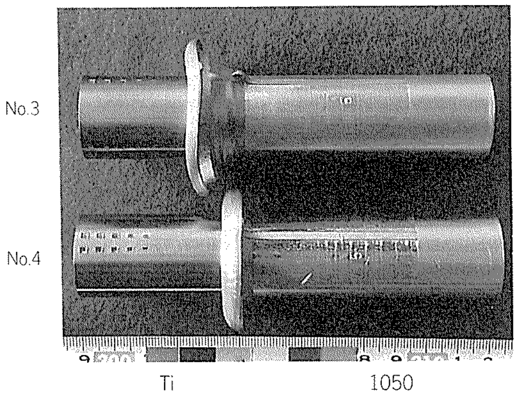

Fig. 2 Appearance of friction welds.

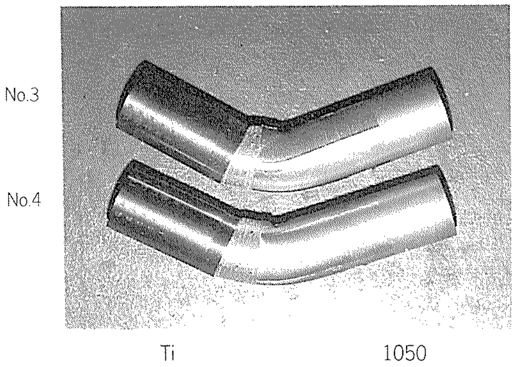

Fig. 3 Appearance of bending tested specimens.

Table 4 Results of tensile test of friction welds.

No.	Tensile strength(kgf/mm^2)	Position of fracture
2	8.0	1050 base metal
4	8.2	〃

No crack occurred at joints under both Nos.12 and 13 conditions in tensile and flattening tests as shown in **Table 8** and **Fig. 4**, respectively. Under No.12 condition the tensile strength was approximately 3kgf/mm^2 higher than that under No.13 condition, but the greater amount of weld upset was observed due to higher P_2, as shown in **Fig. 5**.

The micro-structure at friction weld interfaces and the results of EPMA analysis are shown in **Figs. 6** and **7**, respectively. These are the specimens friction welded under No.12 condition, since similar results were obtained under No.13 condition. Under both conditions, any weld defects such as lack of fusion and cracks are not observed at the interface. In additions, diffusion and alloying layers are not microscopically observed over the interfaces in all specimens. The interface between 6063 aluminium alloy and titanium is clear. The effect of P_2 was not observed at the metallographic examinations.

Hardness distributions of friction welds are shown in **Fig. 8**. In both conditions, the hardness is about 86(Hv) at the 6063 base metal side and it lowered near the interface because of frictional heat. Such a hardness distribution suggests that the weld is hardly work-hardened at friction and upset phases, and that alloying layer between aluminium and titanium is not observed, though it might be squeezed out from the weld at upset phase, even if it were formed at the interface. On the titanium base metal side, the hardness is about 190(Hv) and it does not

Table 6 Results of tensile test of friction welds.

No.	Tensile strength(kgf/mm^2)	Position of fracture
61	13.9	6061 base metal
62	13.9	6061 base metal and weld

Table 5 Friction welding conditions and quality of welds.

Materials (Bar)	No.	Welding conditions							Quality of welds
		U (mm)	Friction phase			Upsetting phase		NL (sec)	
			P_1 (kgf/cm^2)	T_1 (sec)	U_1 (mm)	P_2 (kgf/cm^2)	T_2 (sec)		
6061+Ti	61	10.1～10.3	20	10	1	40	4	0.3	No crack
	62	4.5～7.2	20	10	1	40	4	-0.3	Micro−cracks
	Ranges for bar	10.1～10.3	20	10	1	40	4	0.3	−

Table 7 Friction welding conditions and quality of welds.

Materials (tube)	No.	Welding conditions							Quality of welds
		U (mm)	Friction phase			Upsetting phase		NL (sec)	
			P_1 (kgf/cm^2)	T_1 (sec)	U_1 (mm)	P_2 (kgf/cm^2)	T_2 (sec)		
6063+Ti	11	23.5	20	10	1	39	3	0	Buckling
	12	12.6	20	10	0.5	33	3	0	No buckling, No crack
	13	6.7～7.6	20	10	0.5	20	3	0	
	Ranges for tube	6～13	20	10	0.5	20～33	3	0	–

Table 8 Results of tensile test of friction welds.

No.	Tensile strength(kgf/mm^2)	Position of fracture
12	21.4	6063 base metal
13	17.8	〃

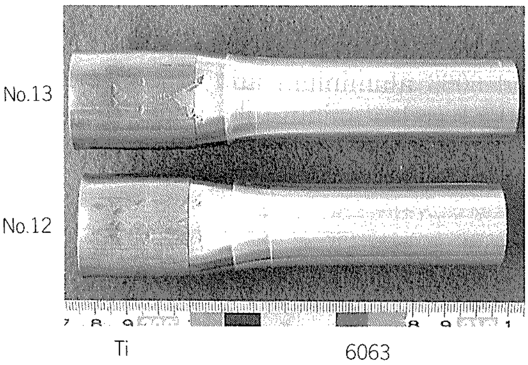
No.13
No.12
Ti
6063

Fig. 4 Appearance of flattening tested specimens.

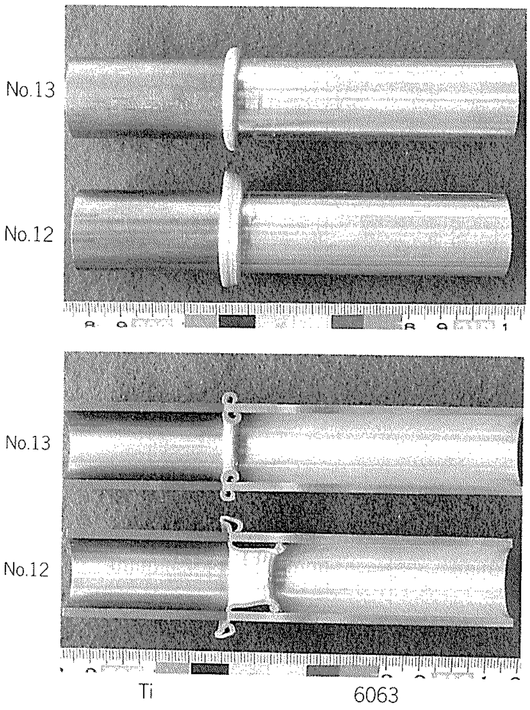
No.13
No.12
No.13
No.12
Ti
6063

Fig. 5 Appearance of friction welds and their cross-sectional views.

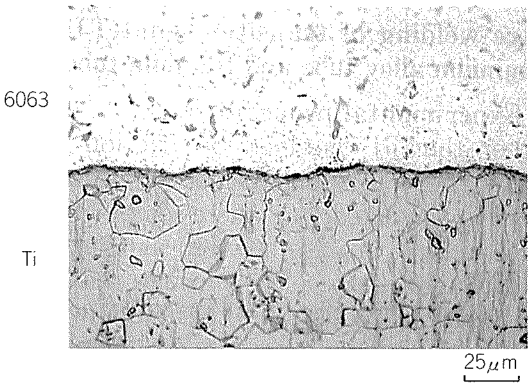
6063
Ti
25μm

Fig. 6 Micro-structure of friction weld interface (As friction welded).

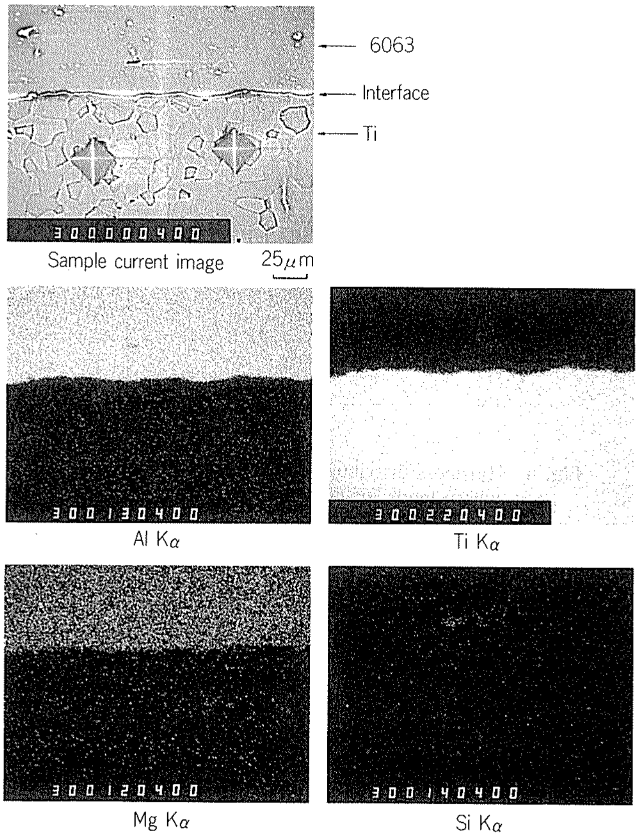
6063
Interface
Ti
300000400
25μm
300130400
300220400
300120400
300140400

Sample current image

Al Kα

Ti Kα

Mg Kα

Si Kα

Fig. 7 EPMA analysis at friction weld interface (As friction welded).

change till the interface, that is, neither softening by frictional heat nor hardening by friction and upset phases are observed.

By comparing hardness distribution of weld under No.12 condition with weld under No.13 condition, a similar tendency was recognized, but the softened zone at 6063 base metal side resulting from frictional heat was wider under the latter than under the former. It may come from the lower upsetting pressure under No.13 condition, so that frictional heated zone might not be squeezed out and be left. The lower strength shown in **Table** 8 seems to result from the wider softened zone as shown in **Fig.** 8.

3. Arc welding of transition joint(TJ) to aluminium alloy tube and titanium tube plate

3.1 Experimental procedures

Whether the TJ obtained by friction welding mentioned above is applicable or not was investigated by the simulated test where joints were made with TIG welding process between aluminium alloy tube and titanium tube plate through the TJ.

The materials used in this experiment are shown in **Table 9**, where aluminium alloy tube and titanium tube plate are 6063−T6 and TP49−0, respectively, and tensile properties of the former are noted below the table. The TJs were made from the specimens friction welded under Nos.12 and 13 conditions in **Table 7**.

Edge preparations and dimensions of TJ, 6063 aluminium alloy tube and titanium tube plate are shown in **Fig. 9 (a),(b)** and **(c),** respectively.

TJ was machined to 40mm long so that the friction weld may be included within a tube plate whose minimum thickness used commercially is about 50mm. In addition, the friction welds are located at three different distances from the centerline of TIG arc weld between TJ and 6063 aluminium alloy tube or titanium tube plate in order to examine the effect of welding thermal cycles on properties of the friction welds. They are shown in Type A, B and C of **Fig. 9 (a)**.

The welding conditions are shown in **Table 10**. The welding processes used were AC−TIG and DCSP−TIG welding for aluminium alloy side of TJ and 6063 aluminium alloy tube, and titanium side of TJ and titanium tube plate, respectively.

The examples of thermal cycles obtained during

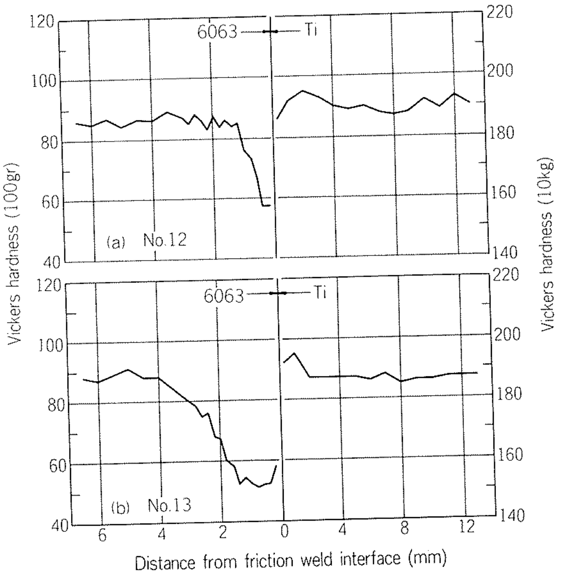

Fig. 8 Hardness distribution of friction welds, where loads for 6063 and Ti sides are 100g and 10kg respectively.

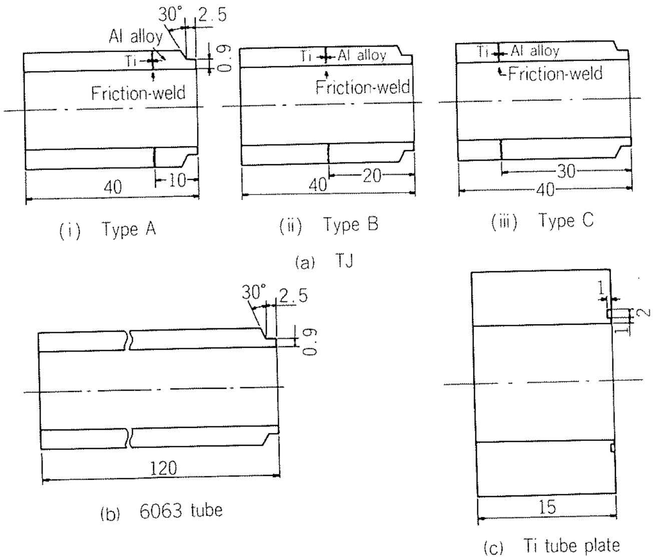

Fig. 9 Schematic representation of edge preparations and locations of friction welds at TJ.

Table 9 Test materials.

Materials			Dimensions			
			Outside diameter (mm)	Inside diameter (mm)	Wall thickness (mm)	Length (mm)
Transition-joint by friction welding, TJ	Al alloy	6063−T83	26.9	21.5	2.7	100
	Ti	TTP49−O	〃	〃	〃	50
Al alloy tube		6063−T6$^{(1)}$	26.4	22.4	2.0	125
Ti tube plate		TP49−O	52.0	27.1	15.0	−

(1) Yield strength : 19kgf/mm^2, Tensile strength : 22kgf/mm^2, Elongation : 27%

Table 10 Arc-welding conditions.

Welding	Welding process	Welding rod	Welding current (A)	Welding speed (cm/min)	Ar gas flow rate (l/min)
Welding between Al alloy of TJ and 6063 aluminium alloy tube	AC·TIG	4043−ϕ1.6mm	55~60	11.3~12.8	12
Welding between Ti of TJ and Ti tube plate	DCSP·TIG Metal−run	−	60	24	12

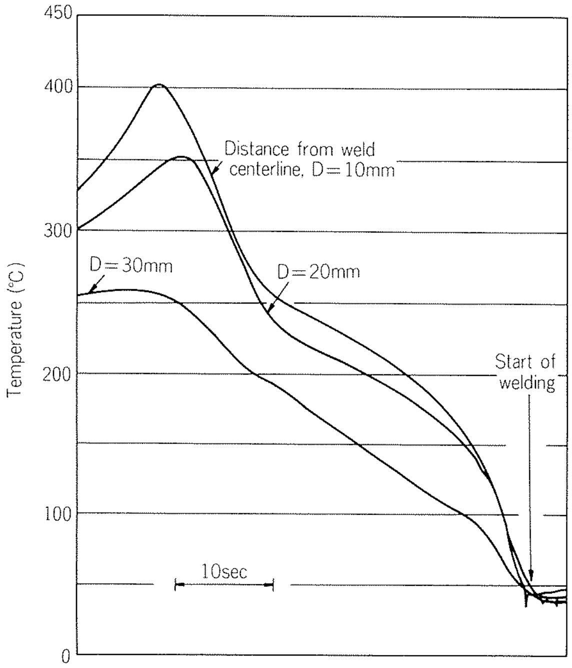

Fig. 10 Weld thermal cycles by AC·TIG welding.

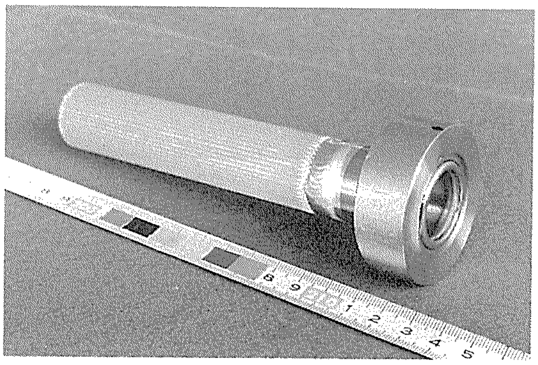

Fig. 11 Appearance of joint.

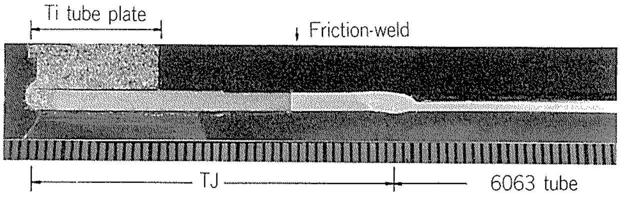

Fig. 12 Cross sectional view of joint.

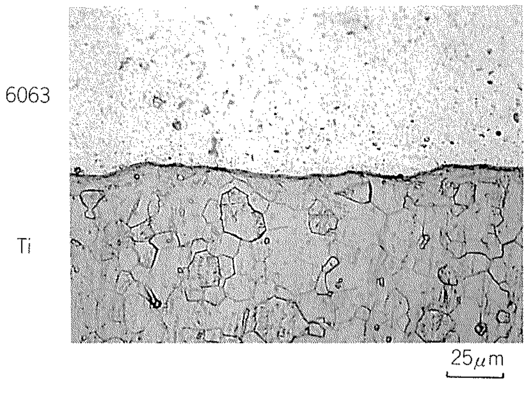

Fig. 13 Micro-structure of friction weld interface (Weld thermal cycled).

AC−TIG welding of TJ and 6063 aluminium alloy tube are shown in **Fig. 10**. According to the result, it becomes clear that the friction welds in A, B and C types of TJs are subjected to such a thermal cycle that heats to them about 400℃ at maximum temperature, or hold them for 50sec in maximum period at least about 250℃ (though such a long holding time is not depicted in **Fig. 10**).

3.2 Experimental results and discussion

(1) Appearance of joint

During welding of both TJ−6063 aluminium alloy tube and TJ−titanium tube plate, neither fracture nor cracking were observed in all types of TJ, which were made from the specimens under Nos.12 and 13 conditions of **Table 7**. The example are shown in **Fig. 11**.

(2) Structure of weld in joint

Fig. 12 shows the cross sectional view of a joint. The sound welds are obtained in both welds of TJ −6063 aluminium alloy tube, and TJ−titanium tube plate. It is also clear that any defects are not observed at friction welds. It is necessary to keep the reinforcement of back-bead at the weld between TJ and 6063 aluminium alloy tube as little as possible in order to make a titanium tube adhere to the inside of TJ sufficiently.

Fig. 13 shows the typical micro-structure of friction weld in the joint (**Fig. 12**). Any difference is not observed in the structure even if the structure is compared with as friction welded one in **Fig. 6**. Growth of diffusion layer, formation of alloying layer and defects such as micro-cracking are not recognized microscopically.

Distributions of elemehts such as Al, Ti and Si at friction welds of the joint were analyzed by EPMA. However, the influence of arc welding on the distributions were not still observed and a similar result to as friction welded one was obtained. **Figs. 14** and **15** show the typical results of EPMA analysis. In **Fig. 15** the distributions are compared between weld thermal cycled and as friction welded interfaces.

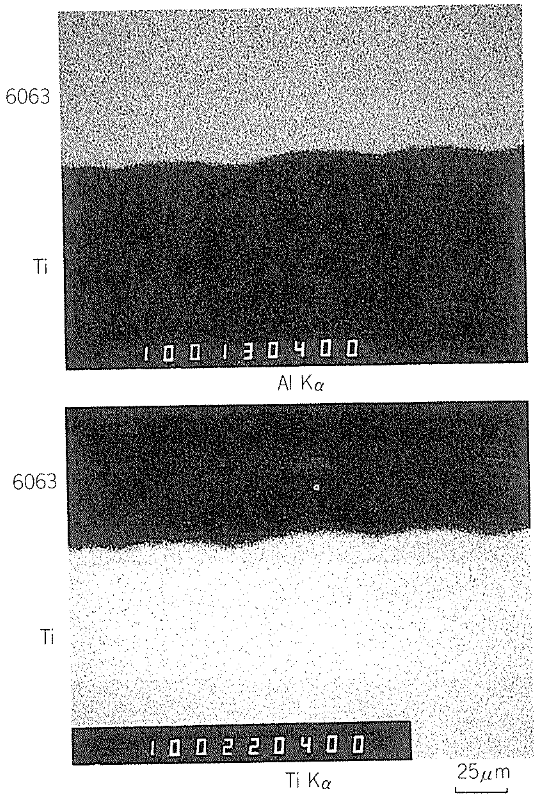

Fig. 14 EPMA analysis at friction weld interface of TJ (Weld-thermal cycled).

In these examinations there were no differences among types or specimens of TJs.

Fig. 16 shows the micro-structures of the TIG welds shown in **Fig. 12**. The sound welds are obtained both in TJ−6063 aluminium alloy tube and in TJ−titanium tube plate, and they do not have any weld defects such as crack and lack of fusion. In the case of titanium weld, hydride and nitride which are often formed resulting from insufficient shielding during welding are not also observed.

(3) Mechanical properties of joint

Fig. 17 shows the hardness distribution in the joint. At the aluminium alloy side of the TJ, the

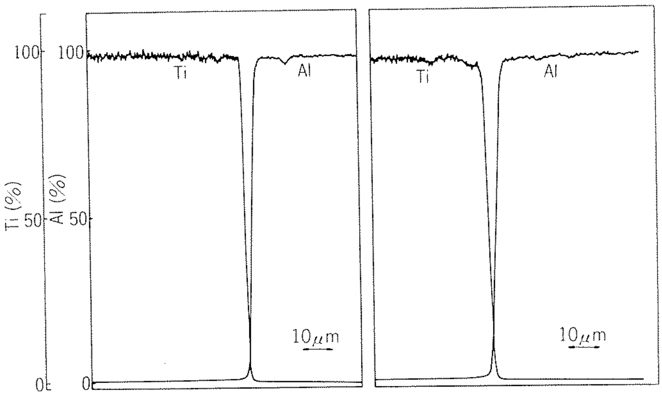

(i) Weld thermal cycled (ii) As friction welded

Fig. 15 EPMA analysis at friction-weld interface of TJ.

(a) Weld between Al alloy of TJ and 6063 aluminium alloy tube

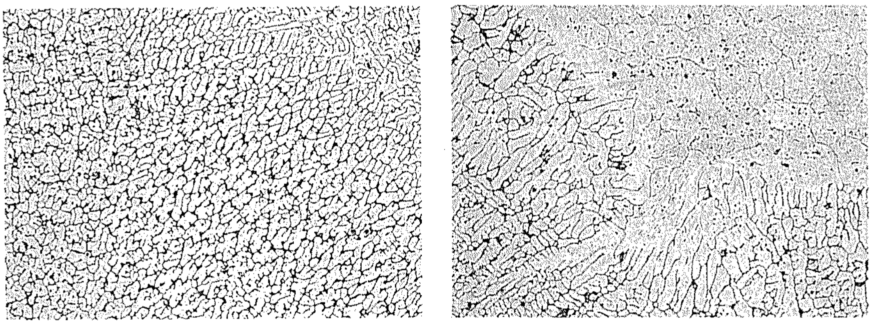

(i) Weld metal (ii) Weld bond

(b) Weld between Ti of TJ and Ti tube plate

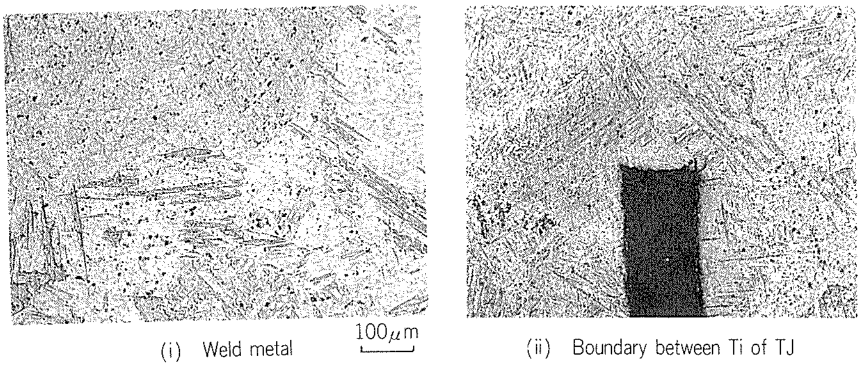

(i) Weld metal (ii) Boundary between Ti of TJ and Ti tube plate

Fig. 16 Micro-structures of TIG-welds at joint.

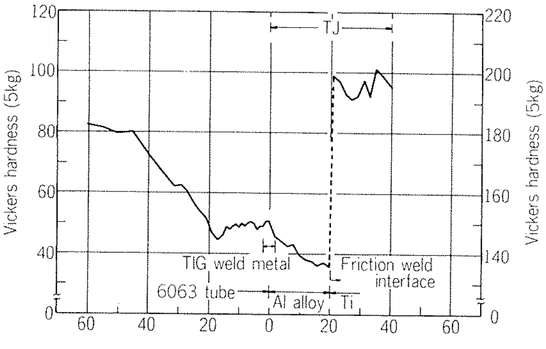

Fig. 17 Hardness distribution at joint.

Table 11 Results of tensile test of joints.

Type of TJ	Tensile strength(kgf/mm^2)	Position of fracture
A	14.7～16.3	6063 base metal
B	15.1～15.7	〃
C	14.3～15.3	〃

hardness becomes below about 50(Hv) and a little lower than that of as friction welded specimen due to arc welding of TJ and 6063 aluminium alloy tube. While at the titanium side of the TJ, a similar hardness to that of as friction welded specimen is obtained.

In hardness examination of the joint, the remarkable increase was not recognized both at friction weld interface and at arc weld of titanium part in TJ, and this fact suggests that growth or formation of diffusion or alloying layer at the former, and that of hydride and nitride at the latter do not occur.

Tensile strengthes of the joints shown in **Fig. 11** are listed in **Table 11**. The fractures occurred at the base matal of 6063 aluminium alloy tube in all specimens and any failure was not observed over the TJ though these results seem to be mainly due to the difference of wall thickness of materials which compose of the joint. The tensile strength is in the range of 14.3～16.3kgf/mm^2, which nearly equal to that of 6063−0 aluminium alloy.

From these results, it seems that the friction weld of TJ with dimensions used in this study is not affected by the arc weld thermal-cycle which is applied here. And there were not any differences between specimens of Nos.12 and 13 and those among A, B and C types shown in **Fig. 11**. Therefore, it is expected that the tubular TJ of aluminium alloy and titanium made with friction welding is put to practical use from the point of view of welding process, as shown in **Fig. 18**.

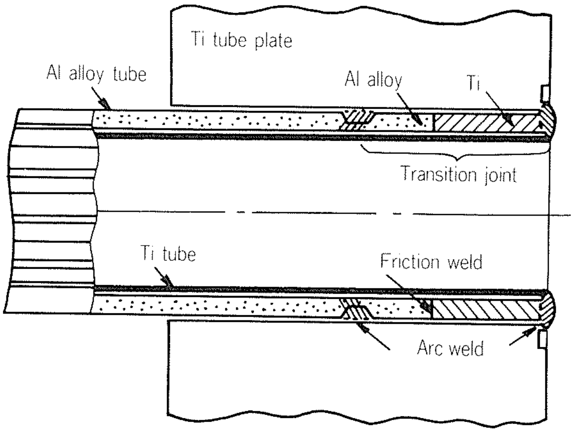

Fig. 18 Joining process.

4. Conclusions

The bi-metal (duplex) tube composed of aluminium alloy and titanium will be applied to heat-exchangers such as condenser of power plants and apparatus for OTEC (Ocean Thermal Energy Conversion) system in order to make a good use of each characteristic of the dissimilar materials. However, the joining process of such a bi-metal tube to titanium tube plate has still been left insufficient in points of corrosion-resistance, leak-tighthess and strength of the joint.

The objective of the present study is to produce the high quality of joint by using tubular transition joint (TJ) of aluminium alloy and titanium made with friction welding process.

The study was carried out on producing the TJ by friction welding process, firstly, and, followed by joining the TJ to aluminium alloy tube and titanium tube plate by TIG arc welding.

The results obtained are as follows.

(1) Sound welds between 6063 aluminium alloy and titanium tubes with 26.9mm diameter and 2.7mm thickness were obtained by friction welding process. The welds had satisfactory mechanical properties and the formation of diffusion or alloying layer was not observed at the interface.

(2) Reliable joints were made with TIG welding process between 6063 aluminium alloy tube and titanium tube plate through the TJ produced from the friction weld mentioned above. The strength of the joint had a similar value to that of 6063−0 aluminium alloy and the interface at friction weld of the joint seemed not to be affected by the arc weld thermal-cycle used in this study.

Therefore, it is expected that the tubular TJ of aluminium alloy and titanium made with friction welding is put to practical use.

Reprinted from SUMITOMO LIGHT METAL TECHNICAL REPORTS (Title No. R-313)

技術資料

Present and Future of Aluminium Alloys for Transport in Japan*

Shiro Sato**

住友軽金属工業株式会社技術研究所

技術資料

Present and Future of Aluminium Alloys for Transport in Japan*

Shiro Sato**

To meet the demand to increase speed and safety in transport with minimal energy, aluminium alloys have been increasingly used by Japanese transport industries. This paper reviews the state of the art of aluminium alloys and related technologies. In the automobile industries, in addition to the main established uses, castings for engines and engine parts, there are other important established uses. These are heat exchangers for automobile air conditioning units made by brazing fins and multi-pore tubes and fabricated or cast car wheels. Use of aluminium alloy body shells for rolling stocks has increased steadily. Main alloys being used are standard and/or modified Al−Zn−Mg and Al−Mg−Si alloys. Thermo-mechanical process to manufacture aircraft stringer materials of 7075 of modified properties has been developed.

Among the varieties of P/M products of aluminium alloys under investigation, high silicon aluminium alloys are going to be used commercially due to their excellent wear resistance. FRM pistons have been developed successfully, in which ceramic fiber is embedded at top ring portions. The modificatinos of present technologies and the applications of new technologies are key factors for future growth of aluminium in transports.

1. Introduction

All the transports have common and eternal requirements to enhance the speed, the safety and the comfortability with minimal energy and cost. Aluminium alloys can meet these requirements. Statistical data, **Fig. 1**[1], on the consumption of aluminium in Japan in ten major field of application reveal aluminium consumption for transport became number one last year and it's annual growth rate in average during these ten years was highest (7.8% in transport vs. 4.8% in the total average).

2. Automobile

It is reported that the total amount of aluminium alloys in one Japanese car is about 40kg excluding that for wheels. Majority of the applications is the castings for engines which include pistons, cylinder heads, cylinder blocks and intake manifolds. These aluminium alloy castings have already been regarded as being standard materials and are supplied by mass production system.

As for the use of wrought aluminium alloys in automobiles, varieties of trials have been made but,

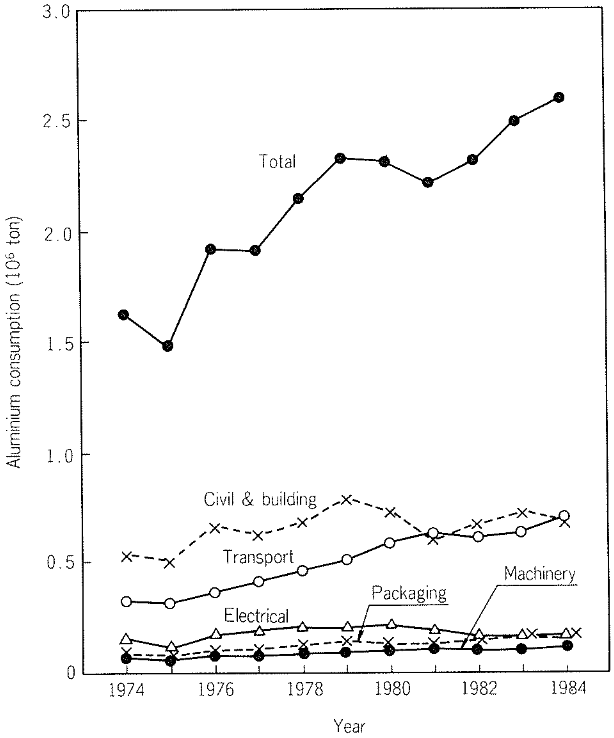

Fig. 1 Annual change of aluminium consumption in Japan, 1974−1984[1].

---

* This paper was presented at 1985 Fall Meeting of European Material Research Society on Advanced Material R&D for Transport, Strasbourg, France, Nov. 26∼28, 1985.

** Technical Research Laboratories, Dr. Eng. Sci.

except some limited cases mentioned bellow, most of them have not necessarily been successful in establishing the positions of standard materials. For example, aluminium alloy bumpers made by extruded 7021 had once been used in one Japanese car model but they could not keep their position due to the cost disadvantage compared to steel or reinforced plastics bumpers.

Aluminium heat exchangers used for condensers and evaporators of car air conditioning units have been developed in this decade and being used exclusively. They are manufactured by brazing of extruded multi-pore tubes with corrugated clad fins. Selection of alloys for tubes and fins are made taking into consideration the requirements for corrosion resistance, strength and fabrication cost. In the course of developmental works particular emphasis was placed upon the sophisticated combination of alloys of tubes and fins to guarantee the corrosion resistance of tubes. In the process of manufacturing, flux (chloride) dip brazing, vacuum brazing and innert gas brazing (VAW process) are applied and fluoride flux brazing is also being tested.

In case of development for mass production of evaporators of car air conditioning units by vacuum brazing, co-operation between a manufacturing company and an aluminium company has been conducted. Extruded flat multi-pore tubes were bent in serpentine shape and vacuum brazed with corrugated fins as shown in **Fig. 2**. Factors considered in alloy selection were the suitable mechanical properties, the production cost of tubes and fins, the ease and reliability in vacuum brazing and, particularly, the corrosion resistance of tubes in combination with fins[2,3,4]. Alloys designated were as following,

Tube : Extruded multi-pore tube, Al$-$0.3%Mn$-$0.15%Cu (MC03)
Fin : Brazing sheet cladding on both side,
core : Al$-$1%Mn$-$0.04%Sn
clad : 4343 (Al$-$7.5%Si)

Corrosion potential of alloys for tubes and fins are shown in **Fig. 3** and **4** respectively[5]. **Fig. 3** shows that the addition of copper and manganese to aluminium raises the corrosion potential, whereas, **Fig. 4** shows that the addition of tin lower the corrosion potential. It is clear from both data that the tubes (MC03) in an evaporator are expected to be protected by the fins because the tubes are cathodic to the fins. In order to maintain satisfactory corrosion resistance, one of the essential points in the practice of vacuum brazing is to cool the evaporators rapidly after passing the hottest zone of furnace. Rapid cooling is useful to prevent the precipitation of tin in the fin core and the increased amount of solutionized tin is essential for the fin to play the role as the active anode.

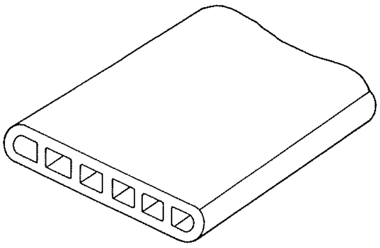

(a) Multi-pore tube

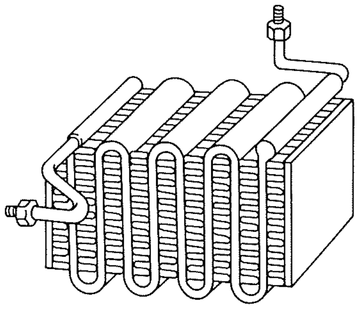

(b) Evaporator

Fig. 2 Aluminium evaporator for automobile air conditioning unit made by vacuum brazing.

Furnace brazing under inert gas atmosphere (VAW process) is also used to manufacture aluminium heat exchangers. As core material of brazing sheet for VAW process, zinc containing aluminium alloy is useful because of freedom from vaporization (dezincification) problem. This alloy fins are efficient to protect tubes from corrosion as sacrificial an-

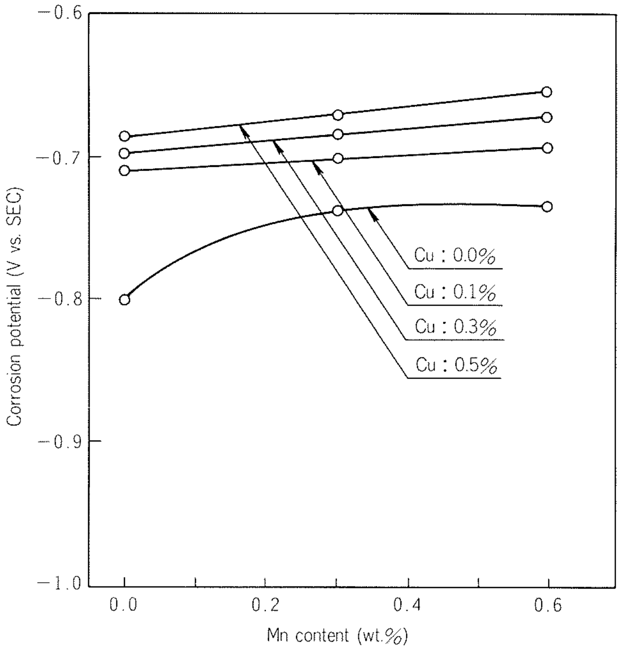

Fig. 3 Potentials of Al$-$Mn$-$Cu alloys in 3% NaCl aq. pH3[5].

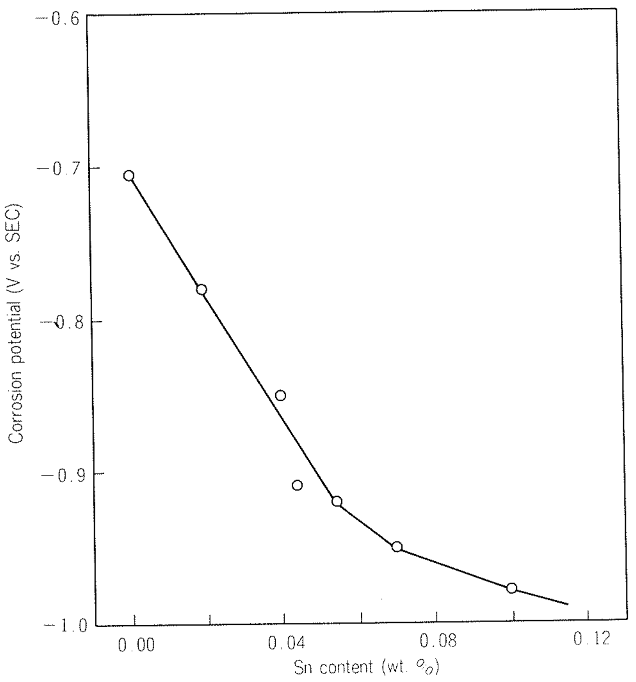

Fig. 4 Potential of Al−1%Mn−Sn alloys in 3% NaCl aq. pH3[5].

odic members in heat exchangers.

Aluminium wheels can provide with the fashionable design and the appreciable reduction of the unsprung mass. Total number of aluminium wheels produced in Japan was 8.5 million pieces in 1984. More than half of them were made by single body castings. Casting processes are low pressure casting, conventional gravity die casting, pore free (oxygen) die casting and squeeze (high pressure) casting. As non casting type aluminium wheels, so-called fabricated wheel of two piece type and three piece type are also widely used. During the five year period, the market share of two piece wheels[6] has greatly expanded. A two piece type wheel is fabricated by welding a disk (mostly by casting) with an aluminium alloy sheet rim which is roll formed from a ring made by flash-butt welding. In flash-butt welding the rim, rectangular AC current is preferably applied rather than conventional (sine curve) AC current to obtain sound weld. Aluminium alloy used for rim is strength modified 5454 and that for disk is AC4C (Al−7%Si−0.3%Mg casting) or 5454 (press formed). Welding of the disk to the rim is made by MIG using 5356 electrode wire. Advantages[6] of two piece type wheel over casting type wheel are (1) weight saving of 15−30%, (2) reduction of moment of inertia by 20−30%, (3) reduction of unbalanced mass by 70−80%.

Recently, the use of aluminium extruded hollow shapes is increasing for frames of autobicycles. In selecting alloy for hollow shapes, factors taken into account were such properties as mechanical strength, extrudability, anodizing and welding and JIS 7NO1 and 7003 were selected. The average amount of use of aluminium alloys is 10−15kg per one autobicycle.

Much efforts had been made by aluminium manufacturers and by automobile companies toward the commercial application of aluminium auto body sheet. First application of aluminium alloy sheet has been realized since mid of 1985. Body sheets being used are Al−4.5%Mg−1.5%Zn[7] (T4 temper) and are used for inner panels, outer panels and stiffeners of engine hoods of high performance luxury cars. This body sheet is called as 30−30 since it has 30kgf/mm^2 in tensile strength and 30% in elongation. Chemical composition and mechanical properties of 30−30 alloy sheet are shown in **Table 1**. Additional cases of commercial uses of aluminium alloy body sheets are expected to come up.

As far as aluminium radiator concerns, Japanese automobile industry had been more conservative than either European and United States industres. It seems, however, automanufacturers have started to shift from conventional radiators to aluminium radiators and now aluminium radiators are installed in several models. It is expected that a big market for aluminium alloys for radiators which is estimated to be some ten thousand ton of alloy per year will be created. In selecting alloys for car radiators, one of the key factors should be corrosion resistance. The long experiences of aluminium heat exchangers for air conditioning units will be most valuable in this evaluation. Manufacturing process of radiator being applied is to join the tubes made by high-frequency induction welding of coil with the corrugated fins by furnace brazing. Furnace brazing processes being applied are vacuum brazing, inert gas (nitrogen gas) brazing (VAW process) and fluoride flux brazing. Cross-fin type radiator (Sofica type) is also being applied.

Table 1 30−30 alloy, chemical composition and typical mechanical properties of auto-panel sheet (Typical value)[7].

1) Chemical composition (wt. %)

Si	Fe	Cu	Mn	Mg	Cr	Zn	Ti	Al
0.06	0.15	0.19	<0.01	4.4	<0.01	1.5	0.01	Balance

2) Mechanical properties, (T4 temper)

Tensile strenght (kgf/mm^2)	Yield strength (kgf/mm^2)	Elongation (%)	(1)E value (mm)	(1)n value	(1)r value	(1)L.D.R.
30.5	14.7	30	9.7	0.29	0.68	2.14

(1) E : Erichsen test cup height, n : Strain hardening exponent, r : Average plastic strain ratio, L. D. R. : Limiting drawing ratio

3. Rolling stocks (Rail vehicles)

In Japan, the debut of first all aluminium rail vehicles (trains) was in 1962 and total number of all aluminium trains already manufactured is about 3200. During these periods, developments in technologies including alloy developments, designs, manufacturings and weldings have been achieved. It is well known that the Committee on the Aluminium Rolling Stocks sponsored by Japan Association of Rolling Stock Industries and by Japan Light Metal Association (1970-) has made a lot of contributions which are well documented in a report published in 1984[8]. In 1969, in order to produce the extruded shapes of large cross sectional area for structural purposes, Light Metals Extrusion Development Company equipped with a giant press of 9,500 ton was founded by a joint venture of major Japanese aluminium companies.

Aluminium alloys being specified in JIS and used for frames of train bodies are 5083, 6N01, 7N01, 7003. Their chemical compositions and mechanical properties with and without welds are shown in **Table 2**[9]. Alloy 6N01, known as a medium strength alloy, is excellent in corrosion resistance, in weldability and also in extrudability and often used for hollow shapes. Alloy 7N01 is a standard weldable Al−Zn−Mg alloy for structural application approximately equivalent to that developed in Europe. Alloy 7003 is a intermediate strength Al−Zn−Mg alloy developed in Japan with excellent extrudability and is suitable for large extruded shapes of thin wall. In this alloy, the modification of chemical composition, which includes the replacement of some magnesium with zinc and the addition of zirconium, makes this alloy ease in extrusion with minimal detrimental effects in strength and in sensitivity to stress corrosion cracking.

Table 2 Aluminium alloys of extruded shapes used for frames of train bodies specified in JIS H 4100[9].

1) Chemical compositions (wt. %)

Alloy	Si	Fe	Cu	Mn	Mg	Zn	Zr
5083	<0.40	<0.40	<0.10	0.40-1.0	4.0-4.9	<0.25	—
6N01	0.40-0.9	<0.35	<0.35	<0.50*	0.40-0.8	<0.25	—
7N01	<0.30	<0.35	<0.20	0.20-0.7	1.0-2.0	4.0-5.0	<0.25(0.15)
7003	<0.30	<0.35	<0.20	<0.30	0.50-1.0	5.0-6.5	0.05-0.25

* Mn+Cr <0.50

2) Mechanical properties of extruded shapes

Alloy	Temper	Tensile strength (kgf/mm^2)	Yield strength (kgf/mm^2)	δ (%)	Fatigue strength (10^7cycles) (kgf/mm^2)
5083	H112(340~410℃)	32.6	18.2	18	13.5(1)
6N01	T5(170~180℃, 8hr)	27.8	24.3	13	12.0(1)
7N01	T5(120℃, 24hr)	39.1	32.6	16	15.5(1)
7003	T5(150~160℃, 8~16hr)	35.0	29.6	15	11.3(2)

3) Mechanical properties of MIG butt welded joints with beads.

Alloy	Temper	Filler metal	Tensile strength (kgf/mm^2)	Yield strength (kgf/mm^2)	Fatigue strength (10^7cycles) (kgf/mm^2)
5083	H112	5356	30.0	15.5	7.0(1)
6N01	T5	5356	19.7	13.4	6.7(1)
7N01	T5	5356	34.0	24.6	7.0(1)
7003	T5	5356	31.8	22.1	9.2(2)(3)

(1) axial load, S. R. =0, σ_{max}. (2) Plain bending, S. R. =−1

(3) Beads off

The aluminium car body shells manufactured in Japan are classified in three types as shown in **Fig. 5**[10]—A. Car body shells of conventional design made by spot welding of frames (extruded shapes) and plates, B. Car body shells made by longitudinal welding of thin large extruded shapes, C. Airtight, increased stiffness and large sized car body shells made by spot welding of extruded shapes and plates.

New bullet trains of the 200 series were designed by type C as shown in **Table 3** and **Fig. 6**[11], in which extruded shapes of 7N01 and 7003 were used for main frames and plates of 5083 for outer sheathing. It is reported that one of the most remarkable merits of aluminium car body shells designed by longitudinal welding of extruded shapes (type B)

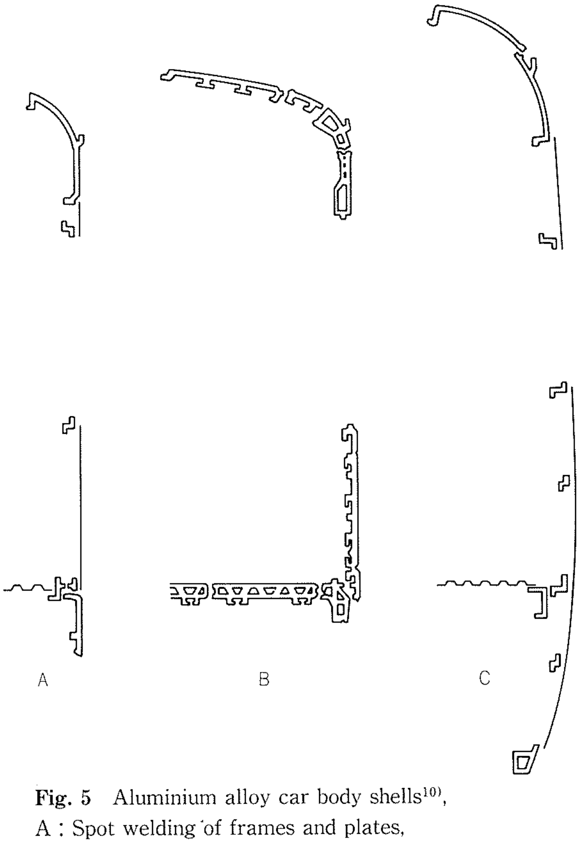

Fig. 5 Aluminium alloy car body shells[10],
A : Spot welding of frames and plates,
B : Longitudinal welding of large extruded shapes,
C : Airtight, increased stiffness and large sized.

Table 3 200 series bullet trains used for Tohoku−Jyoetsu lines[11].

Start of operation	October 1980
Aluminium alloys	Plates : 5083, 7N01 Shapes : 7N01, 7003, 5083, 5052, 6063
Length, width, height	24,500, 3,380, 4,000 (mm)
Total weight	56.5 (ton)
Weight of body shell	7.5 (ton)

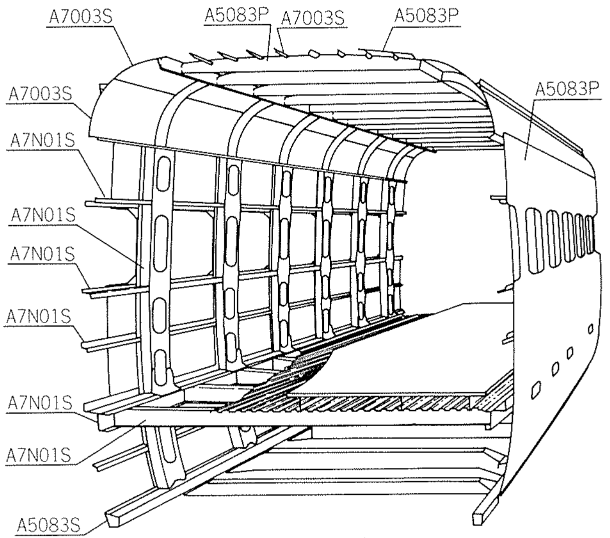

S : Shape, P : Plate

Fig. 6 Structure and alloys of 200 series car body shells used for Tohoku−Jyoetsu bullet trains[11].

over type A is in the appreciable reduction of labour cost for welding. For example, the total length of welding and the total number of spot welding for a car body shell by type A compared to type B were reported to be 357 m vs. 1,021 m and 3,716 vs. 516, respectively. Remarkable reduction of number of spot welding in type B means significant labour cost saving. Hence, car body shells by type B are expected to be used much more for rolling stocks in the future.

4. Aircraft

It seems growth of Japanese aircraft industry has not been fast but steady. Japanese aluminium industry has not necessarily been perfect supplier to aircraft industry. Economical difficulties caused by limited demand, but a wide variety of required products, have been major problems. As important aluminium alloys for future aircraft materials, aluminium−lithium based alloys are much interested. Two basic investigations for the industries are going on under some financial support by Japanese government. One is the basic investigation for process and properties of Al−Li based alloys and another is for novel process for production of high purity Al−Li master alloys.

In this paper, an introduction is made on the innovation of the manufacturing process of 7075 stringer materials used for longitudinal stiffeners of large passenger aircrafts. The original process and the innovated process are shown in **Table 4**[12,13]. In the original process, preferential grain growth occurs during the solution treatment at the portions of small reduction in taper rolling. Grain growth is very detrimental to strength and ductility. In the innovated process, grain growth during the solution annealing is prevented by uniform distribution of stabilized precipitated particles which are controlled by heating/cooling patterns during annealing process. Mechanical properties of stringer materials made by original and innovated process are shown in **Table 5**.

Table 4 Modification of manufacturing process of 7075 (0) for aircraft stringer materials[12,13].

	Original process	Modified process
Homogenizing	470℃ ×30hr	470℃ ×30hr
Hot rolling	400℃, 300mm→6mm thick.	400℃, 300mm→6mm thick.
Cold rolling	6mm→3mm thick.	6mm→3mm thick.
Annealing (1)	Slow heating (0.5～1℃/min), 420℃ ×2hr, cooling(25℃/hr)	Rapid heating (215℃/min), 450℃ ×3min, rapid cooling (50～100℃/min)
Annealing (2) (re-heating)	235℃ ×6hr, air cool	300℃ ×1hr, cooling (300℃→200℃, 20℃/min)
Finishing	Taper rolling, solution treatment (460～499℃, water quench), roll forming, cutting, aging (120℃ ×24hr)	

Table 5 Results of modification of 7075 sheet for aircraft stringer materials[12]. T6 : 120℃ ×24hr after 20% cold rolling.

		Original process		Modified process	
		0	T6	0	T6
Grain size	(μm)	250	−	40	−
Tensile strength	(kgf/mm²)	22.3	56.2	23.6	58.1
Yield strength	(kgf/mm²)	10.8	51.3	11.6	52.9
Elongation	(%)	18	13	19	16
Fatigue strength(1), (10^7 cycles)	(kgf/mm²)	−	14.6	−	16.4

(1) Plain bending, S. R.＝−1

5. Powder metallurgy

Rapidly solidified aluminium alloy powder exhibits unique merits of having fine microstructure and extended alloy range much beyond the solubility limit. Consequently, P/M processes using rapidly solidified aluminium alloy powder are attractive enough to develop advanced materials of heat resisting, of wear resisting and of high strength. Based upon the investigations made on P/M of several alloy series, hyper eutectic Al−Si alloy modified with

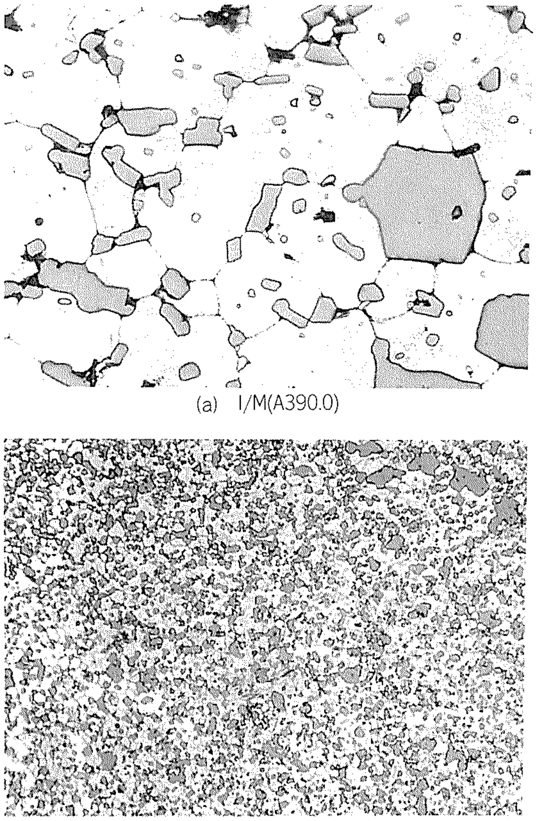
(a) I/M(A390.0)

(b) P/M

Fig. 7 Microstructures of extruded hyper eutectic Al−Si alloys by I/M and P/M processes[14].

the addition of some transition elements has been selected as the compressor sliding vane material for car air conditioning units and is being used successfully. In comparison with conventional materials such as I/M A390.0 (Al−17%Si−4.5%Cu−0.6% Mg, as extruded), P/M hyper eutectic alloy is much superior in wear and heat resistance and in decreasing thermal expansion. Microstructures of I/M and P/M of hyper eutectic Al−Si alloy are shown in **Fig. 7**[14]. As far as Japanese market concerns, applications of aluminium P/M are expected to be pioneered by the automobile industries in which connecting rods, forged pistons and miscellaneous engine parts would be next in line after the sliding vane.

6. FRM

Though FRM of aluminium has been being investigated in recent years, it's practical uses are limited. As a successful example, commercial production of high performance pistons with FRM was reported by Toyota Motor Co. as following[15]. Aluminium alloy AC8A (Al−12%Si−1%Cu−1%Mg−1.1%Ni) is casted under high pressure into mould in which a ring of preformed ceramic fiber is settled at the portion of top ring groove. **Table 6** presents the data on fiber and FRM pistons. Cross section of FRM piston is shown in **Fig.** 8. Preformed ceramic fiber is soundly filled with cast metal and embodied at the top ring portion. FRM pistons have been used in diesel engines of automobiles. Comparing with the conventional pistons in which Ni−Resist rings are embodied, FRM pistons are reported to have following merits;

Table 6 Fiber reinforced aluminium alloy pistons used for diesel engines by Toyota Motor Co[15].

(1) Fiber

Chemical composition	Al_2O_3 : 51%, SiO_2 : 49%
Dimension	Average diameter : 2.8μm
Density	2.6
Tensile strength	1300MPa

(2) Pistons

Position of fiber	Top ring groove
Volume ratio of fiber	6.6%
Matrix alloy	AC8A (Al−12%Si−1%Cu−1%Mg−1.1%Ni)

1) enough wear resistance equivalent to Ni−Resist embodied pistons.
2) low thermal expansion and excellent wear resistance resulting in fuel saving and noise reduction.
3) low density and high strength permitting small mass.
4) superior thermal conductivity making low temperature and high duty operation possible.

Connecting rods reinforced by fine stainless steel wire are reported to have been adopted in high performance engines by Honda Motor Co.[16]. New FRM connecting rod contains 50,000 bundled stainless steel wires, each 0.025mm in diameter, in pressure casted aluminium alloy. In comparison with a steel connecting rod, the FRM connecting rod is reported to save 30% in mass resulting 5% in power increment and 5−10% of fuel saving.

7. Conclusion

Though, until ten years ago, aluminium alloys had enjoyed the monopolistic position in light weight materials for transport, their position is now being challenged by new comming materials such as FRP. This situation, however, does not mean the maturity of aluminium alloys for transport. Continuous and ever increasing demands for weight saving materials in transport need the new and/or modified aluminium alloys under the competitive condition with other materials.

It is considered that two approachs are available

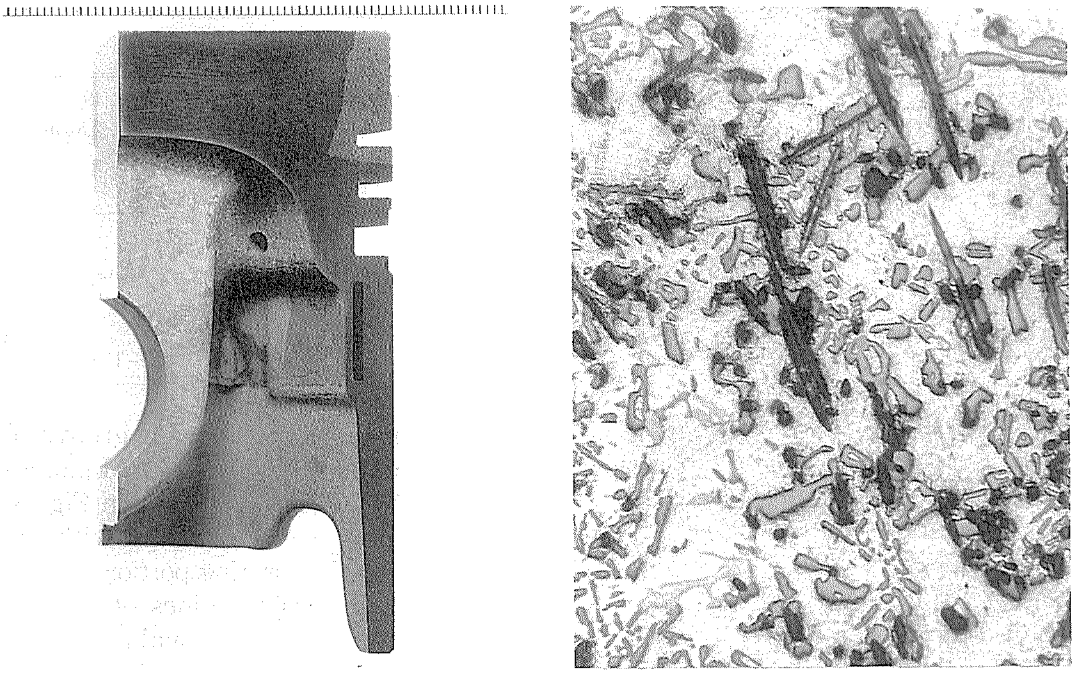
(a) Cross section (b) Microstructure

Fig. 8 Toyota's FRM piston[15].

for R&D of new and/or modified aluminium alloys in transport. One is the modifications of alloys as well as of process technologies being motivated by the experiences of application of aluminium alloys in the transport industries. Another is R&D of new aluminium alloys and of process technologies based upon the new concepts, such as rapidly solidified P/M, lithium containing alloys and FRM.

Acknowledgements

The author wish to acknowledge Prof. Dr. W.G.J. Bunk, Director of Material Lab. of DFVLR and Prof. Dr. Y. Murakami of Kansai Univ. for their encouragements to present the paper to the E−MRS Meeting. Acknowledgements are also due to several colleagues of Technical Research Lab. of Sumitomo Light Metal Ind., in particular to Dr. K. Takeuchi and Dr. Y. Baba for their assistance during this work. Mr. E. Morrice, consultant, is also acknowledged for his useful suggestion in preparing the paper in English.

References

1) Keikinzoku Digest, 1985−7−1
2) S. Terai, Z. Tanabe and T. Fukui : Japanese Patent 1,128,153 (1982), 1,128,154(1982).
3) Z. Tanabe, Y. Baba, T. Fukui and S. Kimura : U.S. Patent 4,244,756(1981).
4) Z. Tanabe, Y. Baba, T. Fukui, H. Ikeda, T. Miura and T. Sugiura : U.S. Patent 4,317,484(1982).
5) Z. Tanabe and M. Hagiwara : *Pre Prints for 32nd Annual Meeting of Japan Society of Corrosion Engineering,* (1985), P486−488.
6) K. Yoshihiro and M. Izumitani : J. Japan Inst. Light Metals, **34**(1984), 198.
7) T. Uno, Y. Baba and T. Amitani : SAE Technical Paper Series, 800348 "New 5xxx−Series Aluminium Alloy for Auto Body Sheet" (1980).
8) Light Metals Rolling Stock Committee : *Report of Light Metals Rolling Stock Committee No. 4 (1978∼1983),* 1, Japan Association of Rolling Stock Industries and Japan Light Metal Association (1984).
9) ibid., 3.
10) A. Sakaguchi and T. Kinoshita : J. Light Metal Welding and Construction (Japan), **22**(1984), 363.
11) H. Ohnishi and I. Kawanishi : 8) 175.
12) Y. Baba, T. Uno and H. Yoshida : Sumitomo Light Metal Technical Reports, **23**(1983), 120.
13) Y. Baba, T. Uno and H. Yoshida : U. S. Patent, 4,410,370(1983).
14) S. Inumaru and S. Yamauchi : Sumitomo Light Metal Technical Reports, **26**(1985), 57.
15) T. Donomoto : J. Soc. Automobile Engineers of Japan, **37** (1983), 884.
16) Nikkei Sangyo Shinbun (News Paper), Jan. 11, (1985).

Reprinted from SUMITOMO LIGHT METAL TECHNICAL REPORTS (Title No. R-314)

技術資料

Modernization of Aluminium Melting Process for Saving Fuel Consumption*

by Toshihiko Uehara**, Katsuaki Masaki***, Norifumi Hayashi****

住友軽金属工業株式会社技術研究所

技術資料

Modernization of Aluminium Melting Process for Saving Fuel Consumption*

by Toshihiko Uehara**, Katsuaki Masaki***, Norifumi Hayashi****

The modernest aluminium melting process has been developed for improving heat efficiency and productivity. The process consists of a tower type continuous melter and a box type main melter with the effective combination of convection and radiation type burner, under which an electromagnetic stirrer is equipped. Fuel consumption was saved about 40% and melting cycle was shortened by about 20%. Total fuel consumption of the melting process including heat recovery by waste gas boiler was about 850 BTU/lb.

Introduction

A modern melting and casting installation was constructed in 1983 at Sumitomo Light Metal Industries (S.L.M.) Nagoya Works, and various novel technical challenges were made for the efficient production of slabs for rolling. A large melting installation made up of a main melter and a tower melter, the core of the plant, was built with the following objectives:

1) Slab production capacity of 11,000,000 lb/month
2) Higher thermal efficiency and lower metal loss
3) Higher productivity
4) Relatively small melt lots and suitable for frequent alloy changes

For the achievement of these objectives, a new concept of melting furnace and various forms of advanced technology were adopted, which, coupled with S.L.M.'s accumulated knowhow of aluminium melting, permitted the completion of a highly modernized melting furnace. The entire system illustrated in **Fig. 1**.

The features of the new furnace (F34 melting complex) can be summarized as follows:

1) Composed of a sub-melter for ingot melting and a main melter chiefly for scrap melting.
2) The main melter has a burner system with both convection and radiation burners, and EMS at the bottom.
3) Waste heat is recovered as steam by means of a waste gas boiler.
(As the plant is located in a densely populated area, clean recovery systems were selected to avoid NOx increase from a recuperator).

Compared with a conventional melter, the total system uses up to 40% less energy. The combination of the sub-melter (we call it "tower melter") and main melter enabled not only energy saving but also a high melting rate, without increasing the melting loss. It also reduced the charging time and operation. In addition, the EMS simplified stirring and dross removal operations of the main melter, resulting in the reduction of the overall melting cycle by more than 20%.

About one month actual operations recently showed a mean thermal efficiency of as high as 59.6%. The fuel consumption with a reduction of the waste heat recovery is 844 BTU/lb. The main concepts of the tower and main melters, and the results of energy saving effect are described below.

2. System of new furnaces

2.1 Tower melter

The tower melter is an epoch-making highly efficient melting furnace, which, as a sub-melter, continuously melts ingots and supplies the hot melt to the main melter. The development of this unique furnace has realized automated charging, waste heat recovery by pre-heating ingots, and high thermal efficiency by continuous melting — all being almost impractical with conventional melting furnaces.

During the course of the development, the three types of furnaces illustrated in **Fig. 2** were discussed, based on a concept of the shaft furnace for copper

---

* This paper was presented at a Aluminum Industry Energy Conservation Workshop Ⅸ" Washington, D. C., U. S. A., held Apr. 8−9, 1986.

** Nagoya Works, Casting and Planning Department

*** Nagoya Works, Engineering and Maintenance Department

**** Technical Research Laboratories, Process Technology Department

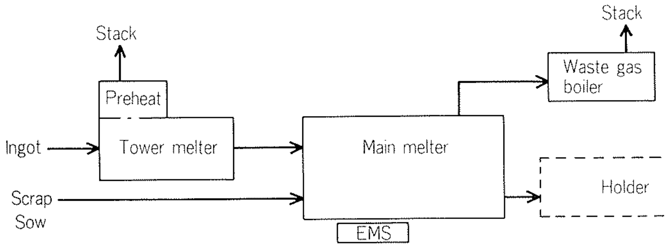
Stack
Preheat
Ingot
Tower melter
Scrap
Sow
Main melter
EMS
Stack
Waste gas boiler
Holder
Filter
Casting

Fig. 1 Total system of new furnaces, F34.

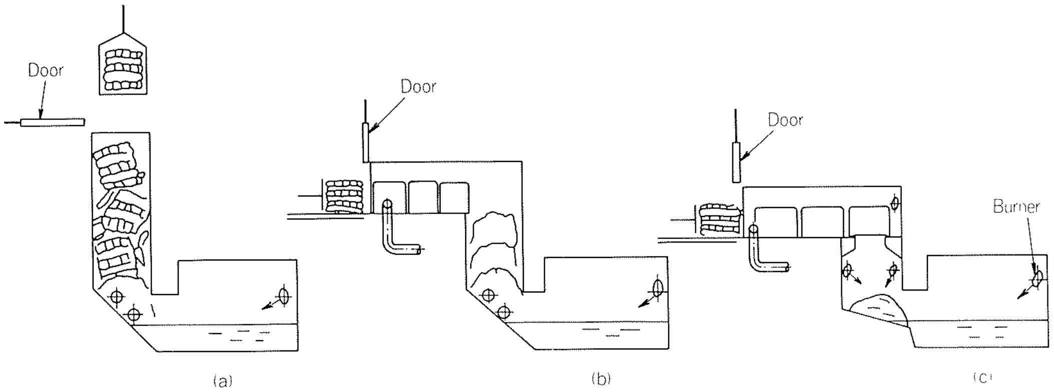
Door
Door
Door
Burner
(a)
(b)
(c)

Fig. 2 Three types of sub-melter.

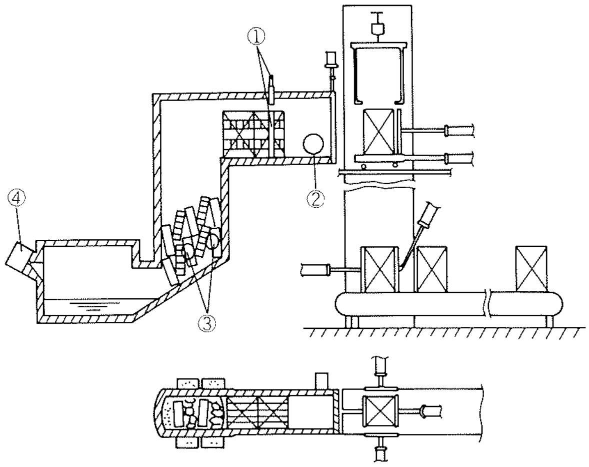

① : Damper ③ : Melting burners
② : Exhaust gas port ④ : Holding burners

Fig. 3 Total system of tower melter.

melting. (a) and (b) differ in pre-heating systems, and (b) and (c) differ in melting systems. As a result of several experiments and analysis using model devices, it was confirmed that (b) was the most effective for melting bundled 99.7% aluminium ingots.

The total system is illustrated in **Fig. 3** After ingots are placed on the conveyor by an operator, all processes from weighing and charging to melting and holding is performed automatically and matched with a given melting rate.

2.1.1 Pre-heating in the horizontal flue

About three bundles of ingots are charged onto the wear-resistant SiC floor by an ingot pusher. A damper is installed to prevent hot gases from

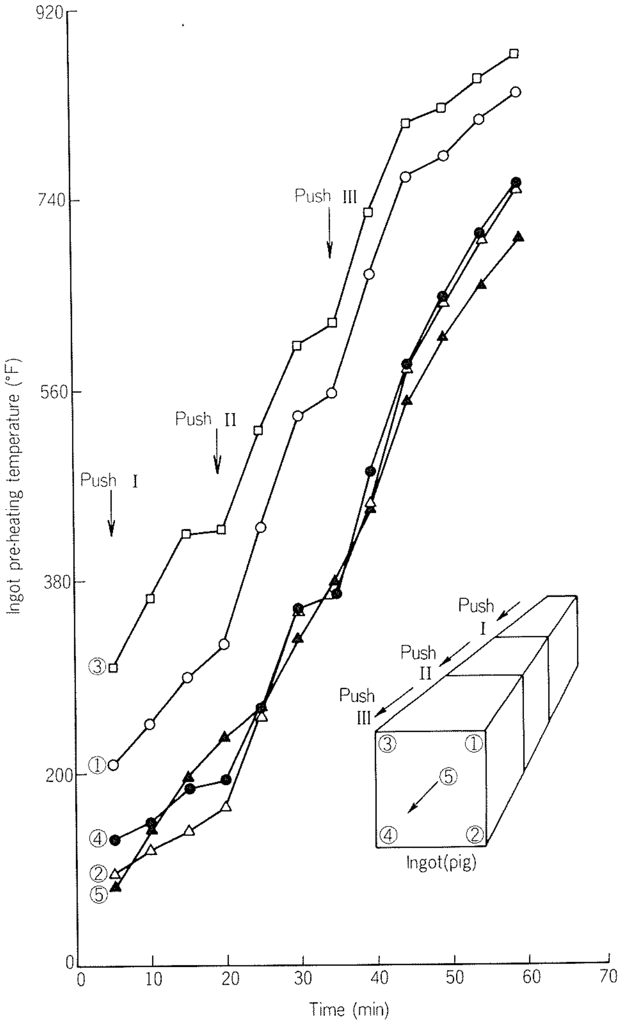

Fig. 4 Pre-heating characteristics of ingots in tower melter.

blowing through between the inside wall of the flue and the ingots (1 bundle=2,200 lb). The ingots are pre-heated up to about 750 °F (see **Fig. 4**).

2.1.2 Pre-heating and melting in the shaft

The ingots pushed out of the horizontal flue are turned over, thus breaking into the most efficient shapes for pre-heating by combustion gases. The section of the shaft is oval in shape to enhance pre-heating efficiency. About three bundles stay in the shaft and the ingots are uniformly heated up to near melting point, and are quickly melted on the dry hearth by impingement heating with the high-momentum burners.

Molten metal is held in the holding chamber, and after the temperature is raised, it is supplied to the adjacent main melter through a laundry. All combustion gases are used for pre-heating the material, which is eventually exhausted to the stack through a waste gas port near the lower part of the charge port. The waste gas temperature at the waste gas port is very low, or around 570 °F, as shown in **Fig. 5**. This evidently shows a high thermal efficiency of the tower melter.

The design specifications and actual operation data are shown on **Table 1**. The heat balance as illustrated in **Fig. 6** gives a very high efficiency of 77% for a continuous operation. A rough estimate of the efficiency distributed to each portion of the tower melter is as shown in **Fig. 7**.

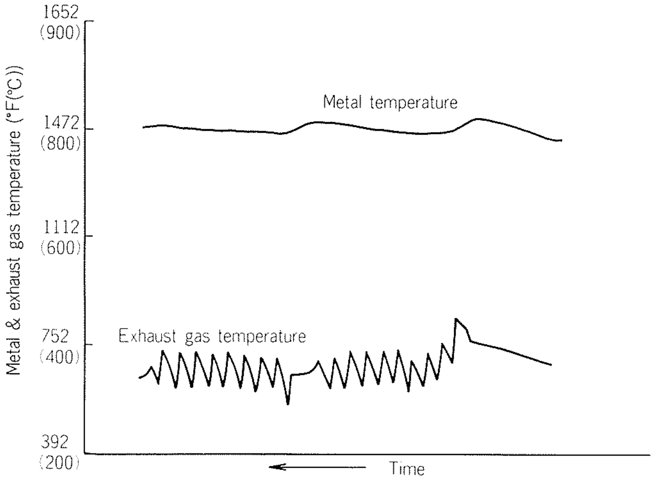

Fig. 5 Actual operation data of exhaust gas and metal temperatures in tower melter.

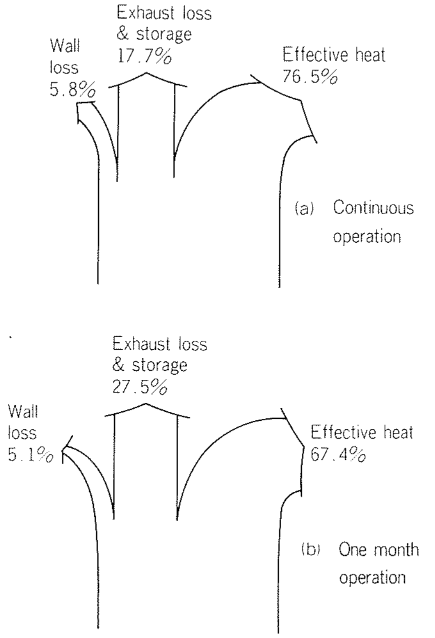
Wall loss 5.8%
Exhaust loss & storage 17.7%
Effective heat 76.5%
(a) Continuous operation
Wall loss 5.1%
Exhaust loss & storage 27.5%
Effective heat 67.4%
(b) One month operation

Fig. 6 Heat balance of tower melter.

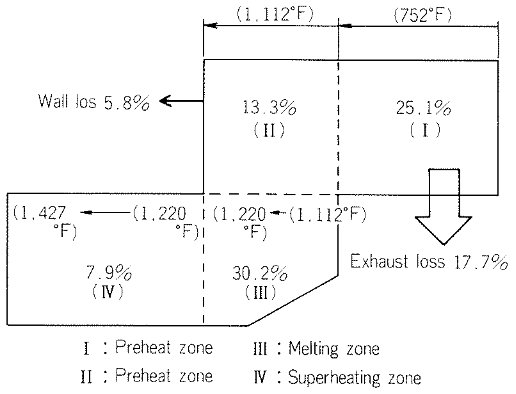
(1,112°F)
(752°F)
Wall los 5.8%
13.3%
(II)
25.1%
(I)
(1,427 °F)
(1,220 °F)
(1,220
(1,112°F)
7.9%
(IV)
30.2%
(III)
Exhaust loss 17.7%
I : Preheat zone
II : Preheat zone
III : Melting zone
IV : Superheating zone

Fig. 7 Estimated thermal efficiency of each zone of tower melter.
(Condition : Ambient temp. 68°F)

2.2 Main melter

Recently there has been a remarkable trend to-

Table 1 Design specifications and actual operation data.

		Design value	Continuous operation	One month operation
Melting capacity	(lb/hr)	7,700	8,400	7,700
Fuel consumption	(BTU/lb)	696	669	763
Molten metal temp.	(°F)	1,382	1,427	1,427
Flue exhaust gas temp.	(°F)	878	482～662	482～662
Thermal efficiency	(%)	73	76.5	67.4
Metal loss	(%)	<0.5	–	0.2～0.3
Dry hearth area	(FT^2)	16.1	–	–

ward convection melting using high-velocity combustion gases for aluminium melting furnaces. The advantages of convection melting have been investigated in our Nagoya Works based on the actual operation data compiled since the installation of the C.R.I. (Holland) melting furnace in 1980. It was found that convection melting gives a high thermal efficiency for initial heating of cold charge, but is not sufficient for the heating up of molten metal. As a result, it was decided that an efficient combination with radiation heat transfer is required.

2.2.1 Type of furnace

The new furnace was laid out as an extension of the existing furnaces, and due to space limitations, a side-charge type rectangular melting furnace with a capacity of 65 tons was selected. It is similar to but smaller than the existing maximum capacity furnace.

2.2.2 Type and layout of burners

As mentioned above, two types of burners, high-velocity burners for convection heat transfer and long-flame burners for radiation heat transfer were mounted. The former employs low maintenance LNG and the latter uses LS heavy oil with highly luminous flames. The layout is shown in **Fig. 8**. It was expected that the luminous gas from the long flame burners is swirled by turbulent jet streams of the high-velocity burners, giving effective combustion gas flows.

2.2.3 Monitoring camera in the furnace

A heat-resistant monitoring camera was mounted in the furnace so that the inside of the furnace could be continuously monitored. The conditions of the furnace are displayed on the TV screen in the control room. The behavior of burner flames observed by the camera is shown in **Fig. 9**. Clearly demonstrated is the process in which the long-flame burner flames are swirled by turbulent jet streams of the high-velocity burners. This was exactly what we had intended to achieve in arranging the burners.

2.2.4 Electromagnetic stirring system (EMS)

The system was installed at the bottom of the

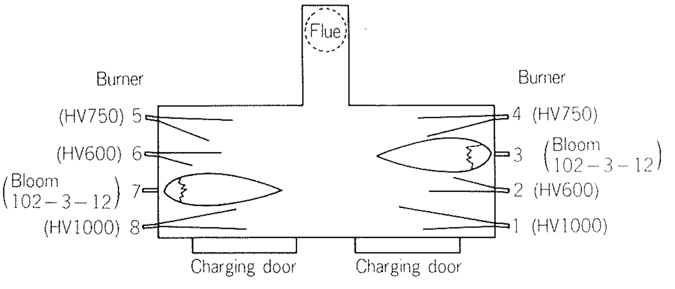
Flue
Burner
Burner
(HV750) 5
(HV600) 6
(Bloom 102-3-12) 7
(HV1000) 8
4 (HV750)
3 (Bloom 102-3-12)
2 (HV600)
1 (HV1000)
Charging door
Charging door

3. 7 : Long flame burner
1. 2. 4. 5. 6. 8 : High velocity burner

Fig. 8 Burner layout.

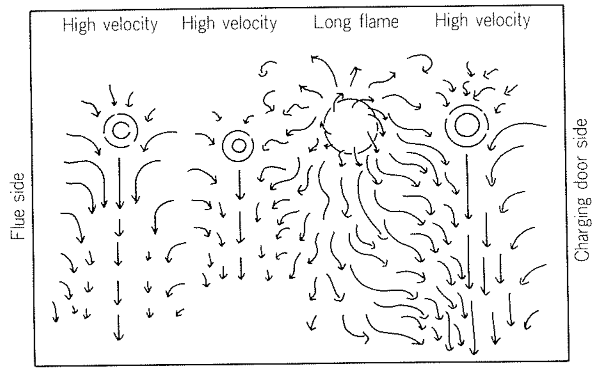
High velocity
High velocity
Long flame
High velocity
Flue side
Charging door side

Fig. 9 Flame configuration observed by monitoring camera.

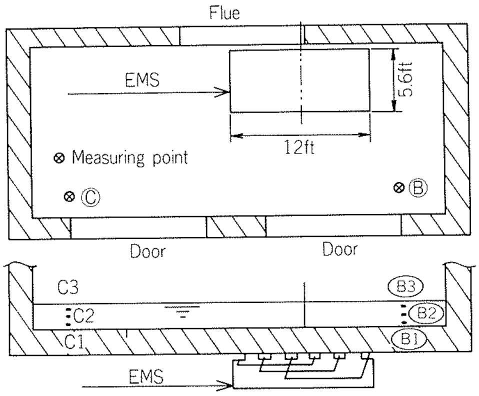
Flue
EMS
5.6ft
12ft
⊗ Measuring point
⊗ Ⓒ
⊗ Ⓑ
Door
Door
C3
C2
C1
B3
B2
B1
EMS

a) EMS location and measuring points of molten metal temperature.

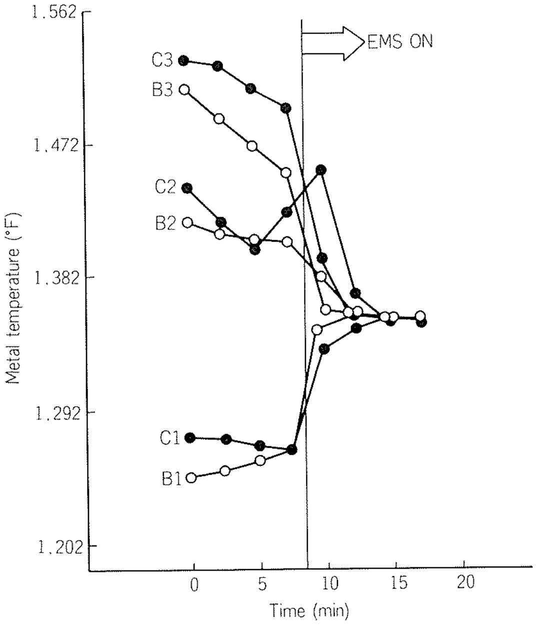

b) Effect on uniform temperature distribution of melt by EMS.

Fig. 10 EMS location and its effect.

furnace to eliminate temperature differences across the depth of molten metal, to improve accuracy of controlling molten metal temperatures, and to achieve the homogenization of the alloy components. **Fig. 10** shows the position of the EMS and the effect on the uniform temperature distribution of the melt.

It was confirmed that the temperature distribution of molten metal of over 300°F can be reduced to 40°F or less within a few minutes of the EMS operation, with the burners being turned off. In addition, as shown in **Fig. 11**, actual operations demonstrated that the difference of molten metal temperatures at the completion of each melting became less, excessive heating was prevented and the variations of melting cycles and thermal efficiency became less.

Although a quantitative evaluation of these effects is difficult, energy saving effect due to prevention of excessive heating may be estimated to be about 36 BTU/lb. Moreover, the EMS won popularity among the operators since molten metal flows caused by the EMS brings the dross together, resulting in easy skimming. It was expected that decreased temperatures in molten metal surfaces would increase the amount of heat transfer to the molten metal, but only a slight temperature drop occurs due to decreasing electromagnetic forces toward the surface, and thus there is presently no such remarkable effect.

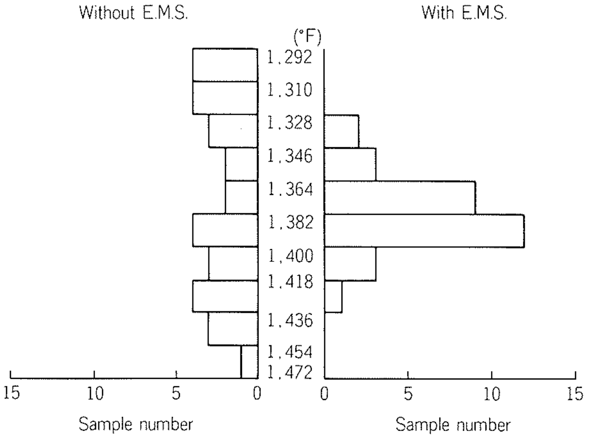

Fig. 11 Molten metal temp. variation at melting completion.

2.2.5 Operating pattern of the burners

The operating pattern of the burners is an essential technique that exercises a vital influence on the melting rate, fuel consumption, and melting loss rates. To determine the best operating pattern, many factors are to be considered such as the types of burners, firing rate, location,and the type and amount of charging material, etc.

We have developed operating techniques of maximum efficiency with a combination of convection and radiation type burners, based on the observations with the furnace monitoring camera.

1) The basic principles

i) From the start to the completion of melting, a burner pattern is determined at each of the three stages, initial, middle, and final.

ii) For optimum melting the length of time of each stage may be freely selected according to the type and quantity of charge, etc.

2) Burner patterns at each stage

i) Initial stage (Illustrated in **Fig. 12(a)**)

Drive hot gases into the spaces of cold charge

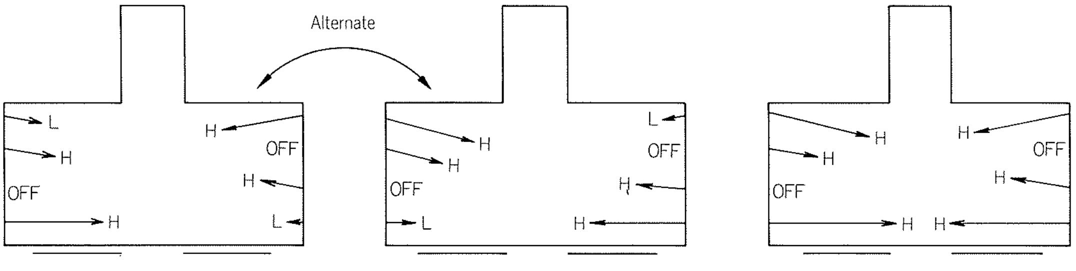

(a) Initial stage (b) Middle stage

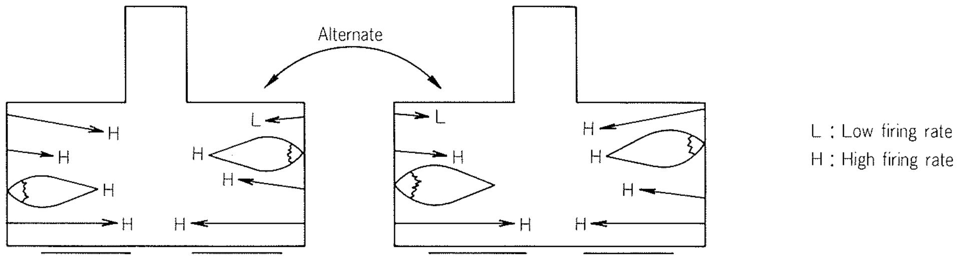

(c) Final stage

Fig. 12 Variation of burner firing pattern.

by positively using the high-velocity burners. Control the overall combustion rate, avoid local excessive heating, and uniformly heat all the cold charges as much as possible.

ii) Middle stage (Illustrated in **Fig. 12(b)**)

Set all high-velocity burners at high combustion. Even at this stage spaces are still left between the cold charges in the furnace so that convection melting by high-velocity burners is extremely effective.

iii) Final stage (Illustrated in **Fig. 12(c)**)

As melting proceeds, piles of materials begin to melt down. Set the long flame burners at high combustion and continue melting with added radiation.

With an increase of molten metal, operate the EMS intermittently to homogenize molten metal temperatures. The effect of the selected operating patterns are shown in **Figs. 13** and **14**. It can be seen from **Fig. 13** that the exhaust gas loss at the early stage of melting is less in convection heating than in radiation heating, which indicates that the former is more effective. **Fig. 14** shows that the thermal efficiency of molten metal in an increasing temperature stage is improved by the combination of convection and radiation type burners.

2.2.6 Waste heat boiler

As our plant is located in a densely populated area, the control of SOx and NOx emission is strictly enforced. Consequently, it was decided to use LNG as a main fuel and a waste heat boiler to recover the waste heat as steam, instead of using recuperators.

The current monthly production of our Nagoya Works is about 44,100,000 lb/month of rolled and extruded products, and the resultant steam is being used for heating hot rolling oil, degreasing coils in the cold rolling process, and welfare facilities of the employees.

When one ton of the steam from the waste heat boiler is effectively used, 2,789,500 BTU of fuel for the exclusive boiler can be saved. This we evaluate as the amount of heat recovered.

A heat-insulating cylindrical duct was built in an underground concrete tunnel to prevent heat loss in the long flue from the main melter to the waste heat boiler.

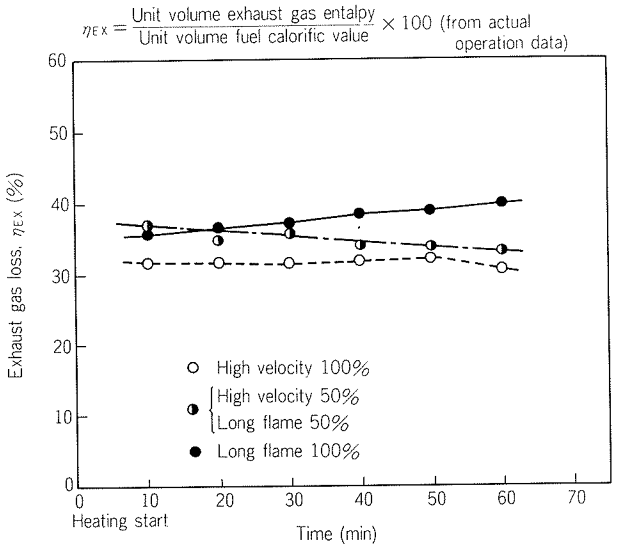

Fig. 13 Exhaust gas loss characteristics with burner types at initial stage of melting.

3. Operation results

According to the operation records taken over the past one month, an overall unit heat consumption for melting of the tower melter plus the main melter reached 844 BTU/lb. with the recovered heat from the waste heat boiler being reduced. In this case, the thermal efficiency is 59.6%, as shown in **Fig. 15**. The overall unit consumption before the reduction is 1076 BTU/lb. The average operational schedule during that period is as shown on **Table 2**.

The melting cycle has been shortened by about 20% as compared with that of conventional furnaces. The details are shown below.

Charging time	3%
Melting time	14%
Stirring time	3%

The rate of dross formation was 2.1% per a total

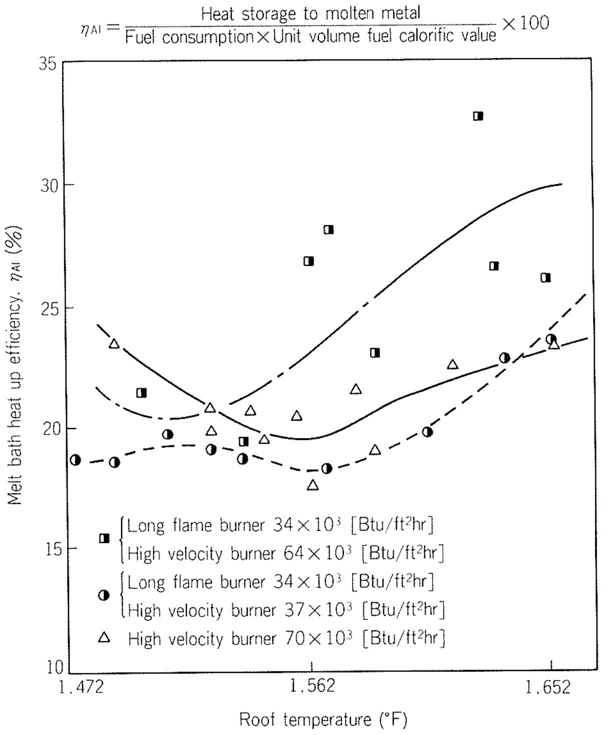

Fig. 14 Heating-up characteristics of melt bath with variation of burner type and firing rate.

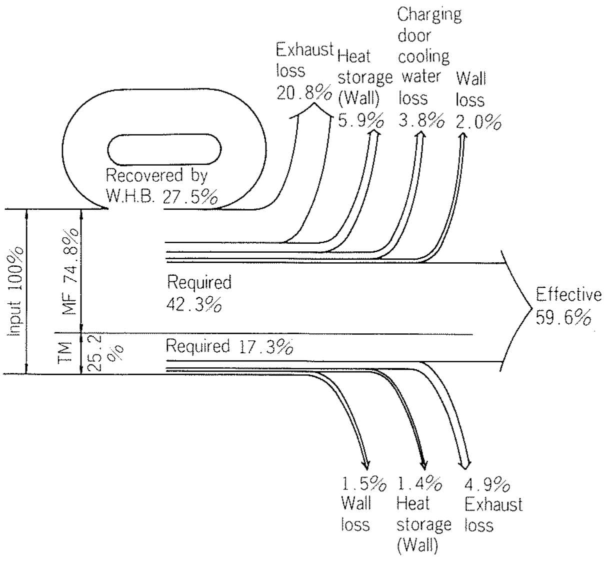
Charging door cooling water loss 3.8%
Exhaust loss 20.8%
Heat storage (Wall) 5.9%
Wall loss 2.0%
Recovered by W.H.B. 27.5%
Input 100%
MF 74.8%
TM 25.2%
Required 42.3%
Required 17.3%
Effective 59.6%
1.5% Wall loss
1.4% Heat storage (Wall)
4.9% Exhaust loss

Fig. 15 Total heat balance of F34 system.

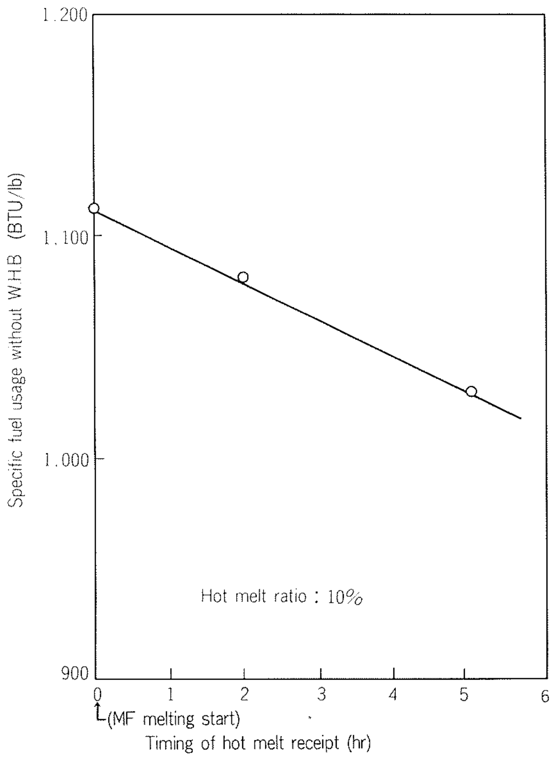

Fig. 16 Melter characteristic curve different timing of hot melt receipt from tower melter.

Table 2 Oprerational schedule.

1. Amount of charge	13,228,000 lb
2. Scrap	60%
3. Ingot	40% (T.M. 25%)
4. Alloy	1000 series 45%
	3000 〃 35%
	5000 〃 20%
5. Drainage for alloy change	28 times/month
6. Operation cycle	5.5hr
7. Molten metal temp.	1,382°F

charge of the tower and main melters, which is reduced to 0.98% after recovery of metals from the dross. The estimated net metal loss is 0.59%.

The later the timing of hot melt charging from the tower melter in the melting cycle, the higher the heat efficiency. This relation is shown in **Fig. 16**. If hot melt is charged in cold charge at an early stage of melting, the efficiency will drop due to the immersion of cold charge in the hot melt. In actual operations, however, a part of the hot melt is charged at an early stage of melting because of the limited holding capacity. On the other hand, in terms of melting loss, it should have a positive effect by protecting thin scraps from direct burner flames, but this is a difficult matter to analyze and evaluate.

4. Conclusion

Our technology implemented in the new furnace, based on experience since 1980 when we started directing toward convection type melting furnaces has led to certain achievements. In aluminium melting, however, there still remain many problems to be solved. The improvement of operators' techniques is also important in increasing the effectiveness of actual operations. We will endeavor to make steady progress despite the various existing constraints.